

*Study of Constitutive Behavior of Ferroelectrics via  
Self-Consistent Modeling and Neutron Diffraction*

**Thesis by**

**Seyed-Maziar Motahari**

**In Partial Fulfillment of the Requirements**

**For the Degree of**

**Doctor of Philosophy**

**California Institute of Technology**

**Pasadena, California**

**(Defended May 17, 2007)**

© 2007

Seyed-Maziar Motahari

All Rights Reserved

# Acknowledgments

Thanks first to my advisor and primary collaborator in this work, Professor Ersan Ustundag, for his support throughout my graduate studies. I'm grateful to Professor Kaushik Bhattacharya for acting as my Caltech advisor while I lived in Ames, Iowa. I am also very thankful to Professor Guruswami Ravichandran, Professor Chiara Daraio, and Professor Bill Johnson for participating in my defense as members of my committee.

I want to gratefully acknowledge the contributions of my research group mates: Dr. Seung-Yub Lee, Goknur Tutuncu, Mesut Varlioglu, Dr. Rob Rogan, Dr. Can Aydiner, Dr. Jacob Jones, and Sarah Shiley. They have not only been instrumental in collecting data necessary to this thesis, they have also offered support and assistance in numerous other ways, not the least of which has been their friendship. Two former fellow Caltech students, Dr. Arash Yavari and Dr. Amir Sadjadpour, have provided counsel, insight, enthusiasm, and inspiration, for which I will be forever indebted.

This section could not be complete without thanks to my family, especially Baba, Maman, Ardavan, Ali, Nahid-Joon, and Guity for the constant encouragement and guidance that they have generously bestowed on me throughout my life. Last, but certainly not least, I want to thank my wonderful wife, Lisa, for whom I would do anything and without whom I would accomplish nothing, the truth of which this thesis is an excellent proof.

# Abstract

The central goal of this study is to develop a reliable self-consistent model to describe the constitutive behavior of polycrystalline ferroelectrics and to predict their lattice strain and texture evolution. Starting with the model developed by Huber et al. formulations and refinements were added to increase both the functionality and the accuracy of the model's results. These refinements include methods for calculating lattice strain, tracking the number of domains contributing to diffraction patterns, locking the domain switching at a specified level, inputting initial grain orientation distribution, and a correction for a major flaw in the previous model: the phenomenon of reverse domain switching.

To validate the model's predictions, *in-situ* neutron diffraction experiments were conducted on polycrystalline BaTiO<sub>3</sub> under uniaxial compression. It was found that the data analysis required a close inspection due to lattice strain anisotropy and leading to a systematic study of different analysis methods: the single peak method, the regular whole-pattern Rietveld method (with no strain anisotropy), and the improved Rietveld method which offers limited strain anisotropy analysis. The latter was judged to be the most appropriate for ferroelectrics and it was further improved by new formulations to permit lattice strain anisotropy analysis for tetragonal and hexagonal crystal structures.

The comparison of model predictions and diffraction data from BaTiO<sub>3</sub> yielded the following observations: (i) domain switching starts at very low stresses (< 10 MPa) and proceeds gradually; (ii) domains with *c*-axes closer to the loading axis start switching earlier and experience more switching; (iii) lattice-plane-specific (*hkl*) strains, with the exception of (111), exhibit apparent hardening after switching starts. The level of agreement between the model and the experimental data was satisfactory, particularly considering the relative simplicity of the model. Keeping in mind the basic assumptions present in the model, it can be a useful analytical tool in the study of ferroelectric constitutive behavior when combined with diffraction experiments.

# List of Illustrations

Figure 1-1: The perovskite crystal structure common to many ferroelectric ceramics. For BTO the white ions at the corners are $\text{Ba}^{+2}$ , the black ions on the faces are $\text{O}^{-2}$ , and the central ion is $\text{Ti}^{+4}$ . The top set of figures illustrates the phase change through the Curie temperature, the spontaneous polarization, and the linear response of the crystal. The bottom set of figures illustrates the spontaneous shape change of the crystal, and $180^\circ$ and $90^\circ$ switching due to applied electric field or stress. The magnitudes of the ion displacements have been exaggerated for clarity. (Courtesy of C. Landis [8]) .....	4
Figure 1-2: Plane view of a crystal aggregate with domains as subregions of equal spontaneous polarization after cooling below the Curie temperature.....	6
Figure 1-3: At the paraelectric-ferroelectric phase transition of a material with tetragonal unit cell, there are six different directions for the central titanium ion to be displaced, resulting in six different spontaneous polarization vectors. ....	7
Figure 2-1: An ellipsoidal inclusion, I, is cut out of the matrix, M. ....	18
Figure 2-2: The inclusion has undergone a stress-free transformation, eigenstrain $\epsilon^T$ , and has been placed back in the matrix. The matrix applies constraining traction forcing the inclusion to assume a final strain $\epsilon^C$ , which can be related to $\epsilon^T$ using the Eshelby tensor, S.....	18
Figure 2-3: (a) The material properties of the inclusion are different from those of the matrix. The eigenstrain is real, due to a change in temperature, a phase transformation, etc. (b) The equivalent imaginary problem, constructed with an inclusion and a matrix that have the same material properties so that the Eshelby formula can be applied.....	20

Figure 2-4: In the case of external loading, the total stress in the inclusion is the sum of the stress due to the mismatch of thermal coefficients or a phase transformation and the applied stress at infinity. Again, (a) depicts the real problem and (b) is the imaginary one..... 21

Figure 2-5: Euler angles  $\varphi$ ,  $\theta$ , and  $\psi$  can be used to define the orientation of any object in three-dimensional space by applying three consecutive rotations to an object lying along the x-axis in a Cartesian system of coordinates. (Illustration from MathWorld.com)..... 25

Figure 2-6: Calculated (lines) and measured (symbols) stress-strain response parallel to the tensile axis for stainless steel. The experimental and modeling results have a good match in the elastic region. The results are less agreeable in the plastic regime. (Courtesy of B. Clausen)..... 31

Figure 3-1: The progressive nature of ferroelectric transformation within a crystal due to domain wall motion. This simplified example has only 2 domains, and the loading space is one-dimensional. (Courtesy of C. Landis) ..... 35

Figure 3-2: Self-consistent model estimates of the electrical displacement (top) and the strain (bottom) responses of a ferroelectric polycrystal to cyclic electric field loading [8]..... 38

Figure 3-3: Schematic of the experimental setup at ENGIN X. The diffracted neutrons are collected by two  $2\theta = \pm 90^\circ$  detectors with scattering vectors corresponding to the longitudinal and transverse directions of the specimen. .... 40

Figure 3-4: The domain selection mechanism incorporated into the new model. The [002] direction in domain 1, the [200] direction in domain 2, the [103] direction in domain 5, and the [301] direction in domain 6 are perfectly aligned with the scattering vector. The [002] and [200] directions in domains 3 and 4 are not exactly aligned with the scattering vector, but they lie within a  $5^\circ$  cone of it; so they also

contribute to the diffraction pattern. If these were the only grains in the material lattice strain [002] would be the average of the strains in domains 1 and 3, the strain along [200] would be the average of domains 2 and 4, the strain along [103] would be equal to the strain of domain number 5, and the strain along [301] would be equal to that of domain number 6. .... 41

Figure 3-5: Schematic of two domains in a grain. Domain A is along direction 1, and domain B is along direction 2. Transformation  $\alpha$  is defined as switching of A to B.

Transformation ' $-\alpha$ ' would be switching of B to A. .... 43

Figure 3-6: Plot of Equation (3.21) - the driving force for transformation ' $\alpha$ ' versus applied stress,  $\sigma_{11}$ . Whether  $\sigma_{11}$  increases in tensile or in compressive directions, the transformation ' $\alpha$ ' will not take place. Instead the transformation ' $-\alpha$ ' will occur, no matter what the sign of  $\sigma_{11}$  is. Referring to Figure 3-5, it is clear that the transformation ' $-\alpha$ ' will be physically meaningless under this applied compressive stress. .... 45

Figure 3-7: Same as in Figure 3-6, except the relative value of  $G_c^\alpha$  is smaller. As compressive stress along direction 1 is increased transformation ' $\alpha$ ' occurs as expected. Increasing compressive  $\sigma_{11}$  even further causes a transformation in the ' $-\alpha$ ' direction, which is an unrealistic case. .... 45

Figure 3-8: BaTiO<sub>3</sub> domain switching under applied uniaxial compressive stress predicted by the original Huber model. The number of domains selected for each reflection (i.e., those that diffract into the longitudinal detector) is plotted versus applied stress. As the load increases domains start to switch. This figure shows that the first switching starts at -30 MPa, and domains in the [002] direction are switched to domains in [200]. Exactly the same number of domains which are switched out of a direction is switched into the twin direction. Reverse switching is observed at about -100 MPa. At this load level [200] domains start to switch back into [002] domains. This seems counterintuitive. .... 46

Figure 4-1: A closer schematic of the sampling volume in Figure 3-3. Lattice planes and their d-spacings sampled by the longitudinal and transverse detectors are highlighted. ....	50
Figure 4-2: Diffraction spectra from a time-of-flight neutron diffraction experiment at ENGIN X using an unloaded BaTiO <sub>3</sub> polycrystal. The x-axis is either in terms of time-of-flight (a) or d-spacing (b), while the y-axis is the intensity of the diffracted neutrons in terms of counts per microsecond. ....	52
Figure 4-3: Single-peak fitting to reflections (200) and (002) of BaTiO <sub>3</sub> . ( a) Raw data and the fitted peak with peak position and intensity refined. (b) Peak width is added to the fitted parameters and a better fit is achieved ( $R_p = 3.5\%$ , $\chi^2 = 1.2$ , where $R_p$ is the minimum achievable pattern residual, and $\chi^2$ is the chi-square goodness-of-fit).....	55
Figure 4-4: (a) A full-pattern Rietveld fit to the diffraction data from a BaTiO <sub>3</sub> polycrystalline sample.(b) The (002) / (200) doublet shows a fit as good as that of the single-peak fitting method. This would not be the case when loading increases. ....	61
Figure 4-5: Different grains have different plane-specific elastic moduli, hence will exhibit different lattice strains. ....	64
Figure 4-6: Schematic definition of angles $\phi$ and $\rho$ in hexagonal (left) and tetragonal (right) unit cells.....	66
Figure 4-7: Crystallographic-direction-specific Young's modulus ( $E_{hkl}$ ) of beryllium (left) and magnesium (right) compared to approximations by Equations (4.20) and (4.22). The $\gamma_i$ parameters in these equations were refined to obtain the best fit to the $E_{hkl}$ curve.....	68
Figure 4-8: Lattice-plane-specific Young's modulus ( $E_{hkl}$ ) of BaTiO <sub>3</sub> (left) and its fit using Equation (4.26) with three refined $\gamma$ (right) .....	70

Figure 5-1: (002)/(200) peaks of BaTiO<sub>3</sub>: (a) is the unloaded sample, and (b) is under -100 MPa compressive stress. The dots are raw data while the green lines are the Rietveld fits. The Rietveld method fails to capture the texture evolution as loading has increased. .... 72

Figure 5-2: At zero loading the March-Dollase (M-D) coefficient value is 1.0, which indicates a random grain distribution. As loading increases, the M-D value increases, indicating domain switching. The change starts at very small loads. .... 73

Figure 5-3: (002)/(200) doublet and single-peak fits to the data using two type 3 peak profiles in GSAS. Both samples are BaTiO<sub>3</sub>: (a) is a stress-free sample, and (b) is under a compressive stress of -100 MPa. Comparison to Figure 5-1 shows the superiority of the single-peak method in texture analysis. .... 74

Figure 5-4: Peak Intensity Ratio diagrams for peak doublets (left to right) (200) / (002), (311) / (113), and (220) / (202). The independent axis is the y-axis which is the applied compressive stress in MPa. .... 76

Figure 5-5: Definition of angle  $\alpha$  between the loading axis (no. 1) and the c-axis of the red domain as it transforms into the blue domain. The unit vectors  $n$  and  $s$  are defined as the inside and outside bisectors, respectively, between the domains' c-axes. .... 77

Figure 5-6: Rietveld analyses of polycrystalline a BaTiO<sub>3</sub> sample with different crystal structures. (a) Tetragonal under -5 MPa stress, (b) tetragonal and orthorhombic under -5 MPa stress, (c) tetragonal under -220 MPa stress, and (d) tetragonal and orthorhombic under -220 MPa stress. .... 80

Figure 5-7: (002) Lattice strain using different diffraction data analysis methods (see text for details). The 'elastic' curve is the prediction of the self-consistent model assuming elastic deformation only. .... 81

Figure 5-8: The evolution of (002) / (200) peak doublets under loading analyzed with the single-peak fitting method. As loading increases (0 MPa, 50 MPa, and 150 MPa), the (002) peak vanishes, making a single peak fit impossible or extremely erroneous.

..... 83

Figure 5-9: Rietveld anisotropy parameter ( $\gamma$  in Equation (4.16)), a measure of the degree of anisotropy. Anisotropy increases as the sample is loaded. .... 84

Figure 5-10: Longitudinal lattice strains from neutron diffraction versus applied uniaxial compression of BaTiO<sub>3</sub>. The strain data were obtained from single-peak fitting. Linear trendlines were fitted to each data set to guide the eye. Note the extreme scatter in the (002) data due to diminished peak intensity at high applied stresses. .... 84

Figure 5-11: Sample BaTiO<sub>3</sub> macrostrain (elastic plus permanent) along the loading direction measured by an extensometer versus applied compressive stress ..... 85

Figure 5-12: Longitudinal lattice strains predicted by an elastic calculation of the SCM versus applied uniaxial compression of BaTiO<sub>3</sub>. The calculations employed the elastic constants listed in Table 5-1 and considered no domain switching. Note the relative slopes of the hkl-dependent lattice strains in comparison to the data on Figure 5-10. .... 86

Figure 5-13: BaTiO<sub>3</sub> domain switching under applied uniaxial compressive stress predicted by the model. The number of domains selected for each reflection (i.e., those that diffract into the longitudinal detector) is plotted versus applied stress. As the load increases domains start to switch beginning with the (002) / (200) pair. It can be seen that the closer the doublet axes are to the loading direction, the earlier the transformation starts. Unlike the original model, however, the new model does not predict reverse switching. .... 89

Figure 5-14: Lattice strain evolution under applied stress predicted by the SCM for (a) the (200) / (002) doublet, and (b) the (311) / (113) doublet ..... 90

Figure 5-15: (111), (200), and (002) lattice strains obtained from the new model are compared with diffraction data. (111) does not demonstrate nonlinearity, the other two crystal directions exhibit apparent hardening during switching in both experimental and modeling results. .... 92

# List of Tables

Table 2-1: Components of the Eshelby tensor. $\nu$ is the Poisson's ratio of the infinite matrix. ....	19
Table 4-1: Initial values used as a starting point for Rietveld refinements in BaTiO <sub>3</sub> experiments. ....	60
Table 5-1: Input data for the self-consistent program to model the BaTiO <sub>3</sub> experiment. $\mathbf{S}^E$ are the components of the elastic compliance tensor, $\mathbf{d}$ is the piezoelectric tensor, and $\kappa^\sigma$ is the permittivity of the material. ....	88

# Table of Contents

Acknowledgments .....	iii
Abstract.....	iv
List of Illustrations .....	vi
List of Tables.....	xiii
Table of Contents .....	xiv
<b>1. Introduction .....</b>	<b>1</b>
1.1 Ferroelectric Materials: Definition and Application.....	1
1.2 Piezoelectricity: Governing Equations.....	9
1.3 Ferroelectrics: Constitutive Modeling.....	12
1.4 Goal and Outline of Thesis.....	14
<b>2. The Self-Consistent Model .....</b>	<b>17</b>
2.1 The Eshelby Tensor.....	17
2.2 Inhomogeneous Inclusion .....	19
2.3 Multiple Inclusions.....	22
2.4 Polycrystals and the Self-Consistent Model .....	23
<b>3. Self-Consistent Modeling of Ferroelectrics .....</b>	<b>32</b>

3.1 The Huber Model .....	32
3.2 The New Self-Consistent Model.....	39
3.2.1 Grain Selection and Average Lattice ( <i>hkl</i> ) Strain .....	39
3.2.2 The Problem of Reverse Switching.....	42
<b>4. Neutron Diffraction Experiments .....</b>	<b>49</b>
4.1 Introduction .....	49
4.2 Experimental Setup and Sample Properties .....	50
4.3 Calculating Lattice Strains: the Single-Peak Method .....	53
4.4 Calculating Lattice Strains: the Rietveld Method .....	56
4.5 Calculating Lattice Strains: the Improved Rietveld Method ..	63
<b>5. Conclusions and Future Work .....</b>	<b>71</b>
5.1 Experimental Conclusions: Texture Evolution .....	71
5.2 Experimental Conclusions: Lattice Strains .....	81
5.3 Modeling Conclusions.....	87
5.4 Summary and Conclusions.....	93
5.5 Future Work .....	95
<b>Bibliography .....</b>	<b>97</b>

# 1. Introduction

## 1.1 Ferroelectric Materials: Definition and Application

Nowadays, many engineering problems necessitate the implementation of “smart”, i.e., adaptive or controlled, systems. Since these systems usually possess both sensing and actuation capabilities, a variety of physical phenomena are often coupled for their technical implementation. Thermal expansion, shape memory effect, magnetostriction, electrostriction, and piezoelectricity are some important examples of such coupling phenomena. It is now a matter of technical needs and costs that determine which coupling mechanism and which material will be the best choice.

Piezoceramics are outstanding candidates for mass applications calling for short response times, high-precision positioning and considerable actuation forces in systems of possibly complex shape. In this thesis, the term *piezoceramic* denotes polycrystalline ferroelectric materials (in general, they are ferroelastic as well) used for the exploitation of piezoelectricity in engineering. Barium titanate ( $\text{BaTiO}_3$ ) and lead zirconate titanate (PZT) are the most prominent materials in this class. While the former is the favored model material in fundamental material science investigations, the latter is preferred in technical applications due to its optimum electromechanical coupling properties [1].

Ferroelectric ceramics are widely used in a diverse set of devices including sensors, actuators, transducers, and ultrasonic motors [2]. The technological importance of

ferroelectrics originates from their large electromechanical coupling and their ability to be easily manufactured into complex geometries via powder processing and other advanced fabrication techniques. The phenomena of ferroelectricity, ferroelasticity, and piezoelectricity are here presented with reference to the commonly found perovskite crystal structure [3]. What will become clear in this discussion is that the unusual electromechanical macroscopic properties found in these materials can only be understood through an appreciation of the physical mechanisms operating in a multiaxial fashion at a range of microstructure-dependent length scales. The interaction of anisotropic mechanisms at multiple length scales leads to complicated behavior dependent on the specific application of external forces and the microstructure of the specimen under investigation.

A ferroelectric material is a piezoelectric material with the ability to switch its polarization direction under an applied electric or mechanical field. The microscopic structure of piezoelectric materials is crystalline in nature. In a crystalline material, the crystal lattice is a periodical repetition of a unit cell. A ceramic material is divided into grains with differing orientations of the crystal lattice. The unit cell consists of a buildup of positively and negatively charged ions typical of a specific material. According to this buildup, the centers of the positive and negative charges of the unit cell possess specific locations within the cell.

The position of the centers of the charges relative to one another within the unit cell is essential to the electromechanical properties of the material. A material is considered

to be polarizable if the centers can be shifted with respect to one another by the application of an external load, leading to a load-induced dipole in the unit cell. In the case of electric loading, the load is the applied electric field.

If the centers of positive and negative charge are at different positions from one another within the unit cell, even in the absence of any load, then the cell is considered to possess spontaneous polarization. In other words, the unit cell has a permanent dipole. In such a case, the material is called a polar material.

Mathematically, any relative displacement of the centers of positive and negative charge in a unit cell is described by the polarization vector. The magnitude of this vector is proportional to the distance between the centers and the respective sum of the positive and negative ionic charges. Polarization is usually denoted by  $\mathbf{P}$ .

Figure 1-1 illustrates the perovskite structure for many ferroelectrics including  $\text{BaTiO}_3$  (BTO) and  $\text{Pb}(\text{Zr}_x\text{Ti}_{1-x})\text{O}_3$  (PZT). Here, only the tetragonal structure is discussed, however orthorhombic, rhombohedral, and monoclinic crystal structures are also known to exist in these materials [3-7]. Above the Curie temperature  $T_c$ , the material is paraelectric with a cubic, centro-symmetric structure. As it is cooled below  $T_c$  it undergoes a phase transformation from the cubic to tetragonal phase. Notice that the previously centered Ti ion has been displaced towards one face of the tetragonal cell. The direction of this ion displacement is also the direction of the spontaneous polarization of the material,  $\mathbf{P}_s$ , and is aligned with the  $c$ -axis of the tetragonal cell (formerly the [001] cubic direction). Below  $T_c$  the material is both piezoelectric and

ferroelectric, and the piezoelectric properties of the crystal are aligned with the spontaneous polarization direction. Rhombohedral phase ferroelectrics possess ion displacements and polarizations along the  $\langle 111 \rangle$  cubic direction, and orthorhombic ones along the  $\langle 110 \rangle$ .

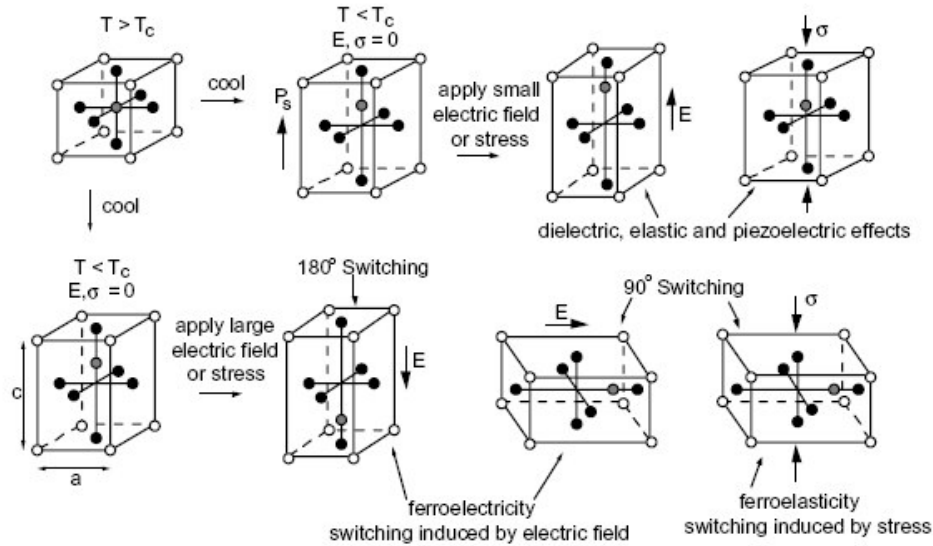


*Figure 1-1: The perovskite crystal structure common to many ferroelectric ceramics. For BTO the white ions at the corners are  $Ba^{+2}$ , the black ions on the faces are  $O^{-2}$ , and the central ion is  $Ti^{+4}$ . The top set of figures illustrates the phase change through the Curie temperature, the spontaneous polarization, and the linear response of the crystal. The bottom set of figures illustrates the spontaneous shape change of the crystal, and 180° and 90° switching due to applied electric field or stress. The magnitudes of the ion displacements have been exaggerated for clarity. (Courtesy of C. Landis [8])*

The piezoelectric, dielectric, and elastic responses of the tetragonal material are illustrated on the first row of Figure 1-1. If a small electric field is applied in the direction of the spontaneous polarization, then the polarization will increase (dielectric effect) together with strain (piezoelectric effect). Alternatively, if a compressive stress is aligned with the spontaneous polarization direction, then the

strain will decrease (elastic effect) and the polarization will decrease (piezoelectric effect).

The ferroelectric response of the material is illustrated on the second row of Figure 1-1 where ferroelastic switching has been differentiated from ferroelectric switching [3]. Note that a change in spontaneous strain, i.e., the orientation of the  $c$ -axis, accompanies the polarization change during  $90^\circ$  switching but not during  $180^\circ$  switching. For the tetragonal structure shown in Figure 1-1 there are four possible  $90^\circ$  switches that can be driven by combinations of stress and electric field, and one  $180^\circ$  switch that can be driven only by electric field. The middle two schematics on the second row of Figure 1-1 illustrate  $180^\circ$  and  $90^\circ$  switching induced by applied electric field alone. The last schematic illustrates  $90^\circ$  switching due to the application of a compressive stress parallel to the polarization direction. Note that for this compressive stress a switch to any one of the four energetically equivalent  $90^\circ$  domain variants can be activated.

A thorough understanding of the electromechanical mechanisms illustrated in Figure 1-1, including linear piezoelectricity and non-linear switching, is necessary for the explanation of most of the macroscopic phenomena observed in ferroelectrics.

However, the depiction of switching that is obtained from the consideration of a single lattice cell is deceptively simplified. As explained by Figures 1-2 and 1-3, in real single crystals (including single grains of a polycrystal), there exist multiple domain variants separated by domain walls formed by twin boundaries [3, 5, 6].

Across a domain wall the spontaneous polarization is discontinuous. Switching of a domain is not a homogenous process as the single unit cell depiction would suggest, but rather proceeds as a result of domain wall motion which converts one domain variant to another [3, 5, 6, 9]. Even within a single crystal different concentrations of the six possible domain variants can coexist such that the irreversible (or remanent) polarization, and hence the piezoelectric properties, of the crystal can be oriented in any of these six directions through application of a large electric field to induce domain switching; this process is called “poling.” The ability of ferroelectric single crystals to be poled in certain directions is of significant technological importance, as it allows for the piezoelectric response to be oriented for use in applications. Successful poling of a single crystal depends on the relative concentrations of the initial domain variants, crystal purity (any impurities can impede domain wall motion), and the direction and strength of the applied electric field.

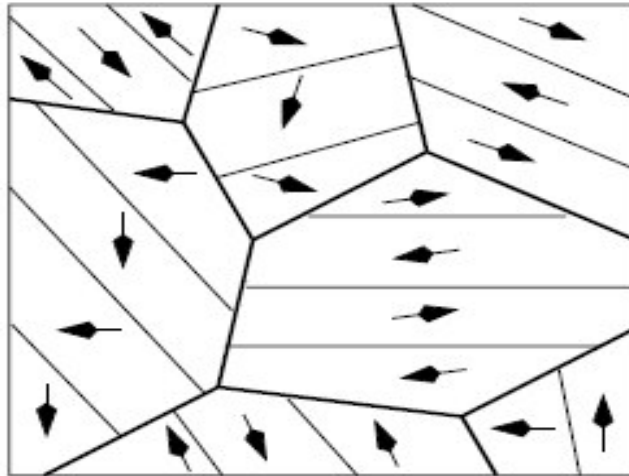


*Figure 1-2: Plane view of a crystal aggregate with domains as subregions of equal spontaneous polarization after cooling below the Curie temperature*

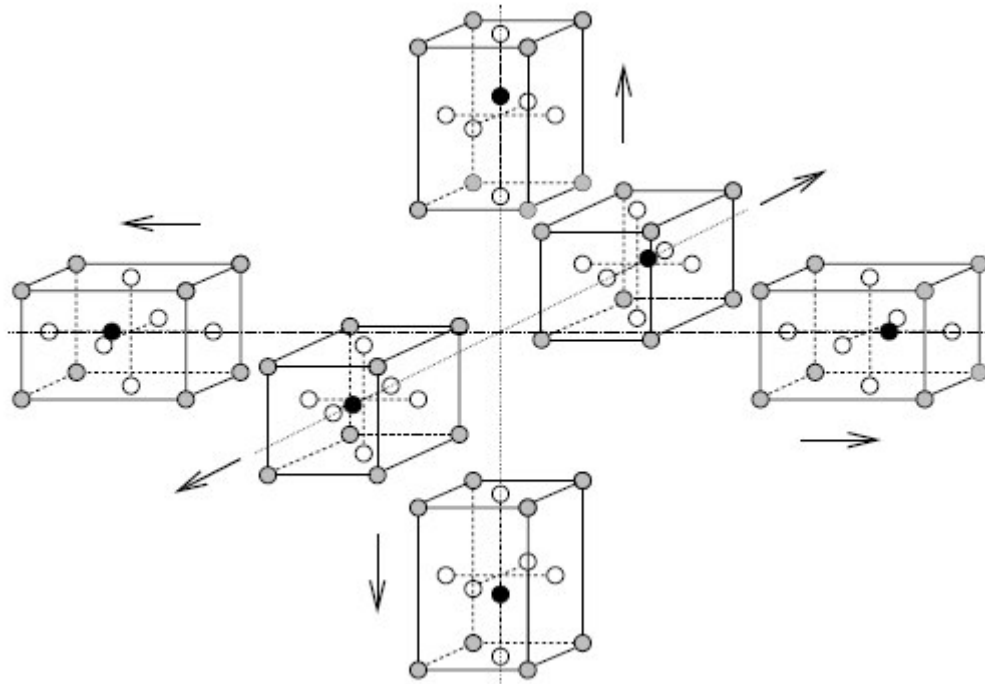


*Figure 1-3: At the paraelectric-ferroelectric phase transition of a material with tetragonal unit cell, there are six different directions for the central titanium ion to be displaced, resulting in six different spontaneous polarization vectors.*

Let us now consider macroscopic phenomena that result from microscopic, i.e., domain-level, mechanisms averaged over volumes which are associated with the polycrystals used in most ferroelectric devices. When the material is cooled below the Curie temperature spontaneous polarization, spontaneous strain and piezoelectricity must exist at the individual domain level. However, when averaged over all possible orientations of the domains and grains within the polycrystal, the macroscopic polarization, strain, and piezoelectric effect of the ceramic are initially zero. In order to make the polycrystal piezoelectric, and therefore useful in actuator or sensor applications, a strong electric field must be applied. In the case of a polycrystal, the

initially homogenous orientation distribution of the ceramic implies that the specimen may be poled in an arbitrary direction.

As the electric field is applied, domain walls move such that domains aligned with the field grow at the expense of domains opposing the field. However, the randomized grain and domain configuration established during preparation limits the possible orientations of any domain variant relative to the externally applied field. Thus, during poling, domains will attempt to switch their polarizations into orientations aligned with the macroscopic field, but the fixed grain structure may severely limit switching ability [2]. The poling process, then, occurs gradually and over a range of applied electric fields due to the variation in local electromechanical boundary conditions (intergranular constraints). In certain grain orientations, domains may switch temporarily to minimize the total energy during the application of an electric field. After the field is removed, some domain walls will move back towards their original positions, due to residual stresses and local electric fields in the material. However, this reverse switching is incomplete and there exists a net polarization, strain and piezoelectric effect aligned in the direction of the original applied electric field. The material is now “poled” and suitable for use as an actuator or sensor.

Many of the most industrially successful ferroelectric compositions possess grains of multiple crystal structures, such as the rhombohedral-tetragonal phase combination found in the morphotropic region of the PZT phase diagram [5]. As such, ferroelectrics can exhibit a complicated behavior in response to both electrical and

mechanical loads which produce large internal stresses that eventually lead to failure. Efforts to model and predict the behavior of ferroelectrics have often been hindered by the lack of suitable constitutive relations that accurately describe the electromechanical response of these materials. While many measurements have been conducted on the *macroscopic* response of large single crystals or polycrystals, there is lack of multiaxial (and multiscale) data about the *in-situ* internal strain and texture response of these materials; this information is critical to the development of accurate models, and it can only be provided by diffraction techniques which directly measure internal lattice strains and crystallographic orientations. This thesis will present a comparison of a mechanics model with diffraction data.

## 1.2 Piezoelectricity: Governing Equations

In a ferroelectric, domain wall motion within each crystal leads to a change in the remanent strain and polarization. This non-linear switching closely resembles plastic deformation by slip in a metallic polycrystal: domain wall motion can be treated in an analogous manner as dislocation slip in elastic-plastic crystals.

Consider an anisotropic ferroelectric solid subjected to an electric field  $\mathbf{E}_i$  and to a mechanical stress  $\sigma_{ij}$ . By assigning the notation superscript ‘ $L$ ’ for the recoverable (assumed linear) part and the superscript ‘ $R$ ’ for the remanent part (equivalent to the plastic part in crystalline plasticity), one can decompose the total strain  $\epsilon_{ij}$  and the total electric displacement  $\mathbf{D}_i$  into linear and remanent parts:

$$\boldsymbol{\varepsilon}_{ij} = \boldsymbol{\varepsilon}_{ij}^L + \boldsymbol{\varepsilon}_{ij}^R \quad (1.1)$$

and

$$D_i = D_i^L + P_i^R \quad (1.2)$$

The remanent strain,  $\boldsymbol{\varepsilon}_{ij}^R$ , and polarization,  $P_i^R$ , are obtained upon the removal of electrical and mechanical loading ( $\boldsymbol{\sigma}_{ij}, \mathbf{E}_i$ ). Assuming that strains remain sufficiently small for the infinitesimal strain theory to apply, the total strain derived from the displacement field  $\mathbf{u}_i$  is given by:

$$\boldsymbol{\varepsilon}_{ij} \equiv \frac{1}{2}(u_{i,j} + u_{j,i}) \quad (1.3)$$

The linear response of the ferroelectric solid is then:

$$\boldsymbol{\sigma}_{ij} = c_{ijkl}^D (\boldsymbol{\varepsilon}_{kl} - \boldsymbol{\varepsilon}_{kl}^R) - h_{kij} (D_k - P_k^R) \quad (1.4)$$

and

$$E_i = -h_{ikl} (\boldsymbol{\varepsilon}_{kl} - \boldsymbol{\varepsilon}_{kl}^R) + \beta_{ik}^\varepsilon (D_k - P_k^R) \quad (1.5)$$

where,  $c_{ijkl}^D$  is the elastic stiffness tensor,  $h_{ijk}$  is the piezoelectric tensor, and  $\beta_{ik}^\varepsilon$  is the dielectric impermeability tensor. A number of alternative versions of the piezoelectric constitutive relations exist, each exactly equivalent to the ones mentioned above. For example, Equations (1.4) and (1.5) can be inverted to obtain:

$$\boldsymbol{\varepsilon}_{ij} - \boldsymbol{\varepsilon}_{ij}^R = S_{ijkl}^E \boldsymbol{\sigma}_{kl} + d_{kij} E_k \quad (1.6)$$

and

$$D_i - P_i^R = d_{ikl} \boldsymbol{\sigma}_{kl} + \kappa_{ik}^\sigma E_k \quad (1.7)$$

Alternatively,  $(\boldsymbol{\sigma}_{ij}, D_i - P_i^R)$  is related to  $(\boldsymbol{\varepsilon}_{ij} - \boldsymbol{\varepsilon}_{ij}^R, E_i)$  by:

$$\sigma_{ij} = c_{ijkl}^E (\epsilon_{kl} - \epsilon_{kl}^R) - e_{kij} E_k \quad (1.8)$$

and

$$D_i - P_i^R = e_{ikl} (\epsilon_{kl} - \epsilon_{kl}^R) + \kappa_{ik}^E E_k \quad (1.9)$$

All these linear equations remain valid during the switching of a ferroelectric, which is a non-linear phenomenon, but are not sufficient to relate an increment in the loading  $(\dot{\sigma}_{ij}, \dot{E}_i)$  to a corresponding increment in configurational quantities  $(\dot{\epsilon}_{ij}, \dot{D}_i)$ . A complete framework requires information on how the remanent increments  $(\dot{\epsilon}_{ij}^R, \dot{P}_i^R)$  evolve with increments in loading  $(\dot{\sigma}_{ij}, \dot{E}_i)$ . This issue will be addressed in Chapter 3 when a self-consistent model is presented.

Static mechanical equilibrium dictates that the stress  $\sigma_{ij}$  is in equilibrium with an imposed distribution of body force  $f_i$  according to

$$\sigma_{ij,j} + f_i = 0 \quad (1.10)$$

and the Gauss' law likewise dictates that the divergence of the electric displacement equals the distribution of free charge density  $q$

$$D_{i,i} - q = 0. \quad (1.11)$$

Assuming quasi-static conditions, the electric field is derived from an electric potential  $\Phi$  via:

$$E_i \equiv -\Phi_{,i} \quad (1.12)$$

On the surface  $S$  of a piezoelectric body, with unit outward normal  $\mathbf{n}_i$ , the traction  $\mathbf{t}_i$  is in equilibrium with the stress  $\sigma_{ij}$  according to

$$t_j = n_i \sigma_{ij} \quad (1.13)$$

and the surface-free charge density  $Q$  is in equilibrium with the jump in electric displacement  $\langle D_i \rangle$  across  $S$ , such that

$$Q = n_i \langle D_i \rangle = n_i (D_i^o - D_i). \quad (1.14)$$

Here, the symbol “ $\langle \rangle$ ” to denotes the jump in a quantity at the boundary and  $D_i^o$  is the electrical displacement exterior to the body [8].

### 1.3 Ferroelectrics: Constitutive Modeling

#### 1.3.1 Background

A successful design for a component in many engineering applications often necessitates a complex interactive process that utilizes modeling and experimentation. This is especially crucial in predicting device/component performance and lifetime. To achieve this, it is essential that the model employs a realistic constitutive law that accurately describes material response to external loading.

One of the commonly used models is the Finite Element Method (FEM). In order to have an informative and detailed FEM model, one often needs to know the spatial distribution of the grains being modeled. This information is not readily available most of the time.

Another approach is the use of the Self-Consistent Model (SCM). In this model the spatial distribution of the grains need not be known. Each single grain is assumed to

interact with an imaginary media (matrix) with properties derived from the average properties of all other grains. The self-consistent method has been used successfully in crystal elastoplasticity. It has also been used to predict the macroscopic behavior of ferroelectrics. The present study will show how it can be used for the investigation of lattice strains and texture evolution in ferroelectrics and how the results compare with neutron diffraction experiments.

The fundamentals of the self-consistent method are based on Eshelby's inclusion method. In his papers published in 1957 and 1961, Eshelby [10, 11] solved the problem in closed form of an ellipsoidal inclusion in an infinite matrix with a misfit due to change in temperature. His approach can readily be expanded to solve the general problems of multiple inclusions, a finite matrix, and applied mechanical loading. Eshelby's method and the aforementioned extensions are explained in Chapter 2. The Eshelby method has been further developed into a self-consistent method to solve polycrystalline plasticity problems. Studies have been conducted to simulate the development of lattice strain and texture during loading. These, too, will be briefly reviewed in Chapter 2.

### **1.3.2 Self-Consistent Modeling of Ferroelectrics**

In their 1999 paper, Huber et al. developed an SCM to study macroscopic behavior of ferroelectrics [8]. Their model is based on the switching of differently oriented tetragonal domains within a grain under the application of mechanical loading or an electric field. The model provides good qualitative predictions for many of the

macroscopic features of ferroelectric switching, but it lacks the capacity to compute lattice strains. The improvement of the model to obtain this capability is the subject of Chapter 4.

The work of Hall et al., 2005-2007 [12-15], seems, at first glance, to be similar to the present study. They have also studied lattice strains in ferroelectrics via physical experimentation and a micromechanical model. However, there are two major differences. They have conducted X-ray experiments to calculate lattice strains in PZT, but the experiments were not *in situ*. Instead, they measured residual lattice strains after the application and removal of an electric field. Then they rotated the sample around an axis perpendicular to the polarization axis and diffraction vector. The purpose of the experiments discussed in this thesis is to study the evolution of lattice strains while the loading is being applied. The second key difference is in the modeling. Due to the different nature of their experiments, they have been able to use a simple model which helps them explain why the lattice strain can be fitted linearly with moderate success using the cosine square of the rotation angle as the independent variable. In comparison, the model presented here aims to predict the lattice strains given the single crystal properties of the ferroelectric and known domain switching criteria.

#### **1.4 Goal and Outline of Thesis**

The main goal of this thesis is to investigate the *in-situ* lattice strain and texture evolution in ferroelectrics, specifically BaTiO<sub>3</sub>, using self-consistent modeling and

neutron diffraction data. Along the way, it will be shown that improvements were needed in both the analysis of diffraction data and the self-consistent modeling.

The introduction to ferroelectrics, previous studies, and equations governing ferroelectrics were explained in this chapter. Chapter 2 will discuss the self-consistent model and its basis, the Eshelby method, as they existed before the SCM was extended into ferroelectrics. Cases of mechanical versus thermal loading, and single versus multiple inclusions are also discussed. Next, the formulation of SCM as a means to simulate grain-to-grain interactions is presented. Chapter 3 will explain the SCM for ferroelectric domain switching and the improvements made to a previous model to be able to compare its predictions with diffraction data.

Chapter 4 will elaborate on the experimental methods used and the experimental challenges faced. The single peak fitting and the multi-peak Rietveld method and their advantages and disadvantages will be discussed. Also, an improved version of the Rietveld method which should be used with anisotropic materials will be discussed. This method is currently implemented in the common Rietveld code *GSAS* (General Structure Analysis System)[16] for some crystal structures. Guidelines on how to implement it for other structures are also provided in this chapter.

Chapter 5 will present the experimental results from different methods of analysis, including the *in-situ* lattice strain measurements of BaTiO<sub>3</sub> and its *in-situ* texture evolution. Modeling results, using the model developed in Chapter 3, and the

comparison between the model and the experimental results will also be presented in Chapter 5. Finally, the conclusions will be summarized, and some suggestions for future work will be offered.

## 2. The Self-Consistent Model

### 2.1 The Eshelby Tensor

The fundamentals of the self-consistent model are based on Eshelby's inclusion method. In his papers published in 1957 and 1961, Eshelby [10, 11] solved the problem of an ellipsoidal inclusion in an infinite matrix with a misfit due to change in temperature in closed form. His approach can readily be expanded to solve the general problems of multiple inclusions, a finite matrix, and applied mechanical loading.

Assume an infinite media, referred to as 'the Matrix.' A part of the matrix is cut out, referred to as 'the Inclusion,' and undergoes a stress free transformation, or 'eigenstrain.' This eigenstrain can be due to a mismatch in thermal expansion coefficients, or it can be a result of a martensitic phase transformation, etc.

If the inclusion is to be put back in the matrix (Figures 2-1 and 2-2), due to the mismatch in size, stresses will obviously develop in both the matrix and the inclusion. Eshelby [10, 11] showed that if the inclusion has an ellipsoidal shape, the stress in the inclusion will be uniform. He also related the strain mismatch to the final strain through the Eshelby tensor,  $\mathbf{S}$ ; he then calculated the value of  $\mathbf{S}$ , as shown in Table 2-1 [17]. Needless to say, stress in the matrix is not homogenous but fades away with increasing distance from the inclusion. If the stiffness tensor of the matrix,  $\mathbf{C}_M$ , is

known, which in this case is the same as the stiffness tensor for the inclusion, the residual strain and stress can be readily calculated:

$$\varepsilon^C = S \varepsilon^T \quad (2.1)$$

$$\sigma_I = C_M (\varepsilon^C - \varepsilon^T) = C_M (S - U) \varepsilon^T. \quad (2.2)$$

The subscript  $I$  denotes the inclusion and  $U$  in the equation is the identity matrix.

Superscript  $C$  denotes a constrained value.  $\varepsilon^T$  is the eigenstrain, and  $S$  is the Eshelby tensor.

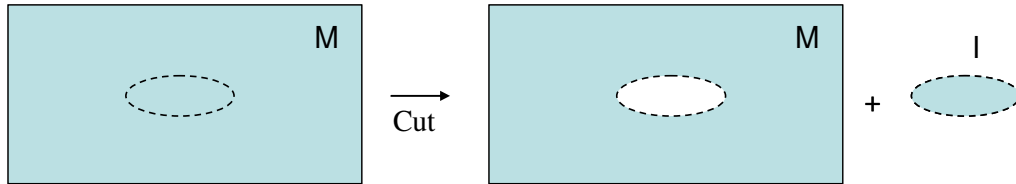


Figure 2-1: An ellipsoidal inclusion,  $I$ , is cut out of the matrix,  $M$ .

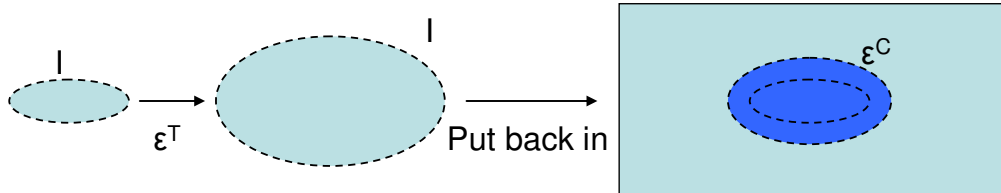


Figure 2-2: The inclusion has undergone a stress-free transformation, eigenstrain  $\varepsilon^T$ , and has been placed back in the matrix. The matrix applies constraining traction forcing the inclusion to assume a final strain  $\varepsilon^C$ , which can be related to  $\varepsilon^T$  using the Eshelby tensor,  $S$ .

$S_{ijkl}$	<i>Fibers</i>	<i>Spheres</i>	<i>Plates</i>
$S_{3333}$	0	$\frac{7-5\nu}{15(1-\nu)}$	1
$S_{1111} = S_{2222}$	$\frac{5-\nu}{8(1-\nu)}$	$\frac{7-5\nu}{15(1-\nu)}$	0
$S_{1122} = S_{2211}$	$\frac{-1+4\nu}{8(1-\nu)}$	$\frac{-1+5\nu}{15(1-\nu)}$	0
$S_{1133} = S_{2233}$	$\frac{\nu}{2(1-\nu)}$	$\frac{-1+5\nu}{15(1-\nu)}$	0
$S_{3311} = S_{3322}$	0	$\frac{-1+5\nu}{15(1-\nu)}$	$\frac{\nu}{1-\nu}$
$S_{1212} = S_{1221} =$ $S_{2112} = S_{2121}$	$\frac{3-4\nu}{8(1-\nu)}$	$\frac{4-5\nu}{15(1-\nu)}$	0
$S_{1313} = S_{2323} =$ $S_{1331} = S_{2332} = \dots$	$\frac{1}{4}$	$\frac{4-5\nu}{15(1-\nu)}$	$\frac{1}{2}$
<i>All Other <math>S_{ijkl}</math></i>	0	0	0

Table 2-1: Components of the Eshelby tensor.  $\nu$  is the Poisson's ratio of the infinite matrix.

## 2.2 Inhomogeneous Inclusion

The above case, where the elastic stiffness of the matrix and the inclusion are the same, is highly unrealistic. If the inclusion has a different stiffness tensor,  $\mathbf{C}_I$ , the problem is not so easily solved since the equation,  $\boldsymbol{\varepsilon}^{\mathbf{C}} = \mathbf{S} \boldsymbol{\varepsilon}^{\mathbf{T}}$ , no longer holds true. Eshelby solved the problem only for a matrix and an inclusion of the same material.

To circumvent this problem, an imaginary counterpart (Figure 2-3b) to the real problem (Figure 2-3a) is constructed. The imaginary problem, the “ghost problem,” has an inclusion which has an elastic stiffness of  $\mathbf{C}_M$ . Hence, the Eshelby formula can

be applied to it. It can be shown that one can choose a size for the ghost inclusion and assume an eigenstrain for it such that the final constrained strain and the traction on the ghost inclusion are equal to the constrained strain and traction on the inclusion in the real problem. The conclusion is that the matrix is practically dealing with the same inclusion in cases (a) and (b), so the results can be used interchangeably.

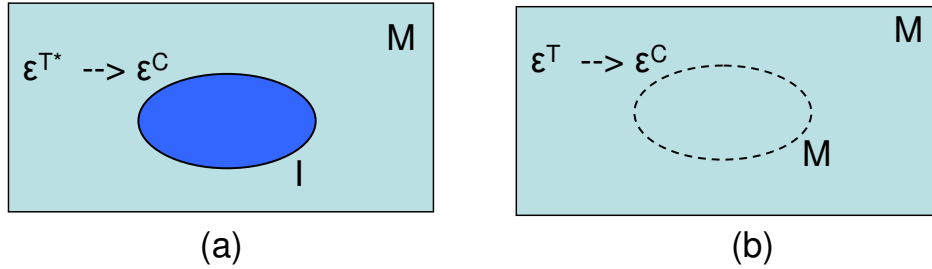


Figure 2-3: (a) The material properties of the inclusion are different from those of the matrix. The eigenstrain is real, due to a change in temperature, a phase transformation, etc. (b) The equivalent imaginary problem, constructed with an inclusion and a matrix that have the same material properties so that the Eshelby formula can be applied

$$\text{Figure 2-3 (a)} \rightarrow \sigma_I = C_I (\epsilon^C - \epsilon^{T*}) \quad (2.3)$$

$$\text{Figure 2-3 (b)} \rightarrow \sigma_I = C_M (\epsilon^C - \epsilon^T) \quad (2.4)$$

$$\text{Figure 2-3 (b)} \rightarrow \epsilon^C = S \epsilon^T \quad (2.5)$$

$$\rightarrow C_I (\epsilon^C - \epsilon^{T*}) = C_M (\epsilon^C - \epsilon^T) \rightarrow C_I (S \epsilon^T - \epsilon^{T*}) = C_M (S \epsilon^T - \epsilon^T) \quad (2.6)$$

$$\epsilon^T = [(C_I - C_M) S + C_M]^{-1} C_I \epsilon^{T*} \quad (2.7)$$

$$\sigma_I = C_M (S - I) \epsilon^T = C_M (S - I) [(C_I - C_M) S + C_M]^{-1} C_I \epsilon^{T*} \quad (2.8)$$

Here,  $\epsilon^{T*}$  is the eigenstrain of the real inclusion which can be due to difference in the coefficient of thermal expansion between the matrix and the inclusion or due to phase

transformations, and  $\boldsymbol{\varepsilon}^T$  is the eigenstrain in the ghost inclusion which is just an imaginary construct.

Exactly the same concepts hold in the case of an applied external load (Figures 2-4a and 2-4b), only more care should be taken in writing the inclusion stress-elastic strain relationships. It is then possible to calculate the stress and constrained strain for such a case as well.

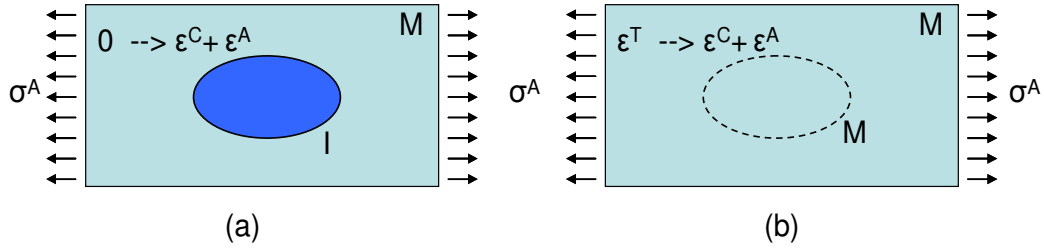


Figure 2-4: In the case of external loading, the total stress in the inclusion is the sum of the stress due to the mismatch of thermal coefficients or a phase transformation and the applied stress at infinity. Again, (a) depicts the real problem and (b) is the imaginary one.

$$(a) \rightarrow \sigma_I + \sigma^A = C_I (\varepsilon^C + \varepsilon^A) \quad (2.9)$$

$$(b) \rightarrow \sigma_I + \sigma^A = C_M (\varepsilon^C + \varepsilon^A - \varepsilon^T) \quad (2.10)$$

$$(b) \rightarrow \varepsilon^C = S \varepsilon^T \quad (2.11)$$

$$\varepsilon^T = -[(C_I - C_M) S + C_M]^{-1} (C_I - C_M) \varepsilon^A \quad (2.12)$$

$$\sigma_I + \sigma^A = -C_M (S - I) [(C_I - C_M) S + C_M]^{-1} (C_I - C_M) \varepsilon^A + C_M \varepsilon^A \quad (2.13)$$

In the above equations,  $\sigma^A = C_M \varepsilon^A$ . Note that in this case  $\sigma_I$  is not the total inclusion stress, instead it is the mismatch stress.

### 2.3 Multiple Inclusions

A single inclusion in an infinite matrix is not a very realistic situation, but instead multiple inclusions are usually present. One way to relate such a case to the calculations presented up to now is to assume that an inclusion does not have the whole matrix constraining it, but only a portion of the matrix around itself. As a result there would be less constraint and the inclusion will be more relaxed. One way to model this is to assume a background stress already present in the matrix denoted by  $\langle \sigma \rangle_M$ . The equations would now be very similar to what was presented before, for both external stress and eigenstrain. In case of eigenstrain:

$$\sigma_I + \langle \sigma \rangle_M = C_I (\varepsilon^C + \langle \varepsilon \rangle_M - \varepsilon^{T*}) \quad (2.14)$$

$$\sigma_I + \langle \sigma \rangle_M = C_M (\varepsilon^C + \langle \varepsilon \rangle_M - \varepsilon^T) \quad (2.15)$$

$$\varepsilon^C = S \varepsilon^T \quad (2.16)$$

where,  $\langle \sigma \rangle_M = C_M \langle \varepsilon \rangle_M$  is the background stress, and  $\langle \sigma \rangle_I \equiv \sigma_I + \langle \sigma \rangle_M$  is the inclusion stress.

The value of the background stress should be such that the inclusion and matrix are in equilibrium. Thus:

$$f \langle \sigma \rangle_I + (1-f) \langle \sigma \rangle_M = 0 \quad (2.17)$$

where, 'f' is the volume fraction of the inclusions. Solving for  $\varepsilon^T$  in these equations will give:

$$\varepsilon^T = \{(C_M - C_I)[S - f(S-I)] - C_M\}^{-1} C_I \varepsilon^{T*}. \quad (2.18)$$

From which stress in 'M' and 'I' can be calculated:

$$\langle \sigma \rangle_M = -f C_M (S-I) \varepsilon^T \quad (2.19)$$

$$\langle \sigma \rangle_I = (1-f) C_M (S-I) \varepsilon^T. \quad (2.20)$$

In the case of external loading the only difference would be  $\varepsilon^T$ :

$$\varepsilon^T = \{(C_M - C_I)[S - f(S-I)] - C_M\}^{-1} (C_M - C_I) \varepsilon^A \quad (2.21)$$

and, of course,  $\sigma^A$  should be added to obtain the total stress.

## 2.4 Polycrystals and the Self-Consistent Model

Almost all structural materials are polycrystals made up of multiple grains. In order to design and optimize engineering components constructed out of these materials, it is necessary to know the internal stress/strain state in the polycrystal.

Micromechanical polycrystal deformation models that are based on the deformation of the individual grains can be used to determine the overall stress state of a component, including the residual and intergranular stress. These models can predict the elastic and plastic deformation of grains and, consequently, the overall stresses in the polycrystal. Many polycrystal deformation models that use different assumptions have been proposed over the years. In the lower-bound models, e.g., Sachs 1928 [18], the grains are all subjected to the same stress, as opposed to the upper-bound models,

e.g., Taylor 1938 [19], where all the grains are subjected to the same strain. These models do not account for anisotropy; hence, they do not serve our purposes.

A self-consistent model is one way of modeling grain-to-grain interactions. Similar to the Sachs and Hill methods, the topological aspects of the microstructure are neglected in this method; instead, each grain interacts with other grains through the matrix, also called the homogeneous equivalent medium (HEM). The material properties of this matrix are an average of the properties of the grains that make up the conglomerate.

In the self-consistent model, the effects of elastic anisotropy can be considered. Most of the ferroelectric materials of interest are extremely anisotropic; thus, the self-consistent model provides a far superior method of analysis to the Sachs and Taylor models. In the rest of this section, details regarding the formulation of a self-consistent method for solving problems of elastoplastic polycrystalline deformations are presented. These will serve as a useful guidance and background for the SCM of ferroelectrics presented in Chapter 3.

The self-consistent scheme includes the elastic-plastic interaction between grains that are regarded as ellipsoidal inclusions in an infinite homogenous matrix with the overall modulus of the polycrystal. The grains are modeled as single crystals with specific orientations represented by their Euler angles ( $\varphi$ ,  $\theta$ , and  $\psi$ ) defined in Figure 2-5. The three-dimensional orientation of any object in space can be related to the

orientation of an object lying along the  $x$ -axis in a Cartesian coordinate system  $x$ - $y$ - $z$  by using these angles that represent three consecutive rotations. The first rotation is  $\varphi$  in the positive direction around the  $z$ -axis, the second is a rotation of  $\theta$  around the new  $x$ -axis, and the third is a rotation of  $\psi$  around the new  $z$ -axis.

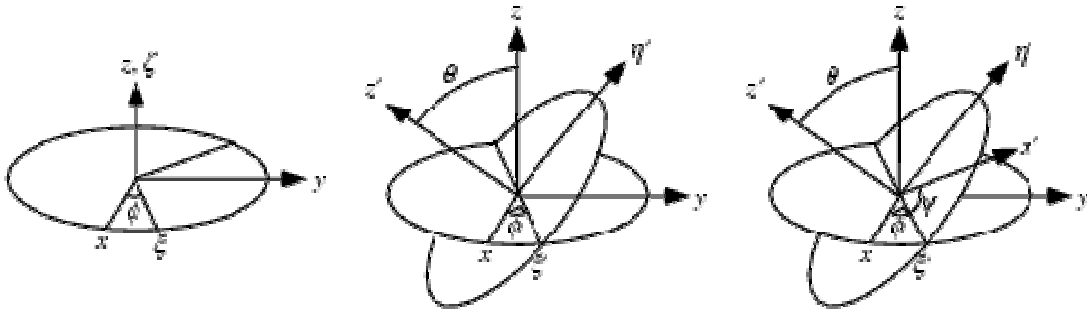


*Figure 2-5: Euler angles  $\varphi$ ,  $\theta$ , and  $\psi$  can be used to define the orientation of any object in three-dimensional space by applying three consecutive rotations to an object lying along the  $x$ -axis in a Cartesian system of coordinates. (Illustration from MathWorld.com)*

The self-consistent model to be discussed here [20] is restricted to low strains, as the strain definition does not include second-order terms, and the model does not include localization, which can lead to instabilities such as necking. As a rule, a small strain model is valid as long as the tangent modulus is much larger than any of the stress components.

The model is governed by the single crystal slip mechanisms, in which the controlling parameters are the critical resolved shear stress and the hardening law. The number, crystallographic planes and directions of slip systems depend on the crystal structure of the material under study. For example, in a face centered cubic ( $fcc$ ) material the potential slip systems are  $\{111\} \langle 110 \rangle$  which consist of 12 plane-direction single slips. The initial critical resolved shear stress,  $\tau_0$ , is assumed to be the same for all slip

systems. The number of potential slip systems is effectively doubled, as the shear rates are assumed not to be negative.

Plastic strain rate in the grain can be related to the rate of movement in the active slip systems:

$$\dot{\boldsymbol{\varepsilon}}_{kl}^P = \sum_i \dot{\gamma}^i \boldsymbol{\mu}_{kl}^i . \quad (2.22)$$

The term  $\boldsymbol{\varepsilon}^P$  is the plastic strain tensor in the grain,  $\dot{\gamma}^i$  is the movement of the  $i^{\text{th}}$  slip system in the grain, and  $\boldsymbol{\mu}^i$  is the Schmid tensor related to the  $i^{\text{th}}$  slip system. The elements of the Schmid tensor for the  $i^{\text{th}}$  slip system, which is a slip on a plane with a normal vector  $\boldsymbol{n}^i$  in the direction of vector  $\boldsymbol{m}^i$ , are:

$$\boldsymbol{\mu}_{kl}^i = \frac{1}{2} (m_k^i n_l^i + m_l^i n_k^i) . \quad (2.23)$$

Similarly, the resolved shear stress rate on each slip system,  $\dot{\tau}^i$ , can be written in terms of the state of stress in the grain,  $\boldsymbol{\sigma}$ , and the Schmid tensor:

$$\dot{\tau}^i = \dot{\boldsymbol{\sigma}}_{kl} \boldsymbol{\mu}_{kl}^i . \quad (2.24)$$

The active slip systems are chosen from the potential slip systems such that they minimize the dissipated energy corresponding to plastic deformation in the grain.

The current critical resolved shear stress of the  $i^{\text{th}}$  slip system is denoted  $\tau_c^i$  and its rate is assumed to be related to the shear rates by a hardening matrix  $\boldsymbol{h}^{ij}$  [20]:

$$\dot{\tau}_c^i = \sum_j h^{ij} \dot{\gamma}^j . \quad (2.25)$$

The components of the hardening matrix are defined as:

$$h^{ij} = h_{\gamma}(q + (1 - q)\delta^{ij}) \quad (2.26)$$

where  $\delta_{ij}$  is Kronecker's delta. The factor  $q$  describes the degree of latent hardening; for example,  $q=0$  indicates that only self-hardening occurs, so that slip in one system causes hardening only in the same system. A value of  $q=1$  indicates Taylor hardening, where activity in any slip system causes equal hardening in every other system. The instantaneous hardening coefficient,  $h_{\gamma}$ , depends on the previous deformation history. In the present model, the relationship between the accumulated slip in the grain,  $\gamma^{acc}$ , and the instantaneous hardening coefficient is described by an exponentially decreasing function:

$$h_{\gamma} = h_{final} \{1 + (h_{ratio} - 1) \exp(-h_{exp} \gamma^{acc})\} \quad (2.27)$$

where,  $h_{final}$ ,  $h_{ratio}$ , and  $h_{exp}$ , together with  $\tau^0$ , can be used as fitting parameters. In this formula,  $h_{final}$  is the final hardening coefficient,  $h_{ratio}$  is the ratio between the initial and final hardening coefficient, and  $h_{exp}$  is a parameter that describes the strength of the exponential term.

The self-consistent method for elastoplasticity is an incremental method, so the elastic-plastic instantaneous stiffness tensor for the grain,  $L_c$ , must be calculated at each step. Stress and strain can be related to each other using the elastic stiffness,  $L^E$ , or the elastic compliance,  $M^E$ , tensors.

$$\dot{\epsilon}_C = M_C^E \dot{\sigma}_C + \dot{\epsilon}_C^P \quad \text{or} \quad \dot{\sigma}_C = L_C^E (\dot{\epsilon}_C - \dot{\epsilon}_C^P) \quad (2.28)$$

Combining these equations together, the instantaneous elastic-plastic stiffness tensor for the grain and the slip on each active system,  $f^i$ , can be calculated:

$$\begin{aligned}
L_C &= L_C^E (I - \sum_m \mu^m f^m) \\
f^i &= \sum_k Y^{ik} L_C^E \mu^k \\
Y^{ik} &= (h^{ik} + \mu^i L_C^E \mu^k)^{-1}
\end{aligned} \tag{2.29}$$

Note that if all the potential slip systems are inactive then the instantaneous stiffness is equal to the elastic stiffness.

Now the stress and strain rates in the inclusions can be related to the stress and strain rates at infinity (the stress and strain rates of the HEM) by the concentration tensor,  $A_C$ , which can then be related to  $L^*$ , Hill's 'constraint' tensor. Hill's constraint tensor in turn relates to the Eshelby tensor,  $S$ , and the overall stiffness tensor,  $L$ .

$$\begin{aligned}
\dot{\epsilon}_C &= A_C \dot{\bar{\epsilon}} \\
A_C &= (L^* + L_C)^{-1} (L^* + L) \\
L^* S &= L(I - S)
\end{aligned} \tag{2.30}$$

The polycrystal stress and strain rates are equal to the weighted stress and strain rate averages over all the grains. At a certain stage of deformation, the stress, and thereby the potentially active slip systems in the constituents of the polycrystal, is known. The polycrystal is prescribed an additional strain rate, and, using this model, it is possible to determine the stress and strain rates as well as the instantaneous moduli for all of the individual grains. This then allows the polycrystal stress rate and stiffness to be calculated as the weighted average over all grains.

In their 1998 study [21], Clausen et al. examined the lattice strain development of three *fcc* materials (copper, aluminum, and steel) under uniaxial tension. They used Hutchinson's self-consistent model [22] for elastic-plastic materials, as described in detail in this chapter. The model is a 1-site rate-insensitive SCM. Since all the materials studied are *fcc*, the slip systems contributing to plasticity are  $\{111\} \langle 110 \rangle$ . The critical resolved shear stress (*CRSS*) obeys the hardening rule outlined earlier in this chapter in which three hardening parameters and the *initial CRSS* ( $\tau_0$ ) are used as fitting parameters to fit the macroscopic strain data.

Lattice strains were also calculated by the model and plotted versus applied stress. In the elastic regime, the lattice strains indicated more anisotropy in stainless steel than in copper, while the least elastic anisotropy was observed in aluminum. This is the expected result since the elastic anisotropy factor  $2C_{44}/(C_{11}-C_{22})$  is highest in stainless steel and lowest in aluminum.

The levels of anisotropy observed in the plastic regime were much larger than those in the elastic regime for all three materials. The 200 reflection showed the most unstable behavior, which also conforms to the ferroelectric data presented in Chapters 4 and 5.

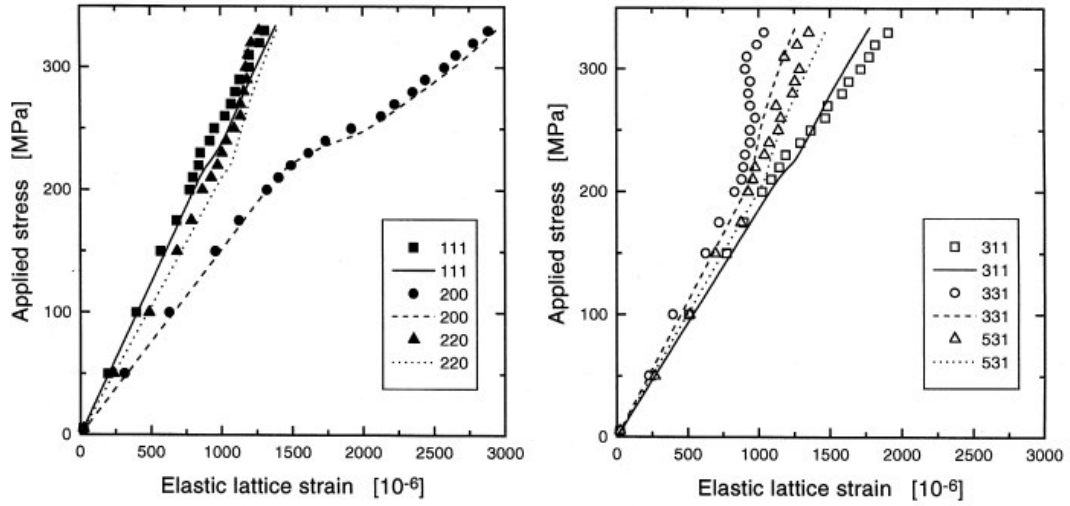
Clausen et al. did not present much comparison with experimental data in their paper. The only figure comparing the model's results with the experimental data was the one on page 3097 (Figure 2-6 below). Experimental results and model predictions in the

elastic regime match very well. In the plastic regime, matching is good for some  $hkl$  and not particularly satisfactory for others. However, the model was judged capable of providing good qualitative predictions. Considering the complex nature of plastic-deformation and the non-topological micromechanical nature of the model, this can be considered a successful result.

Although Clausen et al. did not explore the phenomenon at that time, predictions of texture development can also be made using this model by plotting the number of active slip systems on each subset of grains. They focused instead on the number of grains that contain a specific number of active slip systems. Most of the activity occurs during the first stages of plastic deformation, after which the numbers remain more or less constant.

Clausen's group also compared different lattice strains versus applied stress curves, and concluded that reflection 331 is a suitable one for stress-strain characterization, since it exhibits the most nearly linear response.

Later studies by the Los Alamos group [23, 24] proposed an improved Rietveld analysis to account for strain anisotropy. Details of this method are described in Chapter 4 of this thesis together with suggestions for further improvement.



(a) 111, 200 and 220 reflections.

(b) 311, 331 and 531 reflections.

Figure 2-6: Calculated (lines) and measured (symbols) stress-strain response parallel to the tensile axis for stainless steel. The experimental and modeling results have a good match in the elastic region. The results are less agreeable in the plastic regime. (Courtesy of B. Clausen)

# 3. Self-Consistent Modeling of Ferroelectrics

## 3.1 The Huber Model

The starting point of the modeling effort in this study is the model developed by Huber et al. [8] which uses domain wall motion as the basis of a microelectromechanical model. Domains are regions in which the spontaneous polarization and strain are homogenous and are separated from each other within a single crystal by mobile walls.

The basic equations governing the physical behavior of ferroelectrics were presented in Chapter 1. This section presents the assumptions in the model and how it can predict macroscopic behavior of ferroelectrics.

Grains (crystals) in this model interact via the self-consistent scheme, i.e., each grain only interacts with the homogenous matrix it is surrounded by. The matrix obtains its properties as a self-consistent average of properties of different grains.

The grains, hence the domains, are assumed to be uniformly distributed in space by three Euler angles defined for each grain. The Euler angles describe the orientation between the coordinate system of the grain and the laboratory coordinate system. And since different domains are aligned along the coordinate system of the grain, Euler

angles also define their direction with respect to the global axes, or the laboratory coordinate system.

Currently the model considers a perovskite-type, tetragonal, single-phase material. The material has a cubic unit cell above the Curie temperature, but below that temperature (e.g., at room temperature) it has a tetragonal unit cell with the center of positive and negative ionic charges not coinciding, hence resulting in an electrical dipole in the unit cell.

Each grain has six energetically equivalent variants (domains) in three perpendicular directions ( $I=1$  to  $6$ ). Each of the six variants can transform (switch) to any other five variants. Consequently thirty transformation systems are present ( $\alpha=1$  to  $30$ ).

The model also assumes that stress ( $\sigma$ ) and electric field ( $E$ ) in each variant are constant (i.e., the same) within a given grain. Strain ( $\epsilon$ ) and electric displacement ( $D$ ) of the grain are taken to be the volume average of  $\epsilon^L$  and  $D^L$  over the variants, plus the remnant strain and polarization due to switching.

Linear response ( $\epsilon^L$  and  $D^L$ ) in each variant can be related to the action ( $\sigma$  and  $E$ ) on the variant (which is the same as the action on the grain) by the following equation:

$$\begin{bmatrix} \epsilon^L \\ D^L \end{bmatrix} = \begin{bmatrix} S^I & d^I \\ d^I & \kappa^I \end{bmatrix} \begin{bmatrix} \sigma \\ E \end{bmatrix} \quad (3.1)$$

To calculate the strain and electric displacement in the grain averaging over all the variants is needed:

$$\begin{bmatrix} \boldsymbol{\varepsilon} \\ \boldsymbol{D} \end{bmatrix} = \begin{bmatrix} S^E & d \\ d & \kappa^\sigma \end{bmatrix} \begin{bmatrix} \boldsymbol{\sigma} \\ E \end{bmatrix} + \begin{bmatrix} \boldsymbol{\varepsilon}_r \\ P_r \end{bmatrix} \quad (3.2)$$

$$\begin{aligned} S_{ijkl}^E &= \sum_{I=1}^{I=M} \left[ c^I S_{ijkl}^{E(I)} \right] \\ d_{ijk} &= \sum_{I=1}^{I=M} \left[ c^I d_{ijk}^{(I)} \right] \\ \kappa_{ij}^\sigma &= \sum_{I=1}^{I=M} \left[ c^I \kappa_{ij}^{\sigma(I)} \right] \end{aligned} \quad (3.3-3.5)$$

Here  $\boldsymbol{\varepsilon}$  and  $\boldsymbol{D}$  are the strain and electric displacement response of the grain, respectively. The terms in the matrix ( $S^E$ ,  $d$ ,  $\kappa^\sigma$ : compliance, piezoelectricity coefficient, and electric permittivity, respectively) are the grain's electromechanical properties which are the volume averages of the corresponding domain properties ( $S^{E(I)}$ ,  $d^{(I)}$ ,  $\kappa^{\sigma(I)}$ ) as indicated by Equations (3.3–3.5). The first right-hand side term in Equation (3.2) is the linear response of the grain while the second right hand side term is the remnant part. The development of the remnant part is due to domain switching.  $c^I$  is the volume fraction of each domain present in the grain. Since in the tetragonal structure there are six different domains in each grain, the initial values of  $c^I$  are all assumed to be  $1/6$ .

Domain wall switching is a dissipative motion similar to dislocation plasticity. (Note that dislocation plasticity is neglected in this study.) Initially each domain in the crystal has an equal volume fraction ( $c^I=1/6$ ). This value changes as domains change

to one another, or switching occurs. A schematic of domain switching is illustrated in Figure 3-1. Here, the grain is assumed to have only two domains (variants), and the loading space has only one component: the shear stress.

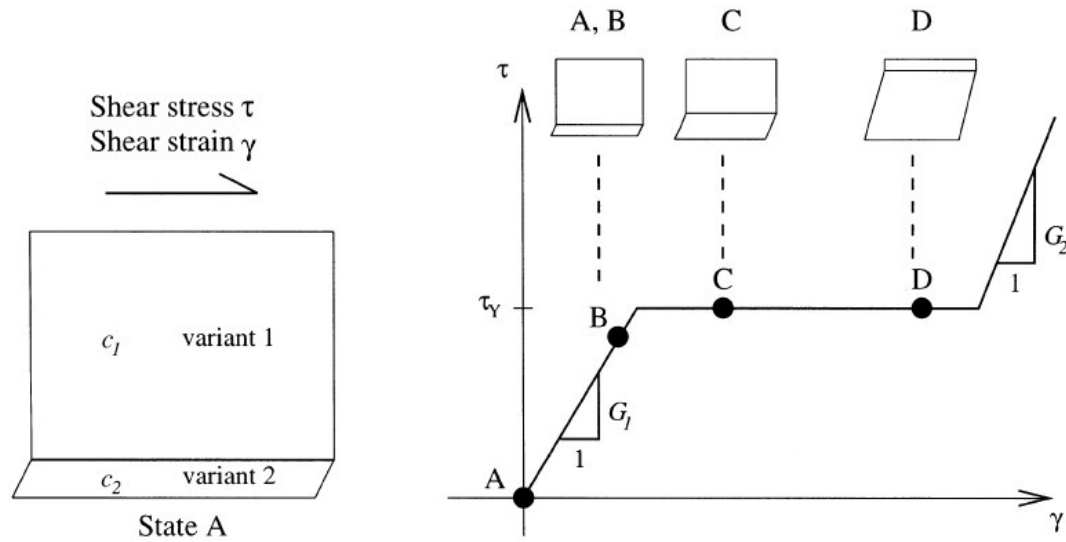


Figure 3-1: The progressive nature of ferroelectric transformation within a crystal due to domain wall motion. This simplified example has only 2 domains, and the loading space is one-dimensional. (Courtesy of C. Landis)

The challenge for ferroelectrics is to find the shape of the driving force function. If the loading were in the form of stress only, classical theories, such as von Mises could be used to combine different components of the stress tensor. But in ferroelectrics there exist not only six stress components, but also three components of the electric field vector. Domain walls move when the driving force on the corresponding transformation,  $G^\alpha$ , reaches a critical value,  $G_c^\alpha$ . The driving force is defined as the work conjugate of the rate of transformation,  $\dot{f}^\alpha$ , which are kinematic variables:

$$\dot{w}^D = \sum_{\alpha} [G^{\alpha} \dot{f}^{\alpha}]. \quad (3.6)$$

The dissipative work rate can be calculated as follows,

$$\dot{w}^D = \dot{w} - \dot{w}^s = \sigma_{ij} \dot{\epsilon}_{ij} + E_i \dot{D}_i - \dot{w}^s \quad (3.7)$$

$$\dot{w}^s = \sigma_{ij} (\dot{\epsilon}_{ij} - \dot{\epsilon}_{ij}^R) + E_i (\dot{D}_i - \dot{D}_i^R) - \sum_{\alpha} \left[ \frac{1}{2} \sigma_{ij} \tilde{\epsilon}_{ij}^{\alpha} + \frac{1}{2} E_i \tilde{D}_i^{\alpha} \right] \dot{f}^{\alpha} \quad (3.8)$$

$$\begin{aligned} \tilde{\epsilon}_{ij}^{\alpha} &\equiv \sum_I A^{I\alpha} [s_{ijkl}^{E(I)} \sigma_{kl} + d_{ijk}^{(I)} E_k] \\ \tilde{D}_i^{\alpha} &\equiv \sum_I A^{I\alpha} [d_{ikl}^{(I)} \sigma_{kl} + \kappa_{ik}^{\sigma(I)} E_k] \end{aligned} \quad (3.9-3.10)$$

$$A^{I\alpha} = \begin{cases} 1 & \dots \text{ If } \alpha \text{ increases } I \\ -1 & \dots \text{ If } \alpha \text{ decreases } I \\ 0 & \dots \text{ Otherwise} \end{cases} \quad (3.11)$$

$$\dot{c}^I = \sum_{\alpha=1}^N A^{I\alpha} \dot{f}^{\alpha}, \quad I = 1, 2, \dots, M \quad (3.12)$$

$$\tau^{\alpha} = \sigma_{ij} \mu_{ij}^{\alpha} \quad (3.13)$$

$$E^{\alpha} = E_i s_i^{\alpha} \quad (3.14)$$

Here,  $\dot{w}$  is the total energy rate, and  $\dot{w}^s$  is the elastic energy rate.  $\tau_i$  and  $E_i$  are resolved shear stress and electric field on each transformation, respectively.  $s_i$  and  $n_i$  are vectors specifying the orientation of different variants, and  $\mu_{ij}$  is the Schmid vector.  $A^{i\alpha}$  is a matrix defining what each transformation does, or in the course of transformation  $\alpha$ , which variant transforms to which other one.

Thus the equation defining the driving force on each transformation system would be:

$$G^{\alpha} = \tau^{\alpha} \gamma^{\alpha} + E^{\alpha} P^{\alpha} + \frac{1}{2} \sigma_{ij} \tilde{\epsilon}_{ij}^{\alpha} + \frac{1}{2} E_i \tilde{D}_i^{\alpha}. \quad (3.15)$$

Defining the work hardening as,

$$\dot{G}_c^\alpha = \sum_{\beta} H^{\alpha\beta} \dot{f}^\beta . \quad (3.16)$$

The loading and unloading condition on each transformation system would be:

$$\begin{aligned} G^\alpha = G_c^\alpha \quad \text{and} \quad \dot{G}^\alpha = \dot{G}_c^\alpha &\Rightarrow \dot{f}^\alpha \geq 0 \\ G^\alpha = G_c^\alpha \quad \text{and} \quad \dot{G}^\alpha < \dot{G}_c^\alpha &\Rightarrow \dot{f}^\alpha = 0 \end{aligned} \quad (3.17)$$

Huber et al. [8] used this model to predict the macroscopic behavior of ferroelectrics.

The characteristic hysteresis loop and butterfly curves for ferroelectrics could be qualitatively predicted by the model, as can be seen in Figure 3-2.

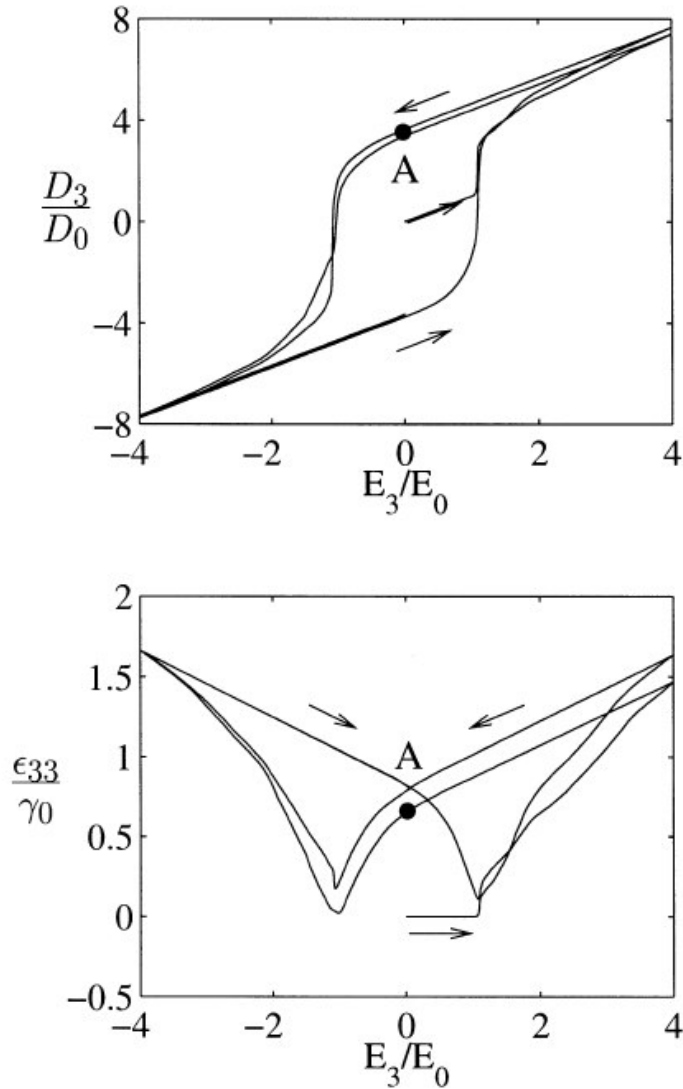


Figure 3-2: Self-consistent model estimates of the electrical displacement (top) and the strain (bottom) responses of a ferroelectric polycrystal to cyclic electric field loading [8]

One of the goals of the present study is to validate the Huber model using diffraction data. This required some changes in the model so that it could be used for calculating lattice strain and texture evolution. A FORTRAN code provided by C. Landis and based on the formulation presented above was used as a starting point. The changes made in the present study are described in the next section while the comparison to experimental data is presented in Chapter 5.

## 3.2 The New Self-Consistent Model

### 3.2.1 Grain Selection and Average Lattice (*hkl*) Strain

The diffraction data include lattice plane spacings (*d*-spacings) yielding *hkl*-dependent lattice strain evolution under loading. To study *hkl*-dependent properties of the material, the domains (or grains in general) which satisfy the Bragg's law – the diffraction condition (i.e., those that will contribute to the diffraction pattern) should be selected and averaged over. This capability was incorporated into the new model.

To select the domains contributing to a specific reflection, the *hkl* vector (i.e., the lattice plane normal) of the domain should lie within a certain solid angle cone of the scattering vector of a given detector. The reason is that a detector in a diffraction experiment usually collects the diffracted beam through a solid angle cone called the acceptance angle. The value of the acceptance angle changes from detector to detector. The majority of the diffraction data presented here was collected at the ENGIN X instrument of ISIS Neutron Scattering Facility, Rutherford-Appleton Laboratory, UK. Here, the acceptance angle is 5°, the value also used in the new model. Figure 3-3 shows the experimental setup at ENGIN X. The data presented in this study came from the left detector ( $2\theta = -90^\circ$ ). The scattering vector, therefore, would be  $Q_{||}$ . As a result, the 002 reflection, for instance, would come from domains with their unit cell *c*-axis parallel to the loading axis.

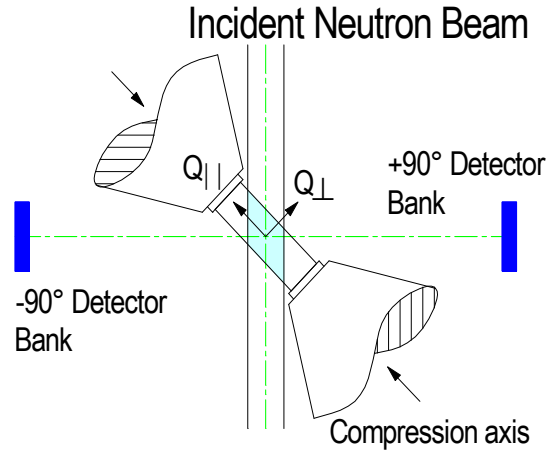


*Figure 3-3: Schematic of the experimental setup at ENGIN X. The diffracted neutrons are collected by two  $2\theta = \pm 90^\circ$  detectors with scattering vectors corresponding to the longitudinal and transverse directions of the specimen.*

Figure 3-4 shows the mechanism of selecting domains that contribute to a given reflection. The new model identifies domains that have their  $hkl$  plane normal within the acceptance angle of a detector. The number of domains identified this way is counted such that each unit of  $1/6^{\text{th}}$  of a grain volume is counted as a single domain. It then averages their strains to obtain the  $hkl$  strain along the sample direction given by that detector. It should be noted that this is different from averaging the strain in the domains present in a grain to obtain the average grain strain.

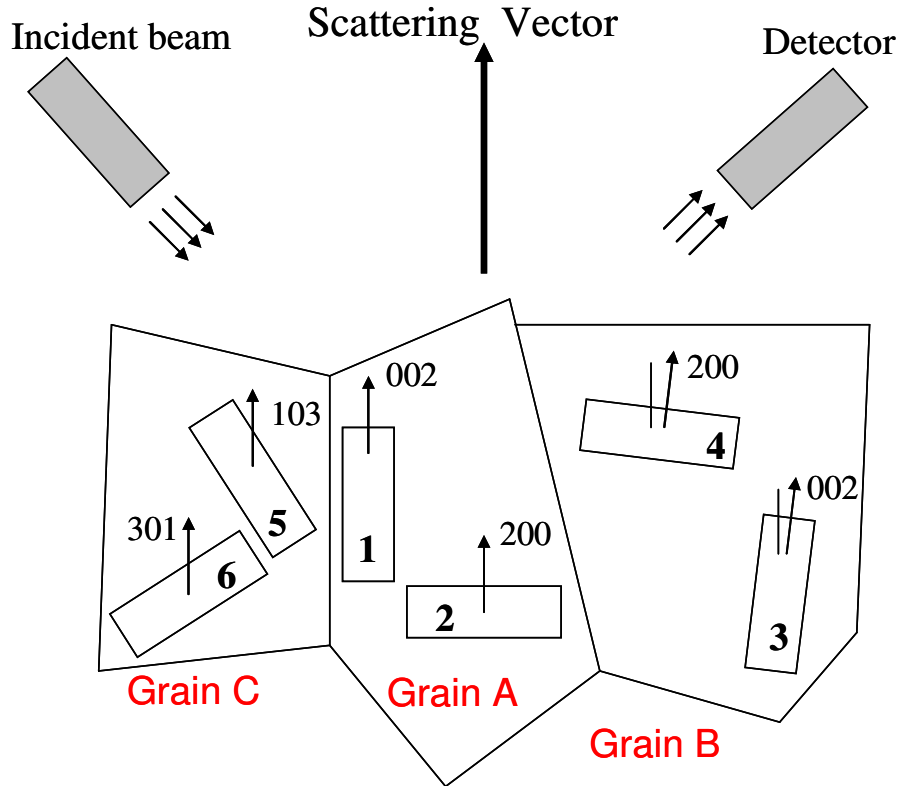


Figure 3-4: The domain selection mechanism incorporated into the new model. The  $[002]$  direction in domain 1, the  $[200]$  direction in domain 2, the  $[103]$  direction in domain 5, and the  $[301]$  direction in domain 6 are perfectly aligned with the scattering vector. The  $[002]$  and  $[200]$  directions in domains 3 and 4 are not exactly aligned with the scattering vector, but they lie within a  $5^\circ$  cone of it; so they also contribute to the diffraction pattern. If these were the only grains in the material lattice strain  $[002]$  would be the average of the strains in domains 1 and 3, the strain along  $[200]$  would be the average of domains 2 and 4, the strain along  $[103]$  would be equal to the strain of domain number 5, and the strain along  $[301]$  would be equal to that of domain number 6.

Calculating the above-mentioned averages is not trivial, bringing up another capability added to the new model. Sometimes all of the domains chosen for a specific  $hkl$  direction would switch out of that direction due to application of stress or electric field, thus calculating the average strain over those domains becomes impossible. To avoid this problem, a “domain-locking” mechanism was added to the

new model. This mechanism assures that even if the driving force on a specific transformation is more than the critical value resulting in all the domains to move out of a specific  $hkl$  direction, the transformation will not be activated. This way, there will always be domains that satisfy the diffraction condition and contribute to a reflection. While this “domain-locking” mechanism is somewhat artificial, it assures the presence of diffraction peaks throughout a loading experiment, a consistent fact in all diffraction data. The percentage of the domains which cannot be switched can be specified as a variable parameter in the program. The present study usually assumed 10% of the initially present domains will be locked (unless it is stated otherwise).

Another capability added to the new model is the ability to define texture. The original Huber model had the grains oriented along uniformly distributed directions. In the new model, one can define any texture at the beginning of the analysis.

### **3.2.2 The Problem of Reverse Switching**

It was noticed that under certain conditions, i.e., low  $G_c^a$  values (Equation (3.17)), domains that switched earlier under mechanical loading would tend to switch back using the original Huber model. The following describes the origin of this problem and the solution offered in the new model. The applied force space has nine components: six stress components ( $\sigma_{11}$ ,  $\sigma_{22}$ ,  $\sigma_{33}$ ,  $\sigma_{12}$ ,  $\sigma_{13}$ , and  $\sigma_{23}$ ), and three electric field components ( $E_1$ ,  $E_2$ , and  $E_3$ ). To find out the shape of the driving force function defined over these nine variables, the dissipated energy, and the work conjugate of the kinematic variable were calculated. Although it yields a way to combine the stress

with electric field, this approach causes a problem as explained below. The equation from which one can obtain the driving force for each transformation system is Equation (3.15).

All the variables in Equation (3.15) are defined at the grain level (i.e., none of them are variables related to the HEM). Therefore, only one grain is considered here, and it does not matter what is happening in the rest of the material. The matrix-grain constraint effects should be already taken into account. For simplicity, let us assume  $E^\alpha = E_i = 0$  and  $\sigma_{ij} = 0$  except for  $i=j=1$ , so the grain is under mechanical loading parallel to axis 1. This simplifies Equation (3.15) into:

$$G^\alpha = \tau^\alpha \gamma^\alpha + \frac{1}{2} \sigma_{ij} \tilde{\varepsilon}_{ij}^\alpha. \quad (3.18)$$

Substituting  $\tau^\alpha = \sigma_{ij} \mu_{ij}$  and  $\tilde{\varepsilon}_{ij}^\alpha = \sum_l A^{l\alpha} s_{ijkl}^l \sigma_{kl}$  yields:

$$G^\alpha = \sigma_{ij} \mu_{ij} \gamma^\alpha + \frac{1}{2} \sigma_{ij} \sum_l A^{l\alpha} s_{ijkl}^l \sigma_{kl}. \quad (3.19)$$

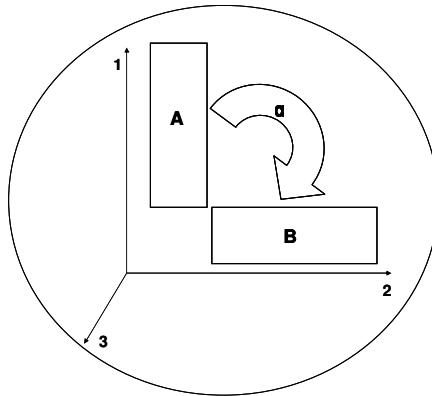


Figure 3-5: Schematic of two domains in a grain. Domain A is along direction 1, and domain B is along direction 2. Transformation  $\alpha$  is defined as switching of A to B.

Transformation ' $-\alpha$ ' would be switching of B to A.

Defining transformation “ $\alpha$ ” so that it changes variant A to variant B as described in Figure 3-5, reduces  $G^\alpha$  further. Here,  $\mu_{ij}$  has the form of

$$\mu_{ij} = \begin{pmatrix} \frac{1}{2} & 0 & 0 \\ 0 & \frac{1}{2} & 0 \\ 0 & 0 & 0 \end{pmatrix}. \quad (3.20)$$

Note that  $s_{ijkl}^I \sigma_{kl} \sigma_{ij}$  is zero except for  $s_{1111}^I \sigma_{11} \sigma_{11}$ .  $A^{I\alpha}$  is zero except for

$A^{B\alpha} = -A^{A\alpha} = 1$ . Hence one obtains:

$$G^\alpha = -\frac{\gamma^\alpha}{2} \sigma_{11} - \frac{(s_{1111}^A - s_{1111}^B)}{2} \sigma_{11}^2. \quad (3.21)$$

For an isotropic material  $G^\alpha$  will reduce to  $G^\alpha = -\gamma^\alpha \sigma_{11} / 2$ , which is a linear function of applied stress, while for an anisotropic material, Equation (3.21) is quadratic. Based on the value of the critical driving force,  $G_c^\alpha$  two different cases are possible, each described in Figures 3-6 and 3-7.

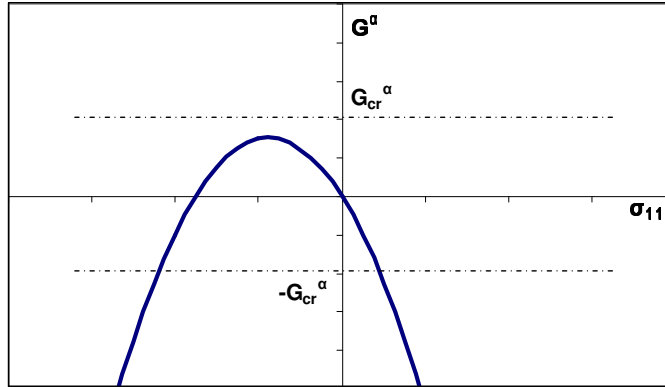


Figure 3-6: Plot of Equation (3.21) - the driving force for transformation ‘ $\alpha$ ’ versus applied stress,  $\sigma_{11}$ . Whether  $\sigma_{11}$  increases in tensile or in compressive directions, the transformation ‘ $\alpha$ ’ will not take place. Instead the transformation ‘ $-\alpha$ ’ will occur, no matter what the sign of  $\sigma_{11}$  is. Referring to Figure 3-5, it is clear that the transformation ‘ $-\alpha$ ’ will be physically meaningless under this applied compressive stress.

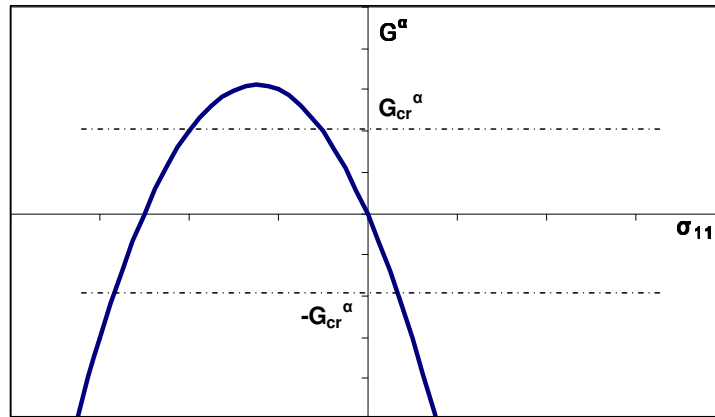


Figure 3-7: Same as in Figure 3-6, except the relative value of  $G_c^\alpha$  is smaller. As compressive stress along direction 1 is increased transformation ‘ $\alpha$ ’ occurs as expected. Increasing compressive  $\sigma_{11}$  even further causes a transformation in the ‘ $-\alpha$ ’ direction, which is an unrealistic case.

In the first case (Figure 3-6), regardless of the sign of the applied stress  $\sigma_{11}$  only the transformation in direction “ $-\alpha$ ” can occur. In the second case (Figure 3-7), with a positive  $\sigma_{11}$ , transformation in the “ $-\alpha$ ” direction will occur, which is intuitive. But when  $\sigma_{11}$  assumes negative values, first the transformation in the “ $\alpha$ ” direction

occurs, and later the transformation in the “ $-\alpha$ ” direction is expected. The latter, of course, is unrealistic. Unfortunately, this latter case was observed as reverse switching in some of the runs of the Huber model (see Figures 3-8 and 3-9). Since the model employs an energy minimization method, the variants want to switch to the one with less energy, and since the relationship between the elastic energy and the stress is quadratic, positive and negative stresses have the same effect.

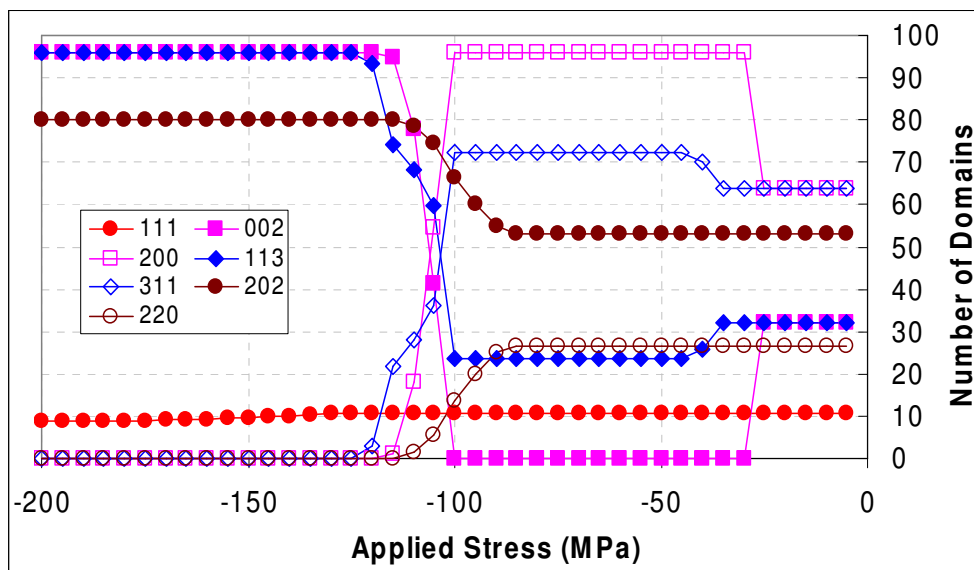


Figure 3-8:  $BaTiO_3$  domain switching under applied uniaxial compressive stress predicted by the original Huber model. The number of domains selected for each reflection (i.e., those that diffract into the longitudinal detector) is plotted versus applied stress. As the load increases domains start to switch. This figure shows that the first switching starts at  $-30$  MPa, and domains in the  $[002]$  direction are switched to domains in  $[200]$ . Exactly the same number of domains which are switched out of a direction is switched into the twin direction. Reverse switching is observed at about  $-100$  MPa. At this load level  $[200]$  domains start to switch back into  $[002]$  domains. This seems counterintuitive.

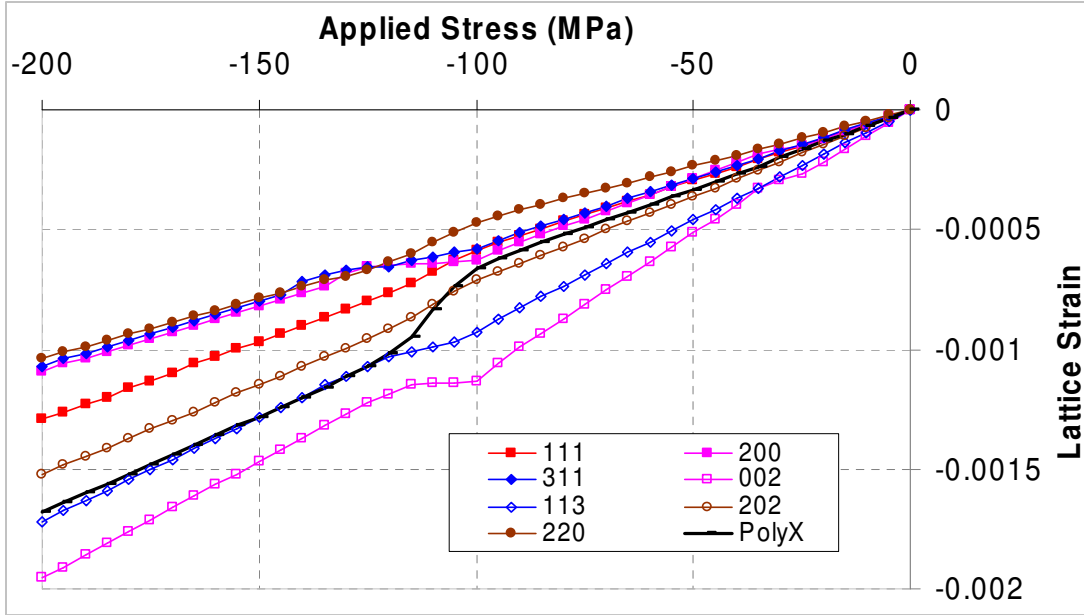


Figure 3-9: Lattice ( $hkl$  dependent) and total polycrystalline (elastic and remnant) strains as a function of applied stress for the case explained in Figure 3-8. Nonlinear behavior is observed near  $-20$  and,  $-100$  MPa. It is more noticeable around  $-100$  MPa where lots of switching occurs (both regular and reverse).

One way to fix the problem would be to use the approach employed in Equation (3.15), but simplify it by ignoring the last two terms (i.e., considering them high-order terms with negligible influence). This yields the following equation for the driving force:

$$G^\alpha = \tau^\alpha \gamma^\alpha + E^\alpha P^\alpha \quad (3.22)$$

where all the terms are defined as before. This way, the driving force is a function of all nine components of loading, and furthermore, both terms are linear with respect to stress and electric field, thus making reverse switching impossible. Using Equation (3.22) for driving force and implementing it in the new model the results shown in Figure 3-10 are obtained. Here, the  $x$ -axis is the applied stress while the  $y$ -axis is the number of domains contributing to a specific  $hkl$  reflection. In early stages of

increasing the load (around  $-10$  MPa), the switching in the (200) / (002) doublet starts. As load increases the number of domains in the (002) curve keeps decreasing and exactly the same number of domains is added to the (200) curve. This is an indication of (002) domains switching to (200) domains due to the applied stress. The (113) / (311) doublet starts switching at a higher stress, but shows the same behavior, i.e., the increase in (311) is exactly equal to the decrease in (113). And (202) / (220) doublet is the last one to start switching. This again confirms the experimental results, and the conclusion that the closer the axis of a doublet to the loading axis, the earlier the switching will start (to be explained again later). More interpretation of the results in this figure will be presented in Chapter 5.

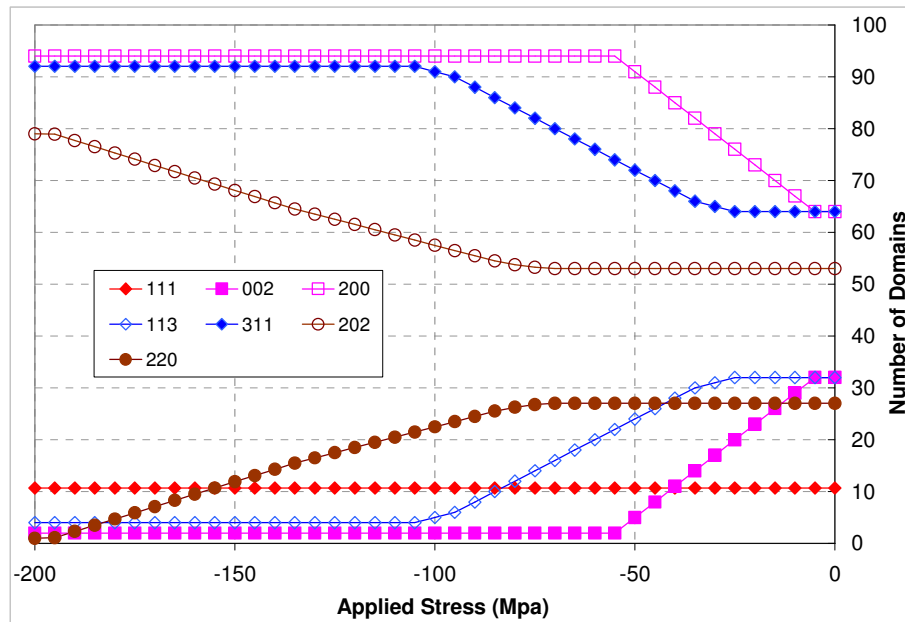


Figure 3-10:  $BaTiO_3$  domain switching under applied uniaxial compressive stress predicted by the new model. The number of domains selected for each reflection (i.e., those that diffract into the longitudinal detector) is plotted versus applied stress. As the load increases, domains begin to switch starting with the (002) / (200) pair. Unlike the original model, however, the new model does not predict reverse switching.

# 4. Neutron Diffraction Experiments

## 4.1 Introduction

Neutron diffraction is an ideal probe of bulk crystallographic structure, but so far in the realm of ferroelectrics, studies have mostly concentrated on probing the temperature-composition-structure relationship to obtain a clear understanding of the nature of the various phase transitions [25]. Recently, some studies have begun to use neutrons for monitoring texture development in ferroelectrics using specimens manipulated *ex situ* [12-15, 26]. Rogan et al. [25] have reported on the first *in-situ* bulk crystallographic study of the ferroelastic behavior of a multiphase, polycrystalline PZT under compressive loading. The present thesis, however, investigates the behavior of single phase tetragonal BaTiO<sub>3</sub>. This material was largely chosen as a model system (its single crystal stiffness tensor is known in contrast to that of PZT), but it also exhibits useful piezoelectric properties.

In the present study, the diffraction data are analyzed using a number of techniques. Single-peak fitting is the most accurate method for calculating lattice strains and it involves a minimum number of assumptions in the analysis. Sometimes, though, the use of single-peak method is not possible. This happens when, e.g., one peak of a tetragonal doublet attains very low intensities due to extensive domain switching. In this case, the multi-peak Rietveld refinement is more advantageous since it combines the contributions of several diffraction peaks to determine various crystallographic

parameters such as lattice constants, etc. However, it will be shown below that the Rietveld method should be used with great caution when high strain anisotropy is involved as is the case with ferroelectrics. An improved Rietveld method is presented and utilized here to capture the anisotropic behavior of BaTiO<sub>3</sub>. Guidelines on how to implement it on materials with other crystal structures are also presented.

#### 4.2 Experimental Setup and Sample Properties

The experiments were conducted at the ENGIN X beamline of ISIS [27, 28] Neutron Scattering Facility, Rutherford-Appleton laboratory, UK. This beamline is optimized for the measurement of strain, and thus stress, deep within a crystalline material by employing lattice planes as 'strain gauges'. The experimental setup was shown earlier in Figure 3-3. Figure 4-1 highlights the sampling volume in Figure 3-3 and the lattice planes interrogated by the incident neutron beam and the corresponding detectors.

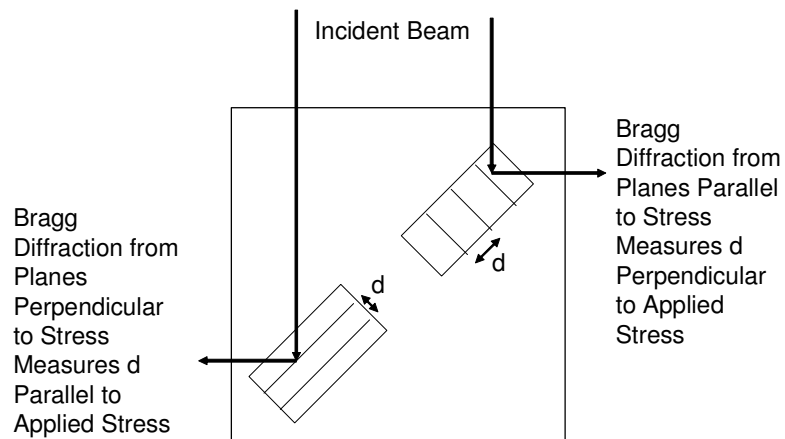


*Figure 4-1: A closer schematic of the sampling volume in Figure 3-3. Lattice planes and their  $d$ -spacings sampled by the longitudinal and transverse detectors are highlighted.*

Cylindrical bars of polycrystalline BaTiO<sub>3</sub> were placed under uniaxial compression up to –300 MPa. Samples were oriented at a Bragg angle of  $\theta = 45^\circ$  to the incident beam (Figure 3-3) allowing the  $2\theta = \pm 90^\circ$  detectors to measure the longitudinal and transverse sample response. In this thesis, all results and references are related to the longitudinal direction unless stated otherwise. In this case the scattering vector and the loading axis will always be parallel, so they will sometimes be referred to interchangeably. Hot-pressed BaTiO<sub>3</sub> was obtained from Alpha Ceramics Inc., (5121 Winnetka Avenue North, Minneapolis, MN 55428, USA). The BaTiO<sub>3</sub> of grade EC-31 was obtained in bulk form in the unpoled state and diced using a diamond wafering saw to produce specimen of 6 x 6 x 14 mm. The samples were separated from the loading fixture using 7 x 7 x 4 mm stainless steel spacers.

Lattice (*d*-) spacings are related to the neutron wavelength,  $\lambda$ , and hence the time-of-flight (TOF), through the Bragg's law:

$$n\lambda = 2d \sin \theta \quad (4.1)$$

Since the spallation (or TOF) neutron diffraction employed here generates a polychromatic beam, this equation means that multiple *d*-spacings are measured simultaneously while the Bragg angle ( $\theta$ ) is kept constant. Therefore, the diffraction data consisted of multi-peak patterns from sample directions either parallel or perpendicular to the loading axis. Figure 4-2 gives an example of neutron data from BaTiO<sub>3</sub> plotted as intensity vs. TOF or *d-spacing*. The latter was calculated using the *GSAS* analysis software [16]. Additional details on data analysis of TOF neutron diffraction data can be found elsewhere [29].

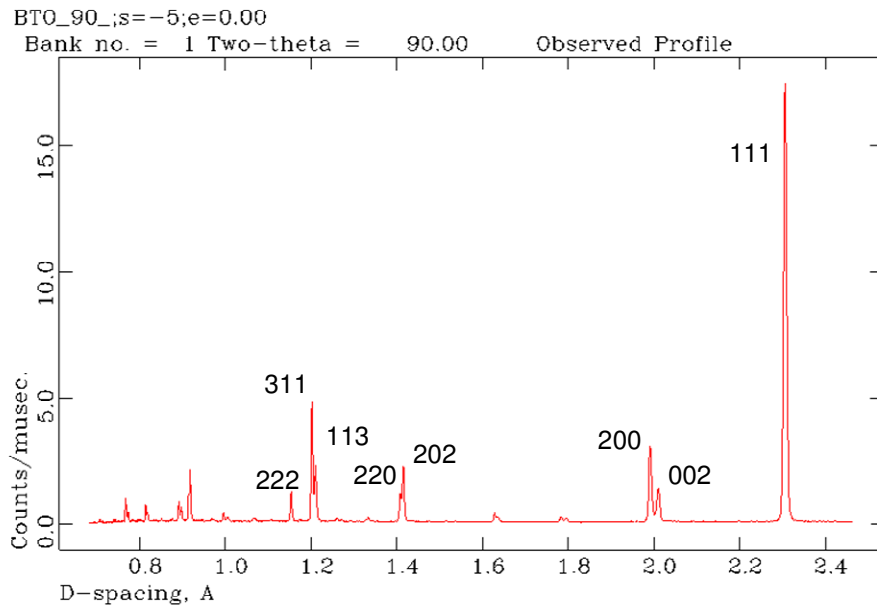
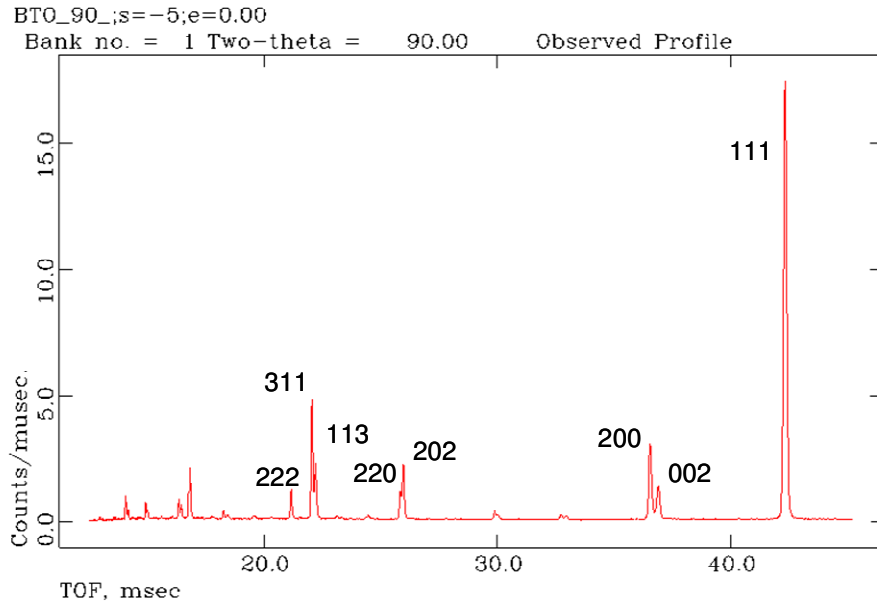


Figure 4-2: Diffraction spectra from a time-of-flight neutron diffraction experiment at ENGIN X using an unloaded  $\text{BaTiO}_3$  polycrystal. The x-axis is either in terms of time-of-flight (a) or d-spacing (b), while the y-axis is the intensity of the diffracted neutrons in terms of counts per microsecond.

Once the diffraction data are reduced and normalized to correct for appropriate instrument artifacts, the next challenge is the calculation of lattice strain. Different approaches can be used to achieve this goal and are presented in the next section together with their advantages and disadvantages.

### 4.3 Calculating Lattice Strains: the Single-Peak Method

In all methods of calculating lattice strains the same basic equation is used [29-31]:

$$\varepsilon_{hkl} = \frac{d_{hkl} - d_{hkl}^0}{d_{hkl}^0} . \quad (4.2)$$

The difference comes in the way lattice spacings,  $d_{hkl}$  are calculated. One approach is to use the single-peak fitting method. This is the most natural way of calculating the lattice strains since it involves minimal assumptions, but sometimes the intensity of certain peaks become so low that they are not distinguishable from the noise, making single-peak fitting difficult, erroneous, or impossible. In the single-peak method, the position of a specific peak is approximately decided at the beginning, and then a peak profile is fitted to that peak, and only that peak, to find its exact location, width, and other properties. This procedure is completely independent of any other peak observed in the spectrum. In practice when peaks appear as doublets, the two of them can be fitted simultaneously, but still the fitting is independent of all other peaks in the spectrum, and hence still considered single-peak fitting. For example, in Figure 4-3 the (002) and (200) peaks have been fit simultaneously. There are no assumptions about the lattice parameters of the sample or on the behavior of other peaks. Different

instruments have different peak profiles to be fitted, and these profiles have different numbers of fitting parameters. The most common parameters are peak position, peak intensity, and peak width. Peak position is used in calculating lattice strains, and peak intensity is used in texture analysis. The peak profile function used in this thesis is profile type number 3 in the *RAWPLOT* module of *GSAS*, which is an exponential pseudovoigt convolution (Von Dreele, 1990, unpublished) [16]. The results of this analysis are presented and discussed in Chapter 5.

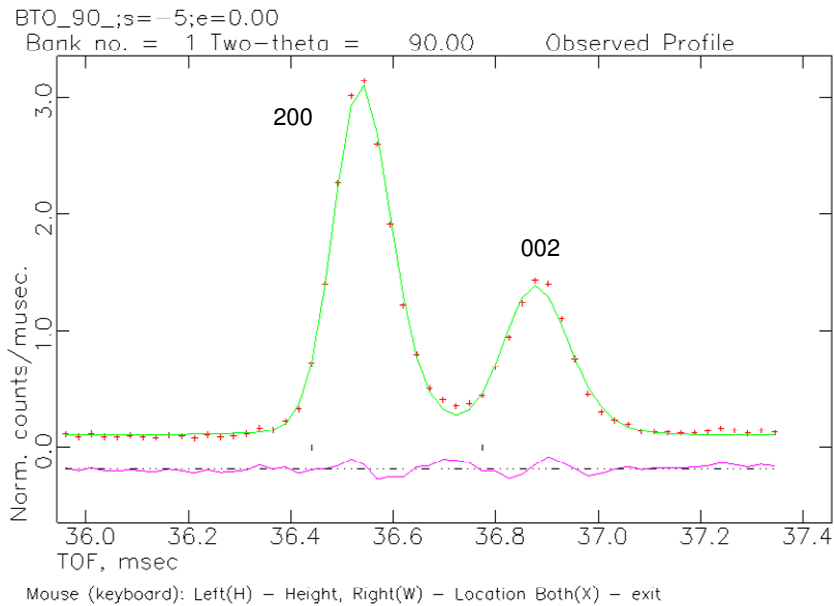
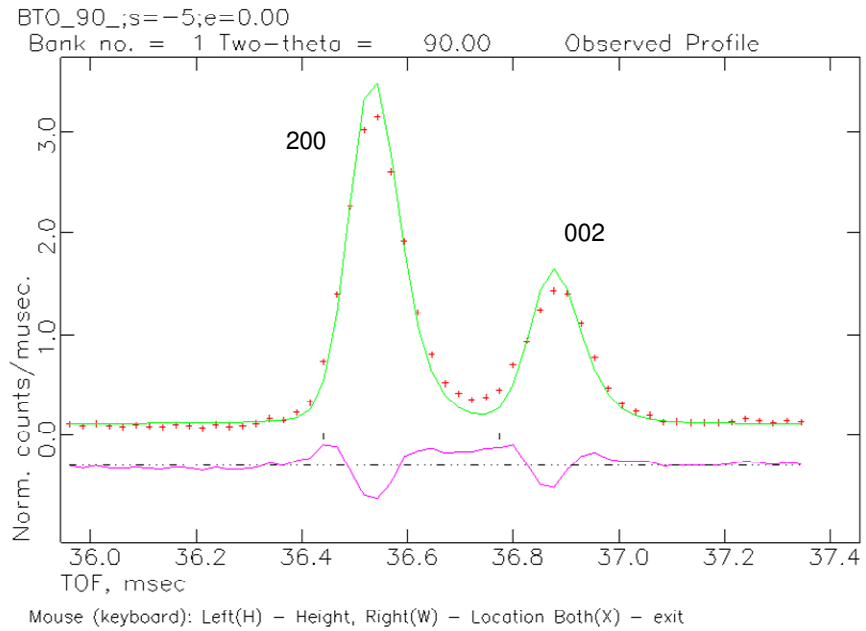


Figure 4-3: Single-peak fitting to reflections (200) and (002) of  $\text{BaTiO}_3$ . (a) Raw data and the fitted peak with peak position and intensity refined. (b) Peak width is added to the fitted parameters and a better fit is achieved ( $R_p = 3.5\%$ ,  $\chi^2 = 1.2$ , where  $R_p$  is the minimum achievable pattern residual, and  $\chi^2$  is the chi-square goodness-of-fit).

#### **4.4 Calculating Lattice Strains: the Rietveld Method**

The Rietveld method uses a least-squares approach to refine a theoretical crystallographic model until it matches the measured diffraction pattern. The introduction of this technique was a significant step forward in the diffraction analysis of powder samples as, unlike other techniques at that time, it was able to deal reliably with strongly overlapping reflections. The method was first reported [32] for the diffraction of monochromatic neutrons. The technique is equally applicable to alternative diffraction techniques such as x-rays or spallation (TOF) neutrons.

In the Rietveld method, least-squares refinements are carried out until the best fit is obtained between the entire observed powder diffraction pattern and the entire calculated pattern based on simultaneously refined models for crystal structure(s), instrumental factors, and other specimen characteristics such as lattice parameters. Some advantages of a full-pattern analysis (as compared to single-peak analysis) include [29]:

1. All reflections in the pattern are included without considering overlap.
2. The background is better defined, since a continuous function is fitted to the whole pattern.
3. The effects of preferred orientation and extinction are reduced since all reflection types are considered. Appropriate parameters can be refined as part of the analysis.
4. Crystal structure and peak-profile parameters can be refined as part of the same analysis, so the physical and chemical details of the phases are adjusted.

5. The calibration constants are computed rather than collected by laborious experimentation.
6. Quantitative measures of anisotropy can be extracted from the analysis. (This point is very important to the present study and will be discussed in detail later in this chapter.)

In the least-squares refinement, the residual  $S_y$  is minimized:

$$S_y = \sum_i w_i (y_i - y_{ci})^2 \quad (4.3)$$

where,  $w_i = 1/y_i$ ,  $y_i$ : observed intensity at the  $i^{\text{th}}$  step,  $y_c$ : calculated intensity at the  $i^{\text{th}}$  step.

A powder diffraction pattern of a crystalline material may be considered as a combination of individual reflection profiles with a peak height, a peak position, and an integrated area which is proportional to the Bragg intensity  $I_{hkl}$ , where  $hkl$  stands for Miller indices. Typically, several Bragg reflections may contribute to the observed intensity at an arbitrary point in the pattern. The calculated intensities are determined from the absolute value of structure factor  $|F_K|^2$  which is the sum of contributions of neighbor Bragg reflections and the background.

So the calculated intensity,  $y_{ci}$  becomes:

$$y_{ci} = s \sum_K L_K |F_K|^2 \phi(2\theta_i - 2\theta_K) P_K A + y_{bi} \quad (4.4)$$

where,  $s$  is the scale factor,

$L_K$ : composed of Lorentz, polarization and multiplicity factors,

$\phi$ : the reflection profile function,

$P_K$ : the preferred orientation function,

$A$ : an absorption factor,

$Y_{bi}$ : the background intensity at the  $i^{\text{th}}$  step.

The effective absorption factor,  $A$ , while it depends on the instrument geometry, is usually considered to be constant for most x-ray diffractometers. The least-squares minimization procedure leads to a set of normal equations involving derivatives of all of the calculated intensities,  $y_{ci}$ ; with respect to each adjustable parameter and the inversion of the normal matrix  $M_{jk}$  gives the solution

$$M_{jk} = -\sum_i 2w_i \left[ (y_i - y_{ci}) \frac{\partial^2 y_{ci}}{\partial x_j \partial x_k} - \left( \frac{\partial y_{ci}}{\partial x_j} \right) \left( \frac{\partial y_{ci}}{\partial x_k} \right) \right] \quad (4.5)$$

where  $x_j, x_k$  are the same set of adjustable parameters. The first term  $(y_i - y_{ci})$  can be neglected. If  $m$  is the number of refined parameters, an  $m \times m$  matrix is created and inverted with an iterative procedure with the shifts,  $\Delta x_k$  since the residual function is nonlinear:

$$\Delta x_k = \sum M_{jk}^{-1} \frac{\partial S_y}{\partial x_k} \quad (4.6)$$

Then calculated shifts are applied to the initial parameters to produce an improved model and the whole procedure is repeated. Since the adjustable parameters and intensities are related to each other in a nonlinear way, the starting model must be

close to the correct model or the nonlinear least squares will not converge to a global minimum. Rather, the procedure will either diverge or lead to a false minimum.

The Rietveld refinement process adjusts the refined parameters until the residual is minimized to obtain the best fit between the entire calculated and observed patterns. For this reason several “ $R$  values” or residuals have been developed for the Rietveld method. The most common of these are the minimum achievable pattern residual,  $R_p$ , and the weighted pattern residual,  $R_{wp}$  defined as:

$$R_p = \frac{\sum |y_i(obs) - y_i(calc)|}{\sum y_i(obs)} \quad (4.7)$$

$$R_{wp} = \left\{ \frac{\sum w_i (y_i(obs) - y_i(calc))^2}{\sum w_i (y_i(obs))^2} \right\}^{1/2} \quad (4.8)$$

where,  $y_i(obs)$  and  $y_i(calc)$  are the observed and calculated intensity at the  $i^{th}$  step, respectively, and  $w_i = 1/y_i$ .

In this thesis, Rietveld analysis was conducted using the *GSAS* software [16].

Rietveld refinement, as opposed to single-peak fitting, relies upon the physics of the problem, and a complete intensity of the diffracted neutron intensity versus time-of-flight or  $d$ -spacing is calculated based on refining some or all of the following material data: convergence criteria, number of phases, lattice symmetry for each phase, lattice parameters for each phase, atoms in unit cells, atom positions in unit cells, atom occupancies, thermal motion parameters, background function type, background function coefficients, diffractometer constants, absorption/reflectivity correction, phase fractions, histogram scaling factors, peak profile type and

coefficients, relevant constraints, and preferential orientations. The parameters found to have the most pronounced influence in this study are: number of phases, lattice symmetry for each phase, lattice parameters for each phase, atoms in unit cells, atom positions in unit cells, atom occupancies, and preferential orientations. Table 4-1 lists some of the initial values used as a starting point for the refinements of BaTiO<sub>3</sub> data [25].

Space Group:	P 4 m m
Laue Class:	4 / mmm
Lattice Parameters:	$a = b = 3.98 \text{ \AA}$ $c = 4.02 \text{ \AA}$ $\alpha = \beta = \gamma = 90^\circ$
Fractal (Atomic) Coordinates:	Ba:    0    0    0 Ti:    0.5 0.5 0.5 O1:    0.5 0.5 0 O2:    0.5 0 0.5

*Table 4-1: Initial values used as a starting point for Rietveld refinements in BaTiO<sub>3</sub> experiments.*

Figure 4-4 shows the same material studied in Section 4.3, but this time the data are fitted with Rietveld refinement. Figure 4-3b zooms in on doublets (200)/(002). The fit

appears as good as the single peak fit in Section 4.3, but this will cease when load increases and the intensity ratio starts to change dramatically (see Chapter 5).

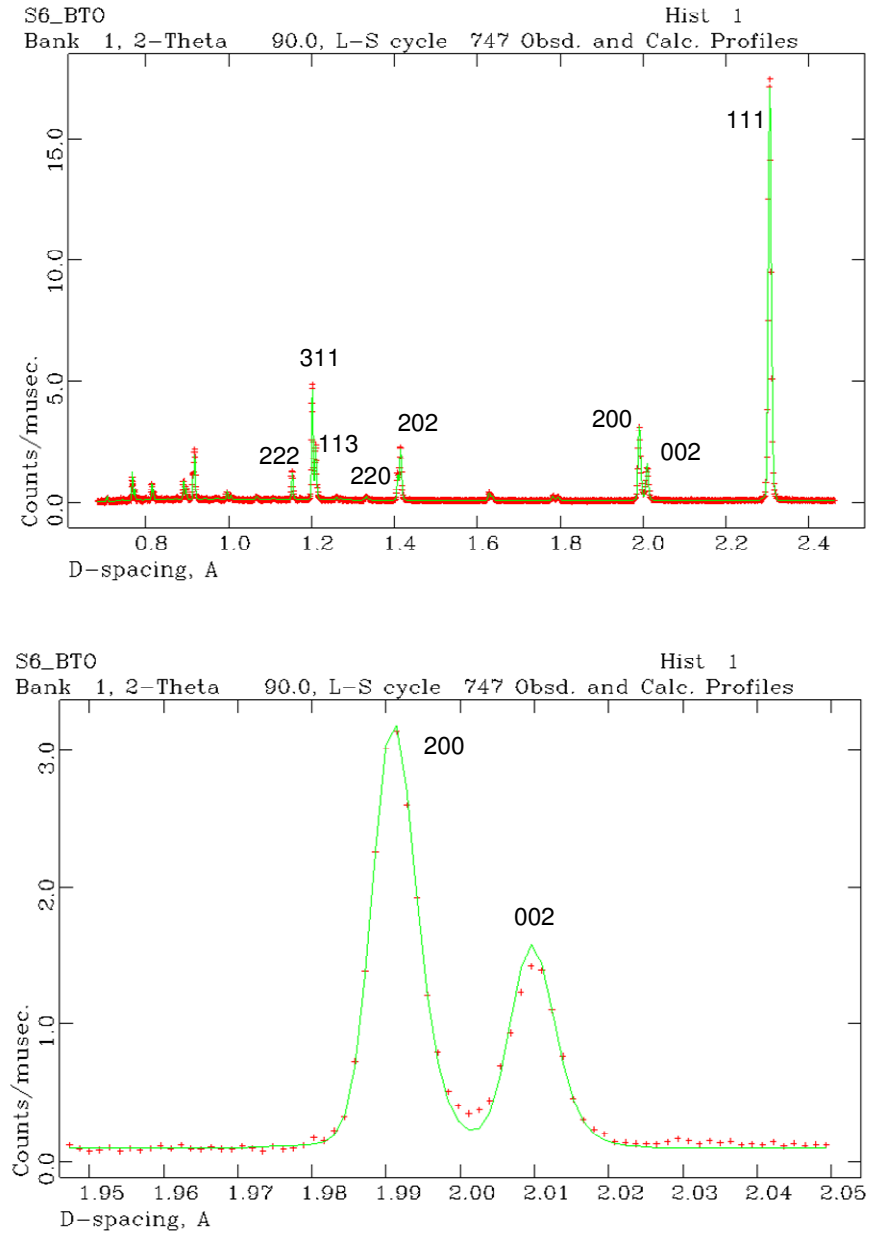


Figure 4-4: (a) A full-pattern Rietveld fit to the diffraction data from a  $\text{BaTiO}_3$  polycrystalline sample. (b) The (002) / (200) doublet shows a fit as good as that of the single-peak fitting method. This would not be the case when loading increases.

Preferred orientation (or texture) is one of the common problems affecting material properties and diffraction data analysis. It can be simply defined as greater volume fraction of certain crystal orientations. In this work, the March-Dollase formulation in *GSAS* was used. For rod-shaped crystals, the total intensity diffracted by an atomic plane can be written as the following proportionality:

$$I_{hkl} \sim P_{hkl}(\alpha) F_{hkl}^2 \quad (4.9)$$

where  $P_{hkl}(\alpha)$  is proportional to the density of poles of this plane. For a cylindrically symmetric specimen produced by a volume-conserving compression or extension along the cylindrical axis, the pole figure profile is given by this equation:

$$P_{hkl}(\alpha) = \left[ r^2 \cos^2 \alpha + \frac{1}{r} \sin^2 \alpha \right]^{-3/2} \quad (4.10)$$

where  $\alpha$  is the angle between  $hkl$  plane normal and the preferred orientation vector, and  $r$  is the refinable March coefficient. It characterizes the strength of the preferred orientation and is often related to the amount of sample deformation. The texture results and their interpretation will be presented in Chapter 5.

The following section describes an alternative Rietveld analysis that properly considers elastic strain anisotropy. It will be shown that its results are more appropriate than either single-peak fitting or “traditional” Rietveld analysis.

## 4.5 Calculating Lattice Strains: the Improved Rietveld Method

### 4.5.1 Cubic Symmetry

Consider a polycrystal composed of grains of *cubic* symmetry randomly oriented in different directions. Also assume that the polycrystal has isotropic stiffness.

Stiffness of a single grain, however, is not isotropic (for most materials) and depends on the crystallographic direction under consideration, i.e., it is anisotropic. The diffraction elastic constants (i.e., the slopes of applied stress versus lattice strain curves for different *hkl*s) are, by the same reasoning, anisotropic because a diffraction experiment is looking at a subset of similarly oriented grains.

For a *cubic* material, the lattice spacings are given by (*a* is the lattice constant):

$$d_{hkl} = \frac{a}{\sqrt{h^2 + k^2 + l^2}}. \quad (4.11)$$

From this, one can calculate the *hkl*-specific lattice strain in the cubic polycrystal (or for any other crystal structure, for that matter) using the following equation and a reference value  $d_{hkl}^0$ :

$$\epsilon_{hkl} = \frac{d_{hkl} - d_{hkl}^0}{d_{hkl}^0}. \quad (4.12)$$

Combining Equations (4.11) and (4.12) yields:

$$\epsilon_{hkl} = \frac{a - a^0}{a^0}. \quad (4.13)$$

Notice that Equation (4.13) is *not* a function of *h*, *k*, or *l*, thus the lattice strain calculated using the regular Rietveld method will be independent of *h*, *k*, or *l*, which

is quite unrealistic. Figure 4-5 is a simplistic model of this problem. The three different grains depicted in the picture have different stiffness so they will undergo different lattice strains, hence  $\varepsilon_{hkl}$  should be a function of  $h$ ,  $k$ , and  $l$ . Equation (4.12) needs to be modified in a way to include this  $hkl$ -dependent anisotropy. The rest of this chapter introduces the improved Rietveld method to solve this problem. This method is already implemented in *GSAS* [16] for cubic structures [23, 24]. Additional recommendations are provided on how to expand it to other crystal structures.

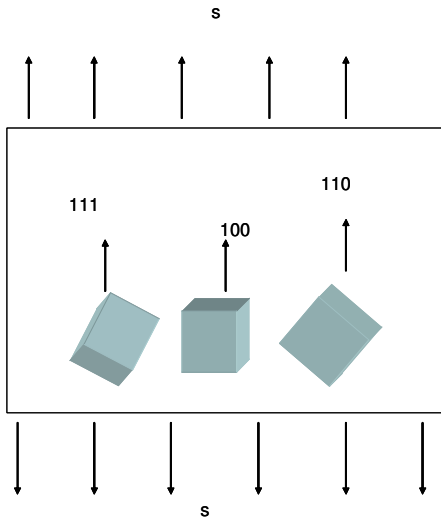


*Figure 4-5: Different grains have different plane-specific elastic moduli, hence will exhibit different lattice strains.*

In a cubic material, the crystallographic-direction-dependent Young modulus is given by:

$$\frac{1}{E_{hkl}} = \underbrace{S_{11}}_{\text{Isotropic}} - \underbrace{2(S_{11} - S_{12} - S_{44} / 2)A_{hkl}}_{\text{Anisotropic}} \quad (4.14)$$

where,

$$A_{hkl} = (l_1^2 l_2^2 + l_2^2 l_3^2 + l_3^2 l_1^2) = \frac{h^2 k^2 + h^2 l^2 + k^2 l^2}{(h^2 + k^2 + l^2)^2}, \quad (4.15)$$

$l_i$  are the direction cosines for a given  $hkl$  unit vector, and  $S_{ij}$  are components of the single crystal elastic compliance tensor. Assume that all the grains have the same stress state (the *Reuss* assumption). In that case, from the simple Hooke's law,  $\varepsilon = \sigma/E$ , one can conclude that strains should be proportional to  $1/E$ ; hence, the following equation can be a good replacement for Equation (4.12):

$$\varepsilon_{hkl} = \underbrace{\frac{d_{hkl} - d_{hkl}^0}{d_{hkl}^0}}_{\text{isotropic}} + \underbrace{\gamma A_{hkl}}_{\text{anisotropic}}. \quad (4.16)$$

The parameter  $\gamma$  in Equation (4.16) would be a measure of strain anisotropy. When  $\gamma = 0$  Equations (4.16) and (4.12) will be the same, hence lattice strains will be  $hkl$ -independent again (the isotropic case). The larger  $\gamma$  is, the bigger the discrepancy between values of lattice strains for different  $hkl$ 's. Therefore, the refinement of  $\gamma$  together with the lattice constant allows the inclusion of *elastic* strain anisotropy in Rietveld analysis; this has already been implemented in *GSAS*.

What if the constant stress (Reuss) assumption for different grains is not a valid assumption? Notice that the linear dependence of lattice strain with respect to  $A_{hkl}$  in Equation (4.16) follows from the linear dependence of  $1/E$  on  $A_{hkl}$  in Equation (4.14). One way to relax the constant stress assumption is to consider lattice strain as a function of a series of powers of  $A_{hkl}$  leading to Equation (4.17) below. During refinement, a subset of the coefficients ( $\gamma$ ) can be used in the fit (too many might

cause instability or convergence problems). Unfortunately, while mathematically feasible, this approach lacks firm physical or mechanical justification and is not recommended.

$$\epsilon_{hkl} = \frac{d_{hkl} - d_{hkl}^0}{d_{hkl}^0} - \gamma_1 A_{hkl} - \gamma_2 (A_{hkl})^2 - \gamma_3 (A_{hkl})^3 - \dots - \gamma_{-1} (A_{hkl})^{-1} - \gamma_{-2} (A_{hkl})^{-2} - \dots \quad (4.17)$$

### 4.5.2 Hexagonal Symmetry

In this case, the problem would be a bit more complicated. The lattice spacing as a function of lattice constants  $a$  and  $c$  is given by:

$$d_{hkl}^2 = \frac{1}{\frac{4}{3} \left( \frac{h^2 + hk + k^2}{a^2} \right) + \frac{l^2}{c^2}}. \quad (4.18)$$

For this crystallographic symmetry, the lattice-plane-specific Young's modulus is a complicated function of  $l_3$  where  $l_3$  is the cosine of the angle ( $\phi$ ) between the unit lattice vector and the hexagonal  $c$  axis (see Figure 4-7):

$$\frac{1}{E_{hkl}} = (1 - l_3^2)^2 S_{11} + l_3^4 S_{33} + l_3^2 (1 - l_3^2) (2S_{13} + S_{44}). \quad (4.19)$$

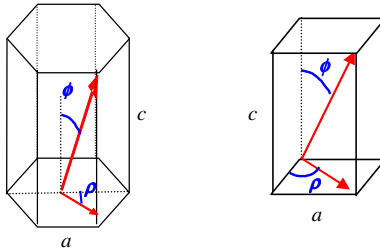


Figure 4-6: Schematic definition of angles  $\phi$  and  $\rho$  in hexagonal (left) and tetragonal (right) unit cells.

In Equation (4.19),  $S_{ij}$  are again components of the single crystal elastic compliance tensor. Daymond et al. [23] employed an approximation to simplify Equation (4.19), noting that since  $1/E_{hkl}$  is a function of  $l_3$  (or  $\cos\phi$ ), the anisotropic strain term should also be a function of  $\cos\phi$ :

$$\varepsilon_{hkl} = \varepsilon_{isotropic} + \gamma \cos\phi \quad (4.20)$$

Here again the extra parameter refined in *GSAS* is the  $\gamma$ . A better representation of elastic strain anisotropy can be achieved by using higher-order terms of  $\cos\phi$  which will lead to more parameters to fit, as shown in Equation (4.21). Separate analyses (not shown) have confirmed that this approach does indeed improve the fit to the  $E_{hkl}$  versus  $\phi$  plot.

$$\varepsilon_{hkl} = \varepsilon_{isotropic} + \gamma_1 \cos\phi + \gamma_2 \cos^2\phi + \gamma_3 \cos^3\phi \quad (4.21)$$

Unfortunately, Equation (4.21) lacks physical or mechanical justification and is nothing but a fitting curve. A more sensible approach might be the use of Equation (4.19) and rearrange it to obtain (again with the Reuss assumption):

$$\varepsilon_{hkl} = \varepsilon_{isotropic} - \gamma_1(1-l_3^2)^2 - \gamma_2 l_3^4 - \gamma_3 l_3^2(1-l_3^2) \quad (4.22)$$

Refining the  $\gamma_i$  parameters in this equation together with the lattice constants can be expected to yield lattice strains that correctly approximate elastic constant anisotropy in hexagonal crystals. This hypothesis was checked for several hexagonal materials and results for Be and Mg are shown in Figure 4-7. The results are also compared with those from the currently used approach designated by Equation (4.20). It is interesting to note that while the current approach works well for Be, it yields a poor

fit for Mg. The new approach represented by Equation (4.22), however, successfully estimates the elastic anisotropy of both materials.

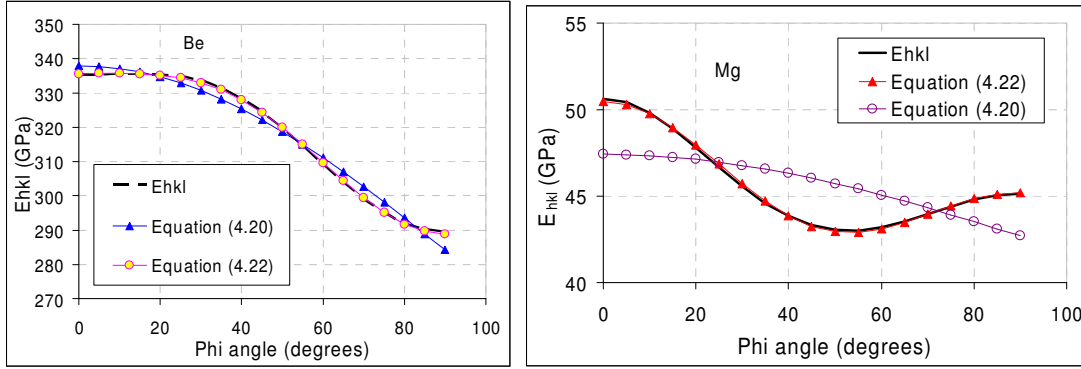


Figure 4-7: Crystallographic-direction-specific Young's modulus ( $E_{hkl}$ ) of beryllium (left) and magnesium (right) compared to approximations by Equations (4.20) and (4.22). The  $\chi_i$  parameters in these equations were refined to obtain the best fit to the  $E_{hkl}$  curve.

### 4.5.3 Tetragonal Symmetry

The case of tetragonal symmetry is yet the hardest of all because the elastic anisotropy is dependent on all direction cosines  $l_i$ . Here, the lattice spacing as a function of lattice constants  $a$  and  $c$  is given by:

$$d_{hkl}^2 = \frac{1}{\left(\frac{h^2 + k^2}{a^2}\right) + \frac{l^2}{c^2}} \quad (4.23)$$

The  $hkl$ -dependent Young's modulus for the  $4/mmm$  crystal symmetry class (e.g., BaTiO<sub>3</sub>) is:

$$\frac{1}{E_{hkl}} = (l_1^4 + l_2^4)S_{11} + l_3^4 S_{33} + l_1^2 l_2^2 (2S_{12} + S_{66}) + l_3^2 (1 - l_3^2) (2S_{13} + S_{44}) \quad (4.24)$$

where  $S_{ij}$  are again components of the single crystal elastic compliance tensor for tetragonal symmetry ( $4/mmm$ ). Therefore, the lattice strains  $\varepsilon_{hkl}$  in the tetragonal case

need to be a function of both  $\phi$ , the angle between the unit  $hkl$  vector and the  $c$  axis, and  $\rho$ , the angle between the component of the unit vector in the base plane and the  $a$  axis (Figure 4-7). Note the following relationships between the directions cosines  $l_i$  and these angles:

$$l_1 = \sin \phi \cdot \sin \rho; \quad l_2 = \sin \phi \cdot \cos \rho; \quad l_3 = \cos \phi \quad (4.25)$$

Figure 4-8 illustrates the dependence of  $E_{hkl}$  on angles  $\phi$  and  $\rho$  for BaTiO<sub>3</sub>. Following the same approach described for the hexagonal case, one can rearrange Equation (4.24) to obtain a good approximation of  $hkl$ -dependent lattice strains in the tetragonal symmetry (specifically, for the  $4mm$ ,  $-42m$ ,  $422$ , and  $4/mmm$  classes appropriate for this equation<sup>1</sup>):

$$\varepsilon_{hkl} = \varepsilon_{isotropic} + \gamma_1 l_3^4 + \gamma_2 l_3^2 (1 - l_3^2) + \gamma_3 l_1^2 l_2^2 + \gamma_4 (l_1^4 + l_2^4) \quad (4.26)$$

One can therefore estimate  $hkl$ -dependent lattice strains by refining the  $\gamma_i$  parameters in this equation. The result for BaTiO<sub>3</sub> is shown in Figure 4-8. Here, refining only the first three parameters ( $\gamma_1$ ,  $\gamma_2$ , and  $\gamma_3$ ) was enough to yield a good approximation of elastic anisotropy. Even a two-parameter refinement (not shown) was reasonably close; hence, the user may have some flexibility regarding the number of parameters to refine.

---

<sup>1</sup> The tetragonal classes  $4$ ,  $-4$ , and  $4/m$  have 7 independent elastic constants leading to this version of Equation (4.24) where the  $S_{16}$  term is non-zero:

$$\frac{1}{E_{hkl}} = (l_1^4 + l_2^4)S_{11} + l_3^4 S_{33} + l_1^2 l_2^2 (2S_{12} + S_{66}) + l_3^2 (1 - l_3^2) (2S_{13} + S_{44}) + 2l_1 l_2 (l_1^2 - l_2^2) S_{16}$$

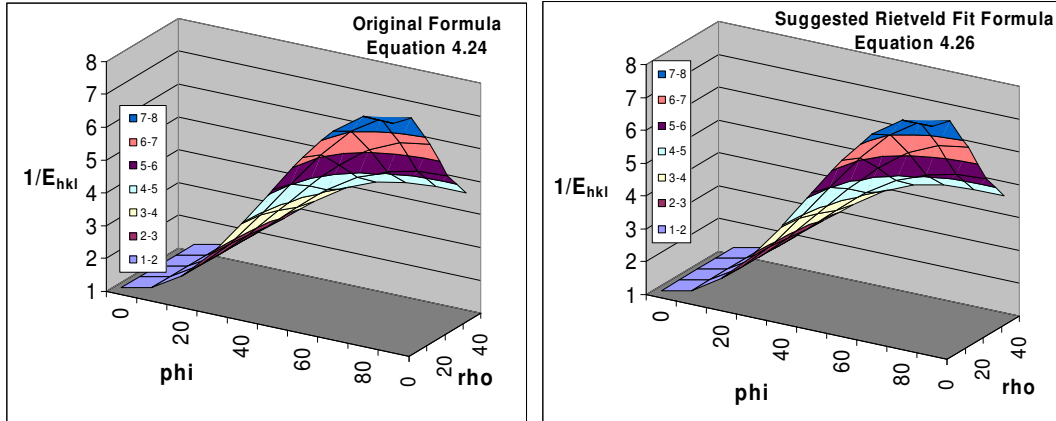


Figure 4-8: Lattice-plane-specific Young's modulus ( $E_{hkl}$ ) of  $\text{BaTiO}_3$  (left) and its fit using Equation (4.26) with three refined  $\gamma$  (right)

It is recommended, therefore, that Equation (4.26) be adapted in *GSAS* to estimate elastic strain anisotropy during the Rietveld refinement of *some* tetragonal materials. One should always keep in mind, however, the two main assumptions in this approach: (i) it only applies to the elastic case; and (ii) it employs the constant stress (Reuss) approximation.

In the next chapter, the experimental results using the methods described in this chapter will be presented. Also in Chapter 5, the results of the model described in Chapter 3 will be presented and compared to experimental results.

## 5. Conclusions and Future Work

### 5.1 Experimental Conclusions: Texture Evolution

The experimental setup and different methods of analysis to extract lattice strain from neutron diffraction experiments were described in Chapter 4. There it was also explained why the regular Rietveld method is insufficient for analyzing data from a mechanically anisotropic material. In this section, only results using the improved Rietveld method and the single-peak fitting are shown.

Figure 5-1a exhibits the (200) / (002) diffraction peaks of BaTiO<sub>3</sub> without the application of external loading. In Figure 5-1b, a uniaxial compressive stress of –100 MPa is applied to the sample. Both figures also show the Rietveld fit. It is obvious from these figures that Rietveld is not the best method for texture analysis.

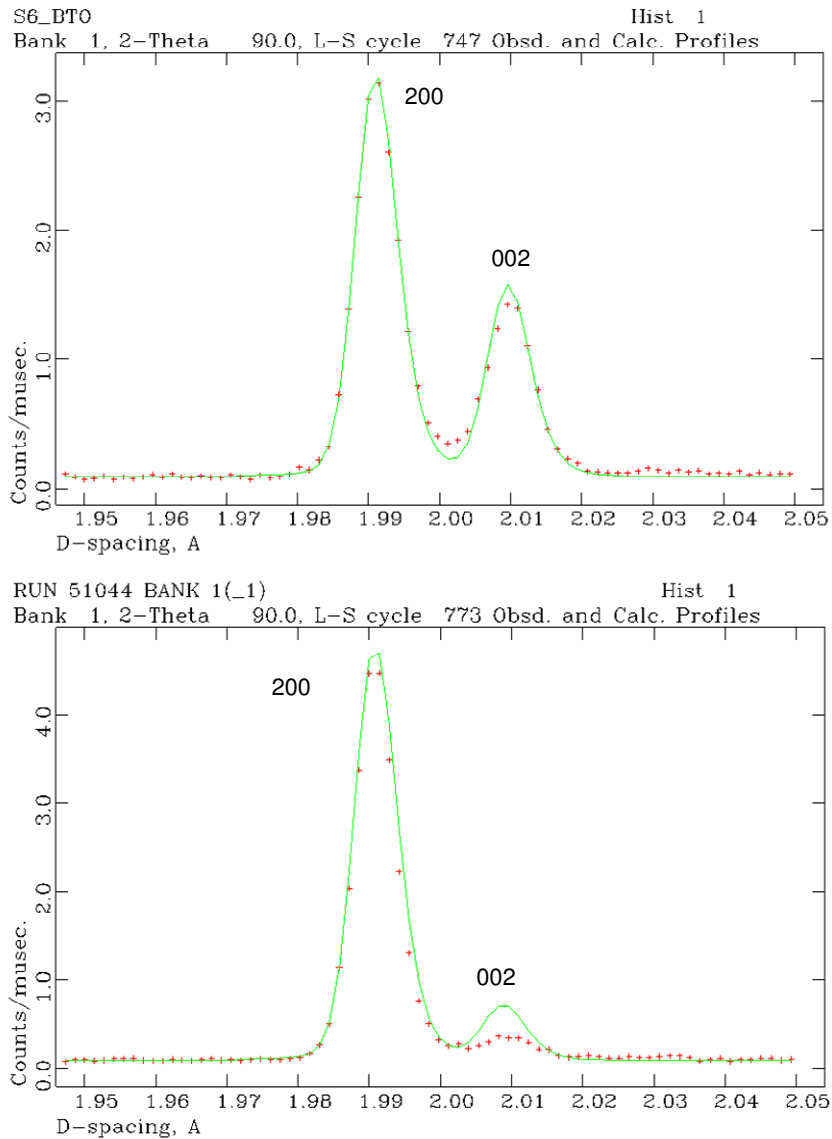
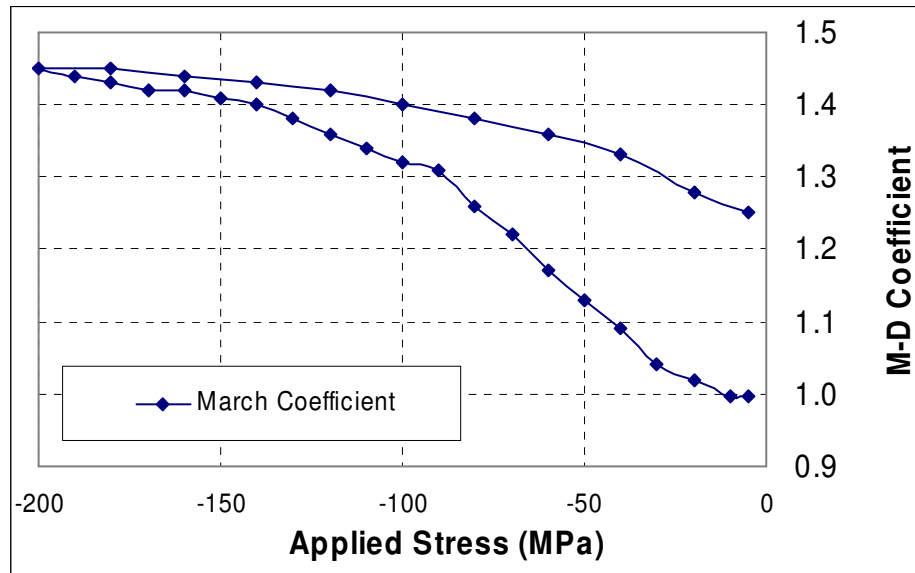


Figure 5-1: (002)/(200) peaks of BaTiO<sub>3</sub>: (a) is the unloaded sample, and (b) is under  $-100$  MPa compressive stress. The dots are raw data while the green lines are the Rietveld fits. The Rietveld method fails to capture the texture evolution as loading has increased.

However, this does not mean that a Rietveld analysis can not provide any information on the texture evolution of the sample. The March-Dollase (M-D) coefficient (Chapter 4) still yields a measure of texture evolution; it just is not as informative and as precise as peak intensity calculations accompanying single-peak fits. Some

examples of the M-D coefficient calculated from experimental results are presented in Figure 5-2. Several properties for BaTiO<sub>3</sub> can be inferred from this figure. First, it is evident that switching starts at coercive stresses even below –5 MPa. Secondly, the switching process is slow and gradual and lasts up to the fracture stress of the ceramic.



*Figure 5-2: At zero loading the March-Dollase (M-D) coefficient value is 1.0, which indicates a random grain distribution. As loading increases, the M-D value increases, indicating domain switching. The change starts at very small loads.*

The same two conclusions can be derived from studying the texture with single-peak fitting analysis (which is a better means of texture quantification). Figure 5-3a shows the (200)/(002) doublet from BaTiO<sub>3</sub> under no load. Using the single-peak fitting method, two type 3 peak profiles (in GSAS) were fitted to the data. In Figure 5-3b the sample is under –100 MPa compressive stress. The fit is still very good. This should be compared to Figure 5-1, showing the superiority of the single-peak method to Rietveld in texture analysis.

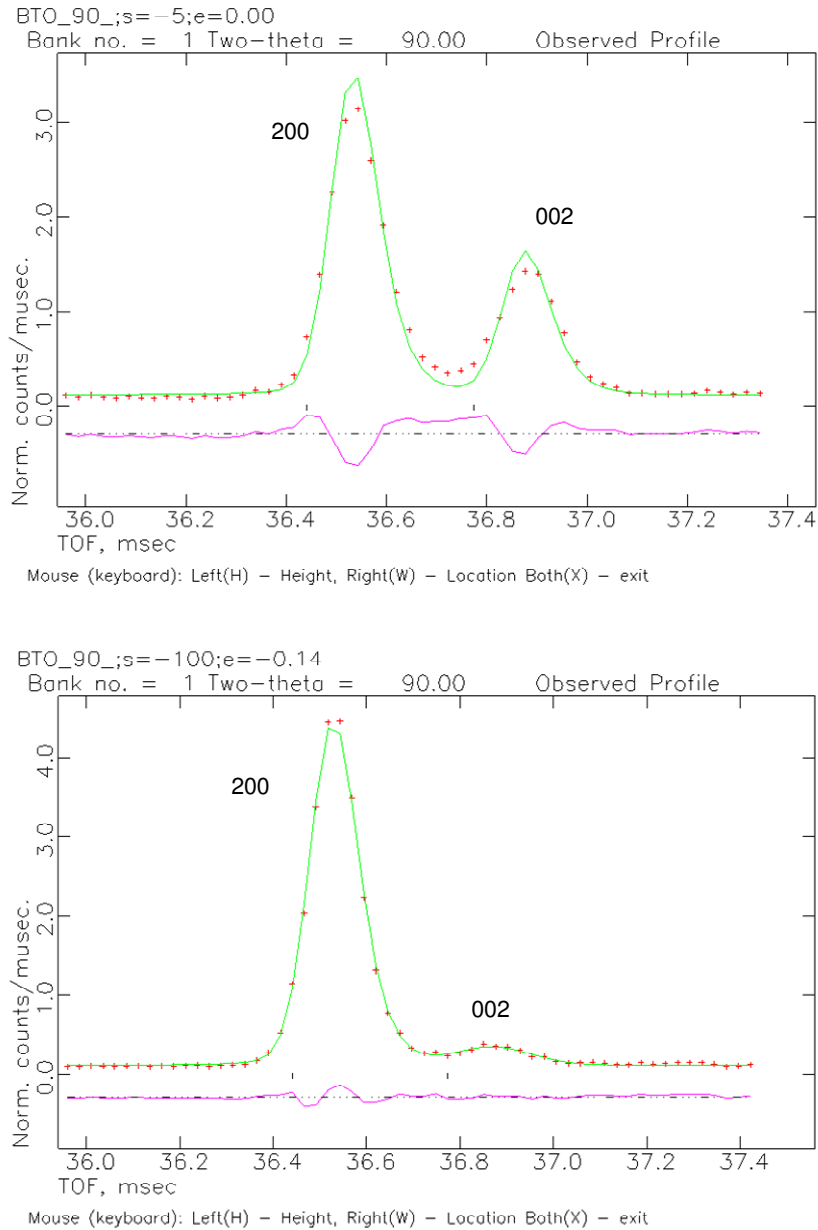


*Figure 5-3: (002)/(200) doublet and single-peak fits to the data using two type 3 peak profiles in GSAS. Both samples are  $\text{BaTiO}_3$ : (a) is a stress-free sample, and (b) is under a compressive stress of  $-100$  MPa. Comparison to Figure 5-1 shows the superiority of the single-peak method in texture analysis.*

Another informative way to demonstrate texture data is using the Peak Intensity Ratio diagrams. Peak doublets such as (200) / (002), (311) / (113), or (220) / (202) can be

chosen for this purpose. In these diagrams, the  $y$ -axis is applied stress (which is the independent variable), while the  $x$ -axis is the ratio of the areas of the integrated peak intensities in the doublet. Let us consider the (200) / (002) peak doublet, for example. The (002) peak corresponds to domains which have their  $c$ -axis, the long axis in the tetragonal unit cell, aligned with (or within the acceptance angle of) the scattering vector, where the scattering vector and the loading direction are parallel in the experimental setup. As the loading increases these (002) domains tend to switch to the perpendicular (200) domains, so the intensity of the (002) peaks will decrease and the intensity of the (200) peaks will increase. As a result, the (002)→(200) Peak Intensity Ratio (PIR) will be an increasing function of applied compressive stress, whereas the reverse (200)→(002) PIR will be a decreasing function of applied stress.

A similar explanation applies to other doublets, too. The only difference is that domains having a  $c$ -axis closer to the loading direction will switch to the perpendicular domains with their  $c$ -axis farther away from the loading axis. Figure 5-4 displays the PIR diagrams with respects to some chosen reflections. The parameter  $\alpha$  in each figure is the angle between the loading axis and the  $c$ -axis of the doublet (see Figure 5.5).

Notice that the same two conclusions obtained using the March-Dollase coefficient in Rietveld can also be reached here: Domain switching starts at stresses below  $-5$  MPa, and it continues as long as the sample is being loaded. But here a third conclusion can be made which was impossible in the Rietveld method. The amount of switching

decreases as  $\alpha$  increases, i.e., there is more switching in the doublets having their  $c$ -axis more closely aligned with the loading axis. This has to do with the fact that the smaller is  $\alpha$ , the larger the resolved stress on the transformation.

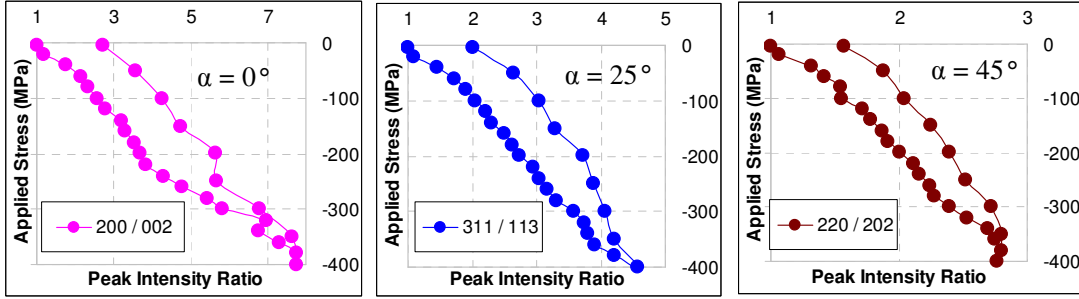


Figure 5-4: Peak Intensity Ratio diagrams for peak doublets (left to right) (200) / (002), (311) / (113), and (220) / (202). The independent axis is the y-axis which is the applied compressive stress in MPa.

To quantify the effect of  $\alpha$  on the extent of domain switching, consider the following.

For uniaxial compression along axis 1,  $\sigma_{11} = \sigma$  and all other stress components are zero. Employing Equation (3.13), the resolved shear stress can be calculated as:

$$\tau^\alpha = \mu_{11}\sigma, \quad \text{where,} \quad \mu_{ij} = \frac{1}{2}(n_i s_j + n_j s_i) \quad \text{and} \quad \mu_{11} = n_1 s_1 \quad (5.1)$$

Using the geometry depicted in Figure xxx, the unit vectors  $\mathbf{n}$  and  $\mathbf{s}$  are obtained as:

$$\begin{aligned} \vec{n} &= (\cos(\alpha + 45), \sin(\alpha + 45), 0) \quad \text{and} \quad \vec{s} = (-\sin(\alpha + 45), \cos(\alpha + 45), 0) \\ \mu_{11} &= \frac{-1}{2} \sin(2\alpha + 90); \quad \text{thus} \quad \tau^\alpha = \frac{-1}{2} \cos(2\alpha)\sigma \end{aligned} \quad (5.2)$$

This means the maximum value of the resolved shear stress will be at  $\alpha = 0$  and will decrease as  $\alpha$  increases, matching the observations exactly.

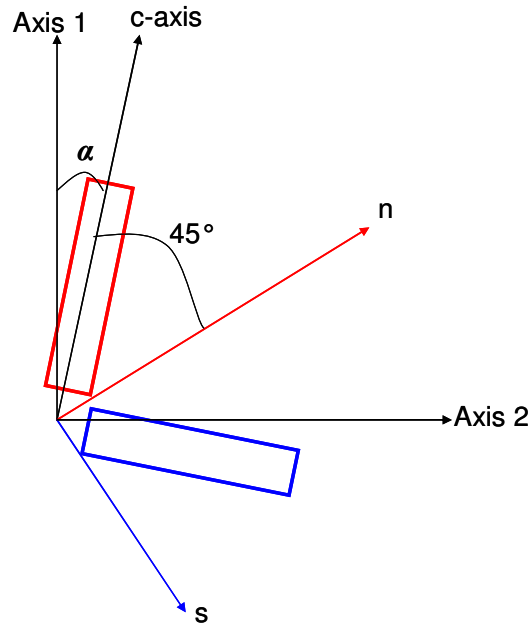


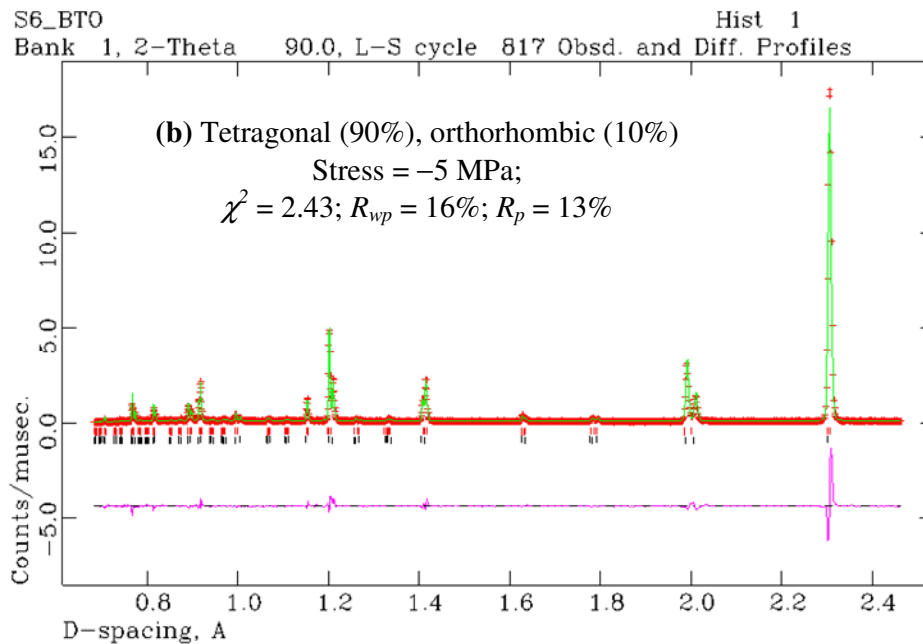
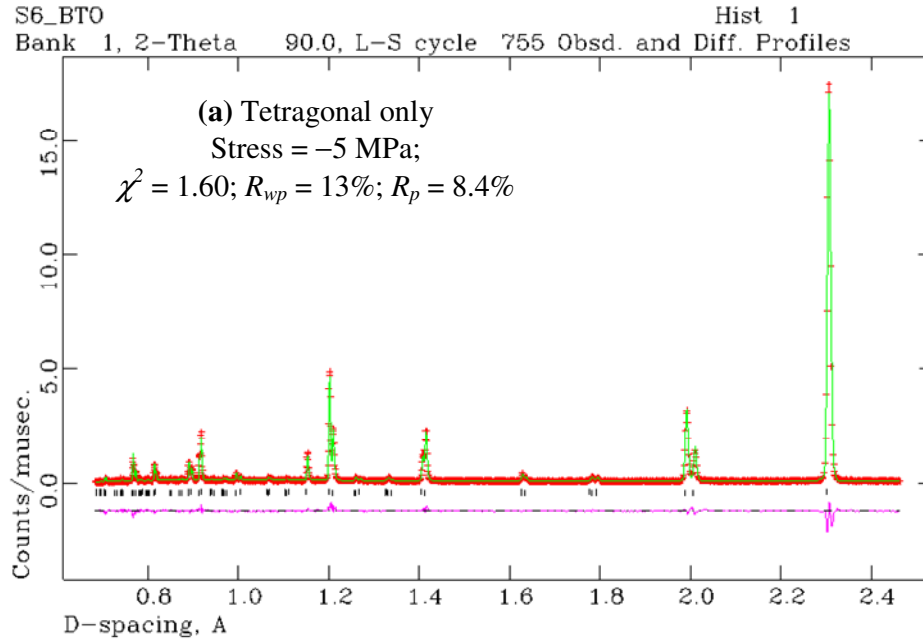
*Figure 5-5: Definition of angle  $\alpha$  between the loading axis (no. 1) and the c-axis of the red domain as it transforms into the blue domain. The unit vectors  $n$  and  $s$  are defined as the inside and outside bisectors, respectively, between the domains' c-axes.*

It is appropriate here to compare the observations presented so far to relevant previous work in literature. Rogan et al. [25] and Li et al. [33] did not observe significant domain switching in single-phase tetragonal PZT. They attributed this in the latter study to lack of sufficient degrees of freedom in tetragonal polycrystals (analogous to the need for five independent slip systems in crystal plasticity to satisfy the compatibility condition). It is therefore somewhat surprising that the tetragonal  $\text{BaTiO}_3$  studied here could undergo significant domain switching. One possible explanation can be found in a recent quantum mechanics model of  $\text{BaTiO}_3$  by Zhang et al. [34] In their study of the various phases of  $\text{BaTiO}_3$ , Zhang et al. developed a new model of the polarization in this material where they suggest the displacement of

the Ti ion is actually along the  $\langle 111 \rangle$  directions. They combine this with a ferroelectric (FE)-antiferroelectric (AFE) coupling along different crystal directions, e.g., the tetragonal phase is obtained by combining an FE-AFE coupling along [100] and [010] to yield a net polarization along [001] as is traditionally known. The implication of this model is that it may be possible to induce significant domain switching in tetragonal BaTiO<sub>3</sub> by forcing polarization changes (or domain switching) along different combinations of the FE-AFE structure. This model needs to be confirmed experimentally. However, if it were correct, the diffraction data would be expected to show these structural changes. So far, the neutron diffraction data did not yield any evidence to support the Zhang et al. model. It is possible that the expected changes in the diffraction peak profiles are too subtle to be captured by neutrons. Therefore, one of the future studies will attempt to collect high resolution synchrotron x-ray data to observe structural evolution in BaTiO<sub>3</sub> under loading.

One relevant issue that was investigated with neutrons concerns the proposed transformation of tetragonal BaTiO<sub>3</sub> into orthorhombic under applied stress. Burscu [35] suggested the existence this transformation in single crystal BaTiO<sub>3</sub>, but did not provide direct proof. In the present study, the orthorhombic phase was attempted in the Rietveld analyses of polycrystalline samples. Figure 5.6 illustrates the results of these analyses. It is clear that the addition of the orthorhombic phase significantly worsened the Rietveld fits by increasing the residuals even at high stress, where the likelihood of the orthorhombic phase is supposed to be higher. It can be concluded, therefore, that within the resolution of neutron diffraction ( $\sim 3$  vol.%), there is no

evidence of a stress-induced tetragonal-to-orthorhombic phase transformation in the BaTiO<sub>3</sub> samples investigated in the present study.



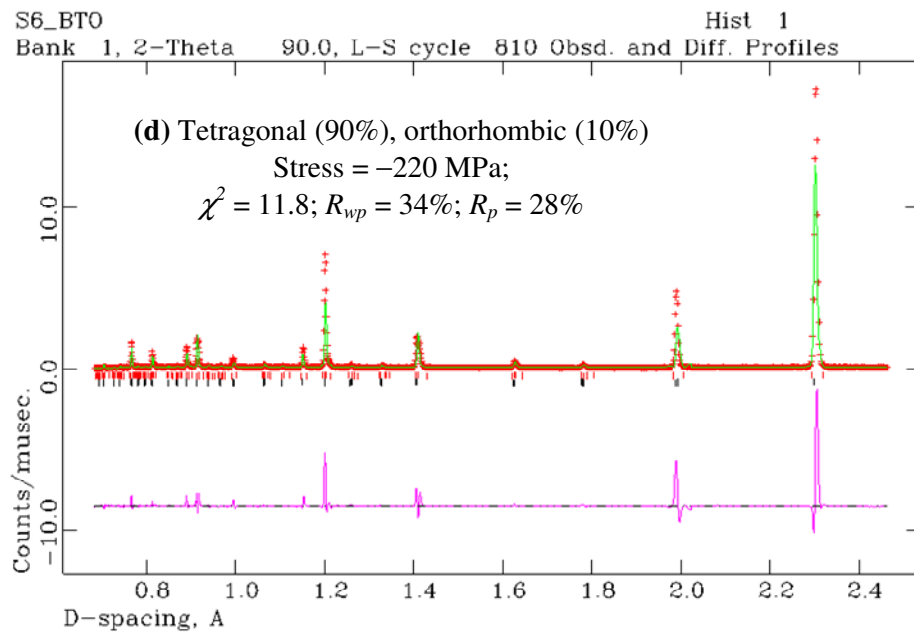
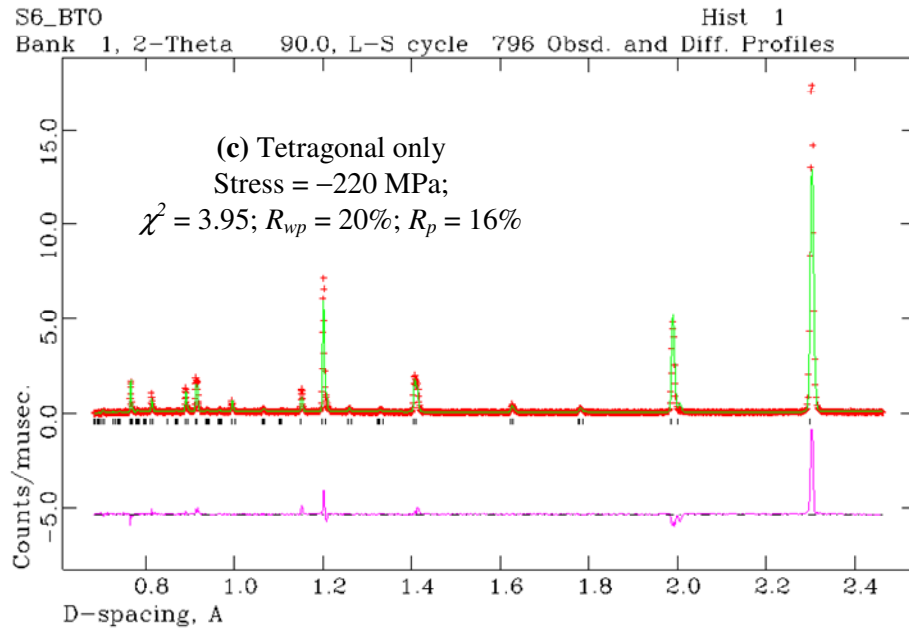


Figure 5-6: Rietveld analyses of polycrystalline  $a$   $\text{BaTiO}_3$  sample with different crystal structures. (a) Tetragonal under -5 MPa stress, (b) tetragonal and orthorhombic under -5 MPa stress, (c) tetragonal under -220 MPa stress, and (d) tetragonal and orthorhombic under -220 MPa stress.

## 5.2 Experimental Conclusions: Lattice Strains

Chapter 4 presented the pros and cons of three different methods of calculating lattice strains from neutron diffraction data. These were single-peak fitting, regular Rietveld method, and improved Rietveld method. Some results from these methods are compared in Figure 5-7. It is clear that the prediction of the regular Rietveld method appears quite unrealistic since it follows the elastic curve closely. Based on evidence presented earlier, domain switching starts at low stresses in this material; hence the elastic portion should be very short. The single peak data is reasonable until a stress value of about  $-100$  MPa. Afterwards, it starts exhibiting large scatter. The reason is explained in Figure 5-8.

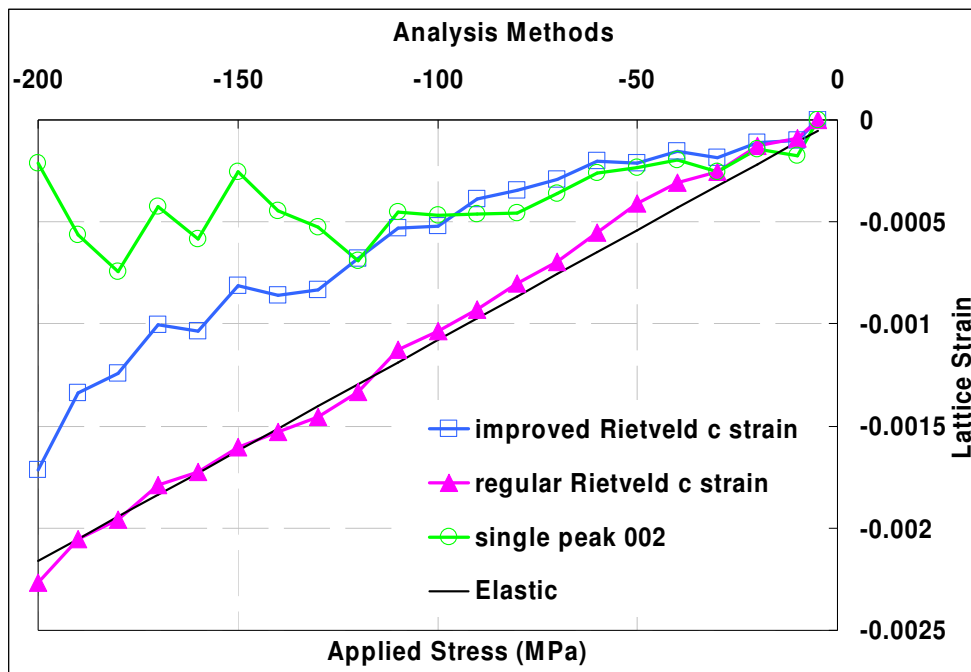
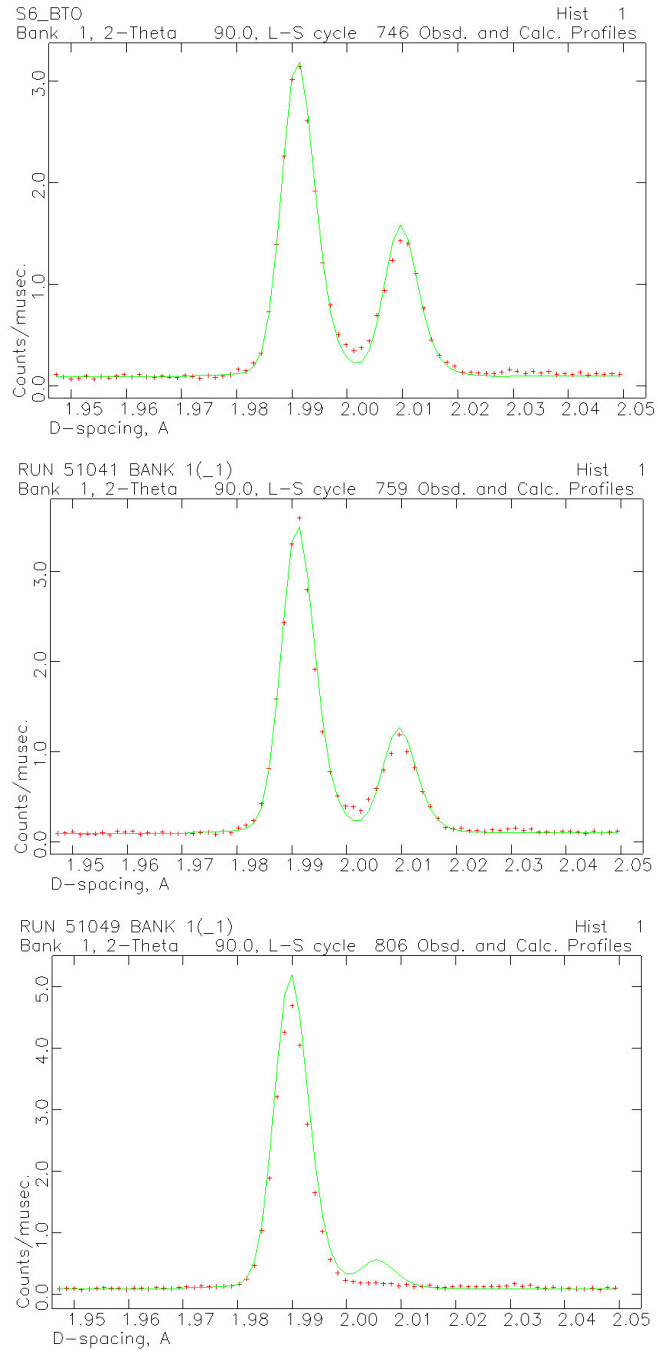


Figure 5-7: (002) Lattice strain using different diffraction data analysis methods (see text for details). The 'elastic' curve is the prediction of the self-consistent model assuming elastic deformation only.

Figure 5-8 shows that the (002) peaks becomes smaller as the value of the applied stress increases. The reason is that the domains having their  $c$ -axis aligned with the loading axis are the ones contributing to the (002) peak, and these domains switch to the perpendicular (200) domains as the loading increases. Figure 5-8-c clearly shows that the (002) is almost indistinguishable from the background, so any attempt to fit a peak to it would result in large fitting errors.

The improved Rietveld method, on the other hand, offers a compromise between the two other fitting techniques. It does include some strain anisotropy to solve that problem in regular Rietveld and deals with drastic peak intensity changes by taking contributions from all reflections to avoid that problem in single-peak fitting.

The improved Rietveld method also provides a more quantitative measure of strain anisotropy, whereas the single-peak method does not, at least directly. How the parameter  $\gamma$  in the improved Rietveld method is a measure of strain anisotropy was discussed in detail in Chapter 4. Figure 5-9 displays the evolution of  $\gamma$  during loading. The anisotropy in the material increases as loading increases. This is due to the effects of domain switching and is analogous to crystal plasticity where lattice strain anisotropy increases as the material starts to yield.



*Figure 5-8: The evolution of (002) / (200) peak doublets under loading analyzed with the single-peak fitting method. As loading increases (0 MPa, 50 MPa, and 150 MPa), the (002) peak vanishes, making a single peak fit impossible or extremely erroneous.*

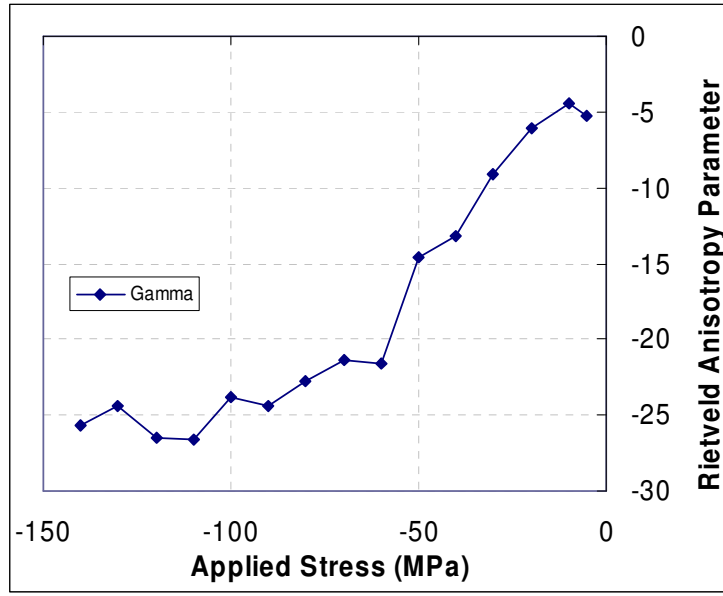


Figure 5-9: Rietveld anisotropy parameter ( $\gamma$  in Equation (4.16)), a measure of the degree of anisotropy. Anisotropy increases as the sample is loaded.

Leaving aside the possibility of scatter at high stresses, a comparison of various lattice strains obtained from single-peak analysis is appropriate (Figure 5-10).

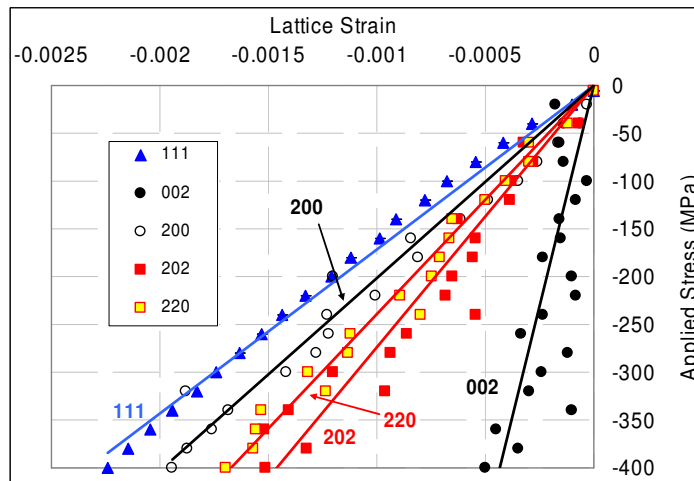


Figure 5-10: Longitudinal lattice strains from neutron diffraction versus applied uniaxial compression of  $\text{BaTiO}_3$ . The strain data were obtained from single-peak fitting. Linear trendlines were fitted to each data set to guide the eye. Note the extreme scatter in the (002) data due to diminished peak intensity at high applied stresses.

Figure 5-11 is the macroscopic strain of the same sample obtained from an extensometer. A comparison of the macroscopic strain values to the lattice strains shows that the effect of strain due to switching (permanent strain) is at least an order of magnitude larger than the lattice strains (elastic strain). For instance, the macroscopic strain at  $-150$  MPa is about  $-0.012$  whereas the largest lattice strain (along  $\langle 111 \rangle$ ) under the same applied stress is around  $-0.001$ . As confirmed by results from the texture development section, it can again be seen here that nonlinearity (a direct result of domain switching) starts at very small stresses.

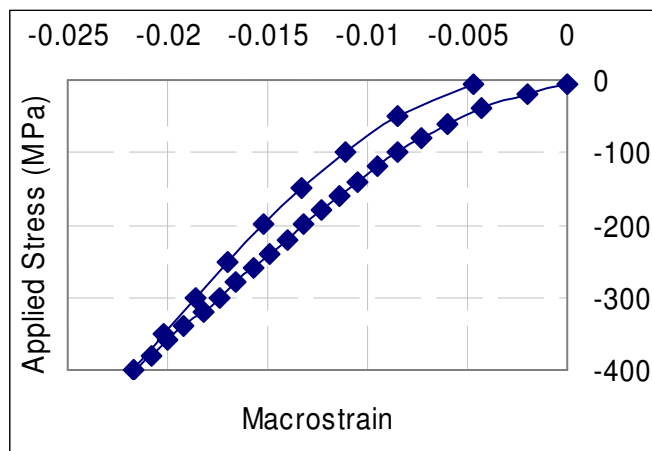


Figure 5-11: Sample  $\text{BaTiO}_3$  macrostrain (elastic plus permanent) along the loading direction measured by an extensometer versus applied compressive stress

The results of Figure 5-10 are appreciated best when compared to those of Figure 5-12 which shows the lattice strains of domains with different  $hkl$  reflections if no domain switching would have occurred, and the system would have behaved elastically in the whole course of loading up to  $-400$  MPa. Consider, for instance, the lattice strains at the final loading ( $-400$  MPa) for different  $hkl$  reflections in both the experimental results (Figure 5-10) and the imaginary elastic material (Figure 5-12).

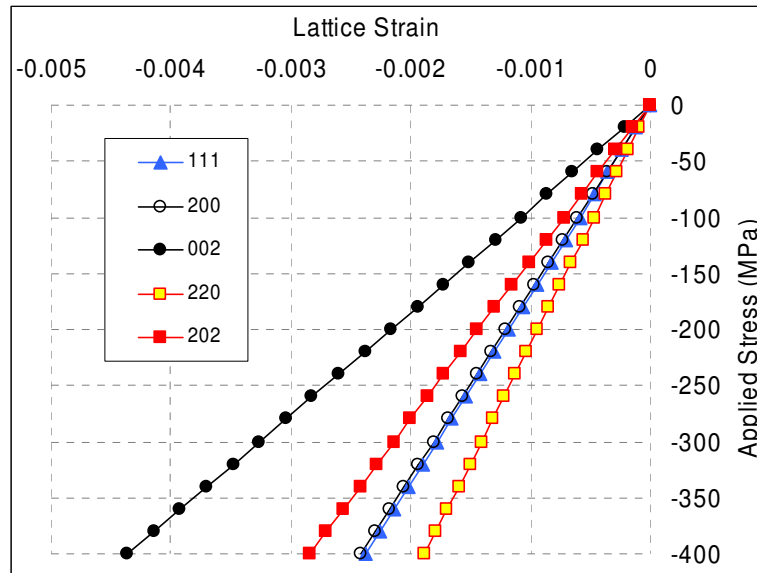


Figure 5-12: Longitudinal lattice strains predicted by an elastic calculation of the SCM versus applied uniaxial compression of BaTiO<sub>3</sub>. The calculations employed the elastic constants listed in Table 5-1 and considered no domain switching. Note the relative slopes of the hkl-dependent lattice strains in comparison to the data on Figure 5-10.

For the (111) reflection the strain values are the same in both figures, almost equal to  $-0.0025$ . All other reflections exhibit smaller strain in Figure 5-10 compared to those in Figure 5-12. Among all these reflections, the domains contributing to reflection (111) are the only domains that do not undergo domain switching. This suggests that all doublets which undergo domain switching exhibit ‘*apparent hardening*.’ It should be noted that apparent hardening has nothing to do with material hardening. This naming convention was chosen simply because the slope of the strain-stress curve has increased. The stress, however, is the total applied stress, which is not necessarily equal to the stress present in specific domains. Actually, the stress in each domain is linearly related to the lattice strain of those domains, so in some sense these figures

show the evolution of domain stress as a function of applied stress. In other words, because of the linear relationship between the grain stress (domain stress) and lattice strain (elastic domain strain), when the lattice strain in a specific  $hkl$  increases, one can conclude that the stress in the grains containing those domains has also increased. The apparent hardening of all reflections which experience domain switching is interesting and may not seem intuitive at first. For that reason, a better interpretation can be reached using the self-consistent model.

### 5.3 Modeling Conclusions

The model details were explained in Chapter 3. The material data employed in calculations is listed in Table 5-1 [35]. The other parameters which need to be input in the model include the critical driving force for each transformation system  $\alpha$  ( $G_c^\alpha$ , Equation (3.17)), change in strain due to switching, or spontaneous strain ( $\gamma^\alpha$ , Equation (3.22)), change in polarization due to switching, or spontaneous polarization ( $P^\alpha$ , Equation (3.22)), and the degree of hardening for each transformation system after switching starts ( $H^{\alpha\beta}$ , Equation (3.16)). The critical driving force was used in the model as a fitting parameter trying to match the starting point of transformations in comparison to the experimental data. The rest of the above-mentioned variables were used to match the lattice strains with those of the experimental results.

One kind of information the model yields is the number of grains (domains) contributing to each reflection. This helps in locating the starting point of switching in each set of twin domains. The results are illustrated in Figure 5-13. The  $x$ -axis is the

	<b>BaTiO<sub>3</sub></b>	<b>Units</b>
$S_{1111}^E$	7.4	$10^{-12} m^2 N^{-1}$
$S_{3333}^E$	13.1	$10^{-12} m^2 N^{-1}$
$S_{1122}^E$	-1.4	$10^{-12} m^2 N^{-1}$
$S_{1133}^E$	-4.4	$10^{-12} m^2 N^{-1}$
$S_{1212}^E$	1.9	$10^{-12} m^2 N^{-1}$
$S_{1313}^E$	4.1	$10^{-12} m^2 N^{-1}$
$d_{311}$	-33.4	$10^{-12} CN^{-1}$
$d_{333}$	90	$10^{-12} CN^{-1}$
$d_{131}$	282	$10^{-12} CN^{-1}$
$\kappa_{11}^\sigma$	4400	$\epsilon_o$
$\kappa_{33}^\sigma$	129	$\epsilon_o$

Table 5-1: Input data for the self-consistent program to model the BaTiO<sub>3</sub> experiment.  $S^E$  are the components of the elastic compliance tensor,  $d$  is the piezoelectric tensor, and  $\kappa^\sigma$  is the permittivity of the material.

applied stress while the y-axis is the number of domains contributing to a specific  $hkl$  reflection. At an early stage (around -10 MPa), the switching in the (200) / (002) doublet starts. As load increases, the number of domains in the (002) curve keeps decreasing and exactly the same number of domains is added to the (200) curve. This is an indication of (002) domains switching to (200) domains due to the applied stress. The (113) / (311) doublet starts switching at a higher stress, but shows the same behavior, i.e., the increase in (311) is exactly equal to the decrease in (113). And the (202) / (220) doublet is the last one to start switching. This again confirms

the experimental results, and the conclusion that the closer the  $c$ -axis of a doublet to the loading axis, the earlier the switching will start.

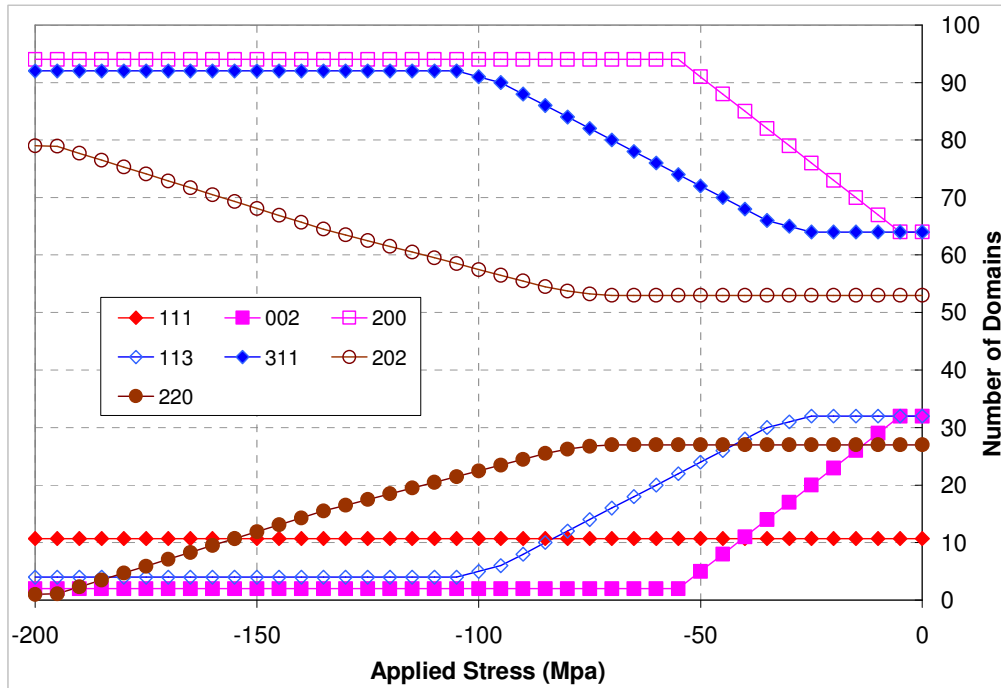


*Figure 5-13: BaTiO<sub>3</sub> domain switching under applied uniaxial compressive stress predicted by the model. The number of domains selected for each reflection (i.e., those that diffract into the longitudinal detector) is plotted versus applied stress. As the load increases domains start to switch beginning with the (002)/(200) pair. It can be seen that the closer the doublet axes are to the loading direction, the earlier the transformation starts. Unlike the original model, however, the new model does not predict reverse switching.*

As far as lattice strains predicted by the model are concerned, Figure 5-14 illustrates strain evolution for reflections (200), (002), (311), and (113). Notice that the material behaves elastically at first. When the transformation in (200)/(002) starts lattice strains in both (200) and (002) show apparent hardening. The case in (311)/(113) is exactly the same. This phenomenon is worth looking at from two angles. First, this

prediction of the model is in agreement with the experimental results (Chapter 4), in the sense that they both show apparent hardening. The experimental showed that only the (111) reflection stays elastic, which is again in agreement with modeling results, while all the rest of the reflections demonstrate apparent hardening (Figure 5-15).

A possible explanation for the apparent hardening phenomenon can be offered as follows. Considering, for instance, the (200) and (002) domains, one should realize that they both reside in the same grain. When domain switching starts those grains can not take additional stress because stress was assumed to be constant throughout the grain. Thus the stress will increase neither in (002) domains nor in (200) domains. Consequently, the elastic strain (lattice strain) will not increase in these domains, because lattice strain is linearly related to stress in the grain. But it should be noted that what is plotted is actually the lattice strain versus the applied stress, not stress in the grain. Since applied stress is the independent variable here it will increase no matter what is happening in the material/model leading to apparent hardening.

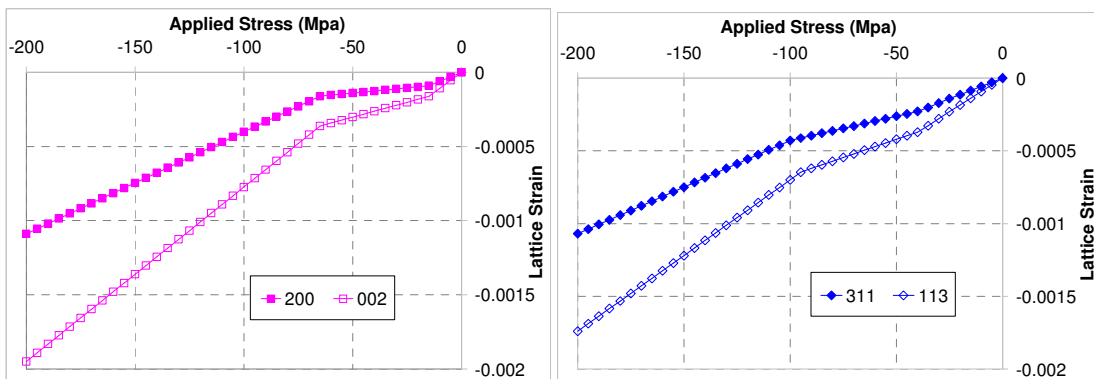


Figure 5-14: Lattice strain evolution under applied stress predicted by the SCM for (a) the (200) / (002) doublet, and (b) the (311) / (113) doublet

Figure 5-15 reveals that the model is reasonable in capturing the nonlinearity arising from domain switching. (200) and (002) both show apparent hardening, i.e., their apparent stiffness (slope of applied stress versus lattice strain) increases. While this is a result of assuming uniform stress within the grain (as explained above), other assumptions could be used to get the same effect. Therefore, the apparent hardening does not necessarily prove that constant stress within a grain is a good assumption. In reality, the stress field inside a grain is nothing similar to uniform. It can also be observed that (111) maintains its linearity since no switching is involved in that direction. Furthermore, it can be seen again that switching, hence nonlinearity, starts at very low applied stress of approximately  $-5$  MPa.

Additional work is needed to improve the match between the model and experimental data. However, one should be aware of an important issue regarding the use of self-consistent models in tetragonal ferroelectrics. There is an ongoing controversy in the field [ref. K. Bhattacharya, personal communication, 2007] on this topic which essentially comes down to the lack of sufficient degrees of freedom in tetragonal crystals to accommodate deformation (as was pointed by Li et al. [33]). Since the SCM does not include direct grain-to-grain interactions (but only via with the equivalent medium), this effect may be lost in the current model. For this reason, modifications in the current SCM will be needed to resolve this issue. Another important question to answer is, since significant domain switching was indeed observed in tetragonal  $\text{BaTiO}_3$ , how is deformation accommodated and whether any internal damage is generated in the process: good problems for future work.

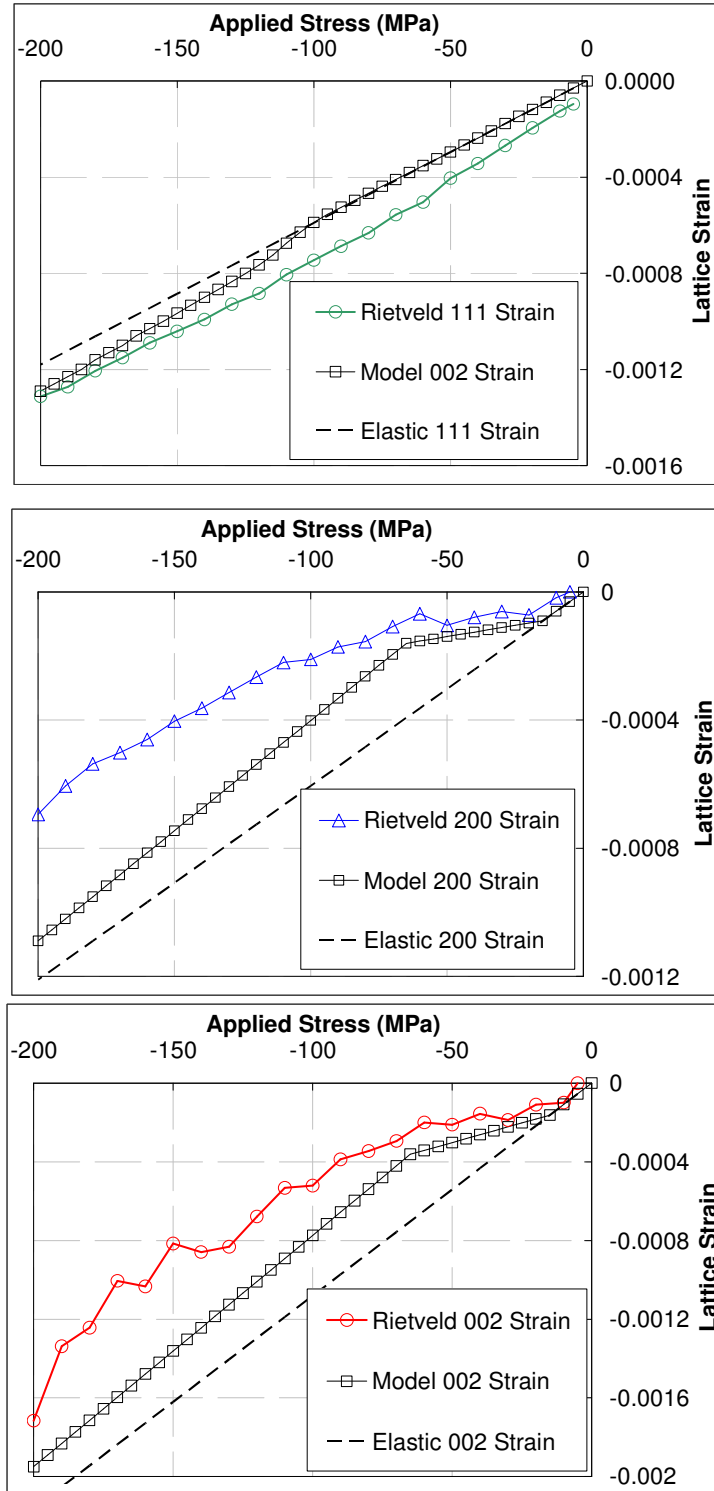


Figure 5-15: (111), (200), and (002) lattice strains obtained from the new model are compared with diffraction data. (111) does not demonstrate nonlinearity, the other two crystal directions exhibit apparent hardening during switching in both experimental and modeling results.

## 5.4 Summary and Conclusions

The most important contribution of this thesis is the adaptation, further development and validation of a self-consistent model for polycrystalline ferroelectrics against neutron diffraction data. Along the way, it was also discovered that the analysis of diffraction data from highly anisotropic materials such as ferroelectrics demands utmost care; thus various analysis methods were investigated to reveal their advantages and disadvantages. The details can be summarized as follows:

- While the single-peak fitting method is the most natural analytical scheme, sometimes it is not a practical choice because the reduction in intensity of some reflections due to domain switching makes it difficult to find the peak position. Likewise, the regular Rietveld method cannot be considered useful because it does not allow for strain anisotropy. The improved Rietveld method proposed here confers two distinct advantages: it can still be applied even when the intensity of one peak becomes too low, and the anisotropy parameter(s) offers a measure of the degree of anisotropy. Hence, this method unquestionably emerges as the preferred system of analysis in cases where single-peak fitting yields scatter in data due to intensity fluctuations.
- Some suggestions for the further refinement of the improved Rietveld method were offered that would allow for its application to a wider assortment of crystal lattice structures, thereby greatly enhancing its strength and applicability. Specifically, a scheme was outlined to improve the accuracy of the hexagonal

formulation, and a strategy was developed for its application to tetragonal systems. Future work should expand upon these schemes, seeking simultaneously to broaden the horizon of materials that can be explored within the model and to further improve the level of accuracy achieved, especially by extending it into the inelastic deformation regime.

- Within the self-consistent model for ferroelectrics developed earlier by Huber et al. [8] a number of advances were made including an innovation that corrects for the reverse switching problem, a method that calculates lattice strain by selecting appropriate grains and averaging their contributions to specific reflections, a capacity to track the number of domains contributing to a selected reflection, an ability to input texture (initial grain orientation distribution), and a mechanism that enables the locking of domain switching.
- The comparison of model predictions and diffraction data from BaTiO<sub>3</sub> yielded the following observations: (i) domain switching starts at very low stresses (< 10 MPa) and proceeds gradually; (ii) domains with *c*-axes closer to the loading axis start switching earlier and experience more switching; (iii) lattice-plane-specific (*hkl*) strains, with the exception of (111), exhibit apparent hardening after switching starts. The level of agreement between the model and the experimental data was satisfactory, particularly considering the relative simplicity of the model.

In conclusion, this body of work yielded a useful set of tools to predict the constitutive behavior of polycrystalline ferroelectrics by integrating, for the first time, a self-consistent model to neutron diffraction stress/strain analysis. While these tools involve crucial assumptions, and should be employed only when appropriate, they can be nevertheless useful in the future studies of ferroelectrics as they opened a new venue of research in this field.

### **5.5 Future Work**

The present study naturally led to many interesting future work which can be briefly outlined as follows:

- *Further development of the self-consistent model* for other crystal structures such as rhombohedral, orthorhombic and even monoclinic. This can also help answer the question about the degree of freedom in domain switching to satisfy the compatibility condition since these structures offer a higher number of domain variants compared to the tetragonal structure.
- *Adaptation of other load sharing schemes* (e.g., the recent model by J. Roedel based on laminate composite theory of domain variants: “Effective intrinsic linear properties of laminar piezoelectric composites and simple ferroelectric domain structures” *Mech. Mater.* 39 (2007) 302-325) to introduce a more robust mechanism for inter-domain and inter-grain interactions.

- *Extension of the improved Rietveld method into the inelastic regime.* This can only be accomplished by a combination of mechanics modeling (e.g., SCM) and appropriate modifications of the profile functions in Rietveld. If successful, this effort will have a major impact in the field of diffraction stress/strain analysis.
- *Collection of high resolution applied stress data.* Since it was difficult to apply small incremental steps in uniaxial compression, and since BaTiO<sub>3</sub> started switching at very low stresses, an alternative loading geometry is necessary. Four-point bending was suggested by the author as a good alternative since it creates small stress/strain gradients across sample height, offers both tension and compression on the same sample and is stable. Preliminary experiments were already conducted and the results are quite promising. This geometry is also very suitable for coupled electromechanical loading. Note also that an increased data density in the elastic regime will allow the calculation of single crystal elastic constants (using the SCM for instance) for ferroelectrics: potentially a major impact in the PZT field where these constants are still unknown.
- *Collection of high resolution synchrotron x-ray data.* This is especially crucial for studying structural evolution in BaTiO<sub>3</sub> under loading and validating the model by Zhang et al. [34].

# Bibliography

1. Kamlah, M., *Ferroelectric and ferroelastic piezoceramics - modeling of electromechanical hysteresis phenomena*. Continuum Mechanics and Thermodynamics, 2001. **13**(4): pp. 219-268.
2. Bhattacharya, K. and G. Ravichandran, *Ferroelectric perovskites for electromechanical actuation*. Acta Materialia, 2003. **51**(19): pp. 5941-5960.
3. Jona, F. and G. Shirane, *Ferroelectric crystals*. 1962: Pergamon Press.
4. Cross, L.E., *Ferroelectric ceramics: tailoring properties for specific applications*. Ferroelectric Ceramics, 1993: pp. 1-86.
5. Jaffe, B., W.R. Cook, and H. Jaffe, *Piezoelectric ceramics*. 1971: Blackwell Synergy.
6. Lines, M.E. and A.M. Glass, *Principles and Applications of Ferroelectrics and Related Phenomena*. 1978: University Press, Oxford.
7. Noheda, B., J.A. Gonzalo, L.E. Cross, R. Guo, S.E. Park, D.E. Cox, and G. Shirane, *Tetragonal-to-monoclinic phase transition in a ferroelectric perovskite: The structure of  $PbZr_{0.52}Ti_{0.48}O_3$* . Physical Review B, 2000. **61**(13): pp. 8687-8695.
8. Huber, J.E., N.A. Fleck, C.M. Landis, and R.M. McMeeking, *A constitutive model for ferroelectric polycrystals*. Journal of the Mechanics and Physics of Solids, 1999. **47**(8): pp. 1663-1697.
9. Munoz-Saldana, J., G.A. Schneider, and L.M. Eng, *Stress induced movement of ferroelastic domain walls in  $BaTiO_3$  single crystals evaluated by scanning force microscopy*. Surface Science, 2001. **480**(1-2): pp. L402-L410.

10. Eshelby, J.D., *The Determination of the Elastic Field of an Ellipsoidal Inclusion, and Related Problems*. Proceedings of the Royal Society of London. Series A, Mathematical and Physical Sciences, 1957. **241**(1226): pp. 376-396.
11. Eshelby, J.D., *Elastic inclusions and inhomogeneities*. Progress in Solid Mechanics, 1961. **2**: pp. 89–140.
12. Hall, D.A., J.D.S. Evans, E.C. Oliver, P.J. Withers, and T. Mori, *In-situ neutron diffraction study of the rhombohedral to orthorhombic phase transformation in lead zirconate titanate ceramics produced by uniaxial compression*. Philosophical Magazine Letters, 2007. **87**(1): pp. 41-52.
13. Hall, D.A., A. Steuwer, B. Cherdhirunkorn, T. Mori, and P.J. Withers, *Analysis of elastic strain and crystallographic texture in poled rhombohedral PZT ceramics*. Acta Materialia, 2006. **54**(11): pp. 3075-3083.
14. Hall, D.A., A. Steuwer, B. Cherdhirunkorn, P.J. Withers, and T. Mori, *Micromechanics of residual stress and texture development due to poling in polycrystalline ferroelectric ceramics*. Journal of the Mechanics and Physics of Solids, 2005. **53**(2): pp. 249-260.
15. Hall, D.A., A. Steuwer, B. Cherdhirunkorn, P.J. Withers, and T. Mori, *Texture of poled tetragonal PZT detected by synchrotron X-ray diffraction and micromechanics analysis*. Materials Science and Engineering A-Structural Materials Properties Microstructure and Processing, 2005. **409**(1-2): pp. 206-210.
16. Larson, A.C. and R.B. Von Dreele, in *General Structure Analysis System. Report LAUR*. 2000, Los Alamos National Laboratory.
17. Clyne, T.W. and P.J. Withers, *An Introduction to Metal Matrix Composites*. 1993: Cambridge University Press.

18. Sachs, G., *Zur Ableitung einer Fließbedingung*. Zeitschrift Ver Deutsche Ingenieur, 1928. **72**: pp. 734–6.
19. Taylor, G.I., *Plastic strain in metals*. Journal of the Institute of Metals, 1938. **62**(S 307).
20. Clausen, B., *Characterisation of Polycrystal Deformation by Numerical Modeling and Neutron Diffraction Measurements*. 1997, Technical University of Denmark.
21. Clausen, B., T. Lorentzen, and T. Leffers, *Self-consistent modelling of the plastic deformation of FCC polycrystals and its implications for diffraction measurements of internal stresses*. Acta Materialia, 1998. **46**(9): pp. 3087-3098.
22. Hutchinson, J.W., *Elastic-Plastic Behaviour of Polycrystalline Metals and Composites*. Proceedings of the Royal Society of London. Series A, Mathematical and Physical Sciences, 1970. **319**(1537): pp. 247-272.
23. Daymond, M.R., M.A.M. Bourke, and R.B. Von Dreele, *Use of Rietveld refinement to fit a hexagonal crystal structure in the presence of elastic and plastic anisotropy*. Journal of Applied Physics, 1999. **85**(2): pp. 739-747.
24. Daymond, M.R., M.A.M. Bourke, R.B. VonDreele, B. Clausen, and T. Lorentzen, *Use of Rietveld refinement for elastic macrostrain determination and for evaluation of plastic strain history from diffraction spectra*. Journal of Applied Physics, 1997. **82**(4): pp. 1554-1562.
25. Rogan, R.C., *Investigation of the Multiscale Constitutive Behavior of Ferroelectric Materials Using Advanced Diffraction Techniques*. 2004, California Institute of Technology: Pasadena, California.
26. Tome, C.N., P.J. Maudlin, R.A. Lebensohn, and G.C. Kaschner, *Mechanical response of zirconium - I. Derivation of a polycrystal constitutive law and finite element analysis*. Acta Materialia, 2001. **49**(15): pp. 3085-3096.

27. Dann, J.A., M.R. Daymond, L. Edwards, J.A. James, and J.R. Santisteban, *A comparison between Engin and Engin-X, a new diffractometer optimized for stress measurement*. Physica B, 2004. **350**(1-3): pp. E511-E514.
28. Johnson, M.W. and M.R. Daymond, *An optimum design for a time-of-flight neutron diffractometer for measuring engineering stresses*. Journal of Applied Crystallography, 2002. **35**: pp. 49-57.
29. Young, R.A., *The Rietveld Method*. 1993: Oxford University Print.
30. Cullity, B.D., *Elements of X-Ray Diffraction*. 1978, Reading, Mass.: Addison-Wesley Publishing Co. 545.
31. Warren, B.E., *X-Ray Diffraction*. 1990: Dover Publications.
32. Rietveld, H.M., *A Profile Refinement Method for Nuclear and Magnetic Structures*. Journal of Applied Crystallography, 1969. **2**: pp. 65-&.
33. Li, J.Y., R.C. Rogan, E. Ustundag, and K. Bhattacharya, *Domain switching in polycrystalline ferroelectric ceramics*. Nature Materials, 2005. **4**(10): pp. 776-781.
34. Zhang, Q.S., T. Cagin, and W.A. Goddard, *The ferroelectric and cubic phases in BaTiO<sub>3</sub> ferroelectrics are also antiferroelectric*. Proceedings of the National Academy of Sciences of the United States of America, 2006. **103**(40): pp. 14695-14700.
35. Burcsu, E., *Investigation of Large Strain Actuation in Barium Titanate*. 2001, California Institute of Technology: Pasadena, California.